AGE AND GENDER EFFECTS ON STRAIN RESPONSE AND BIOMECHANICAL PERFORMANCE OF C57BL/6 MICE

A DISSERTATION IN

Engineering

and

Oral and Craniofacial Sciences

Presented to the Faculty of the University
of Missouri-Kansas City in partial fulfillment of
the requirements for the degree

DOCTOR OF PHILOSOPHY

By

HAMMAD MUMTAZ

B.E., University of Engineering & Technology, Lahore PAKISTAN, 2004

M.S., Royal Institute of Technology, Stockholm SWEDEN, 2007

Kansas City, Missouri

2018

AGE AND GENDER EFFECTS ON STRAIN RESPONSE AND BIOMECHANICAL PERFORMANCE OF C57BL/6 MICE

Hammad Mumtaz, Candidate for the Doctor of Philosophy Degree

University of Missouri-Kansas City, 2018

ABSTRACT

Osteoporosis is a systemic skeletal disease resulting in low bone mass and micro architectural deterioration of bone tissue. It causes a consequent increase in bone fragility and susceptibility to fracture. This age-related bone loss is a major healthcare problem nowadays. Due to this fact, ability to maintain the quality of bone with aging has become an area of interest.

C57Bl/6 mice have been commonly used in various studies to investigate the changes in a bone with aging. In this study, C57Bl/6 mice were divided into three age groups: 6 months old, 12 months old and 22 months old. Each age group consisted of 6-7 males and 6-7 female mice. Axial compression tests, three-point bending tests and micro-CT were used to assess age-related changes in femurs, tibiae and ulnae.

The strain response with aging on tibiae and ulnae was captured using digital image correlation (DIC) technique and strain gaging method. The ulna becomes stiffer compared to the tibia as the mice age and it could be because of a trabecular component which induces flexibility in tibia.

The biomechanical performance of femurs, ulnae and tibiae were determined in C57Bl/6 mice. Femurs, tibiae and ulnae of all the groups of mice were analyzed using micro-CT and three-point bending. We calculated the ultimate load to failure (UL), elastic stiffness (ES), modulus of elasticity (E) and the moment of inertia about bending axis (MOI) for each bone.

Linear regression models with robust standard errors were used to determine differences in all the parameters with age in each bone and sex. Micro-CT scans of all the bones were analyzed to determine cortical bone volume per tissue volume (BV/TV), trabecular bone volume per tissue volume (BV/TV) and cortical bone area (B.Ar) and tested for correlation with the biomechanical parameters. The significance level was set to $p < 0.05$.

In conclusion, aging effects on the skeleton need to be evaluated in a site-specific fashion and global conclusions extrapolated from one bone to another may not be valid. Significant differences between sexes occur across aging in bone.

APPROVAL PAGE

The faculty listed below, appointed by the Dean of the School of Graduate Studies have examined a thesis titled 'Age and gender effects on strain response and biomechanical performance of C57Bl/6 mice' presented by Hammad Mumtaz, candidate for the Doctor of Philosophy degree, and certify that in their opinion it is worthy of acceptance.

Supervisory Committee

Ganesh Thiagarajan, Ph. D., P.E., Committee Chair
Department of Civil and Mechanical Engineering

Mark L. Johnson, Ph.D.,
Department of Oral Biology and Craniofacial Sciences

Gregory W. King, Ph.D., P.E.,
Department of Civil and Mechanical Engineering

Antonis Stylianou, Ph.D.,
Department of Civil and Mechanical Engineering

Jeffrey P. Gorski, Ph.D.,
Department of Oral Biology and Craniofacial Sciences

TABLE OF CONTENTS

LIST OF ILLUSTRATIONS

Figure Page

LIST OF TABLES

Table Page

ACKNOWLEDGEMENTS

First, I would like to thank God for blessing me with the completion of this dissertation. I wish to express my sincere gratitude to my supervisor, Dr. Ganesh Thiagarajan, for his guidance, support and encouragement. His knowledge and motivation inspired me in many ways and helped me through the hurdles I encountered during my tenure in the PhD program.

I am also grateful to Dr. Mark L. Johnson, Dr. Jeffrey P. Gorski, Dr. Gregory W. King, and Dr. Antonis Stylianou, for serving on my supervisory committee and for their valuable inputs on my research.

I am so thankful to Dr. Mark T. Begonia for his support as a lab mate. Dr. JoAnna Scott for doing all the statistical analysis for us. Mark Dallas for helping us in conducting all the experiments and micro-CT scanning. And Dr. Lara Nuria for sacrificing the animals and harvesting the bones.

I want to say thanks to my father for encouraging me to see dreams and follow them. I cannot thank enough to my mother for being there in all my difficult times. Many thanks are due to my wife and daughter who stood by me, understood my situation and never gave up. It is due to the collective support of my family that I may be able to complete my dissertation.

CHAPTER 1
INTRODUCTION

Bone becomes more fragile and prone to fracture as we age [1, 2, 3]. Life expectancy has increased remarkably over the years and resulted from declines in infectious diseases [4]. Osteoporosis is a systemic skeletal disease resulting in low bone mass and micro architectural deterioration of bone tissue. It causes a consequent increase in bone fragility and susceptibility to fracture. Breaking a bone is a serious complication of osteoporosis, especially with older patients. Approximately, 8.9 million fractures have been estimated each year in the world [5]. Osteoporosis produces a fracture every 3 seconds. One out of three women and one out of five men over the age of 50 years have experienced an osteoporotic fracture [6, 7]. By 2050, the incidence of hip fracture alone is projected to increase by 240% in women and by 310% in men [8]. This age-related bone loss that leads to increased risk of fracture is a major healthcare problem nowadays. Due to this fact, the ability to maintain the quality of bone and to predict, diagnose and treat bone fragility has become an area of major focus in medical research.

The cells in bone can detect and respond to mechanical loading. *In vivo* mechanical loading models are widely used to study the response of bone to load [9]. It has been established that the bone response to loading is related to the local strain stimulus [10] and hence the understanding of the relationship between the applied axial force and the resulting bone strains is critical.

Axial loading generates compression and bending in the mid-shaft region of long bones such as the tibia. Most tibial loading studies have been limited to young-adult (3–6 months) C57Bl/6 mice. Studies in older mice are important to examine the potential for loading-based approaches to modulate age-related bone loss [11]. Although strain gauge measurements have routinely been used to characterize the strains at one or two sites on the tibia diaphysis, a

thorough analysis was not performed to assess possible differences in bending patterns or strain distributions with age [12]. *Moustafa et al 2009* showed that the mouse fibula as well as tibia and ulna is a useful bone to assess the response of the cells to mechanical loading [13]. In another study on the response to mechanical loading, *Willie et al 2013* suggested that the trabecular bone loss in adults might not only be due to the reduced mechanoresponsiveness, but also that alterations in the load-induced strains within the bone may play a key role [14].

To investigate various changes and influences on aging, C57Bl/6 mice have been commonly used in various studies [15, 16]. This mouse model is considered to provide more accurate data relating to aging parameters compared to other mouse models because it represents the true physiological aging compared to any other mouse models.

Dual energy X-ray absorptiometry (DXA) is a technique that measures bone mineral density (BMD) which is considered as a current standard and a rapid method for predicting bone fracture. With reference to several studies based on this technique, it is difficult to get a clear and comprehensive understanding of the causes of fragility fractures and hence there is a need to investigate how the function of the bone changes with age [17].

Earlier studies showed that genetic variations between different inbred mouse strains result in large differences in bone density and mechanical properties. The three-point bending test has commonly been used in the evaluation of bone strength in earlier studies [18]. A study suggested that the changes in structural rigidity and ultimate load is more dependent on the increase in the material properties compared to the increase in cross sectional geometry [19].

Bone loss in mice may result from both the osteoblast insufficiency and enhanced resorption. Female C57Bl/6J mice experience significant cortical and trabecular bone loss from 7 to 28 months of age [16].

A study on C57Bl/6 mice showed that most of the micro-CT parameters i.e. BMD and cross-sectional moment of inertia tend to increase with growth and then level off some time before 6 months of age [20]. *Wang et al 2004* used localized regions of human cadaveric femurs to examine age related changes. These localized regions, i.e. osteons and interstitial bone tissues, are useful sites to assess the mechanical behavior of the bone [21]. The interstitial tissue in elderly bone was stiffer (higher elastic modulus), stronger (higher yield and ultimate strength) but more brittle (lower toughness) compared with the young adults [21]. Additionally, this study provided more information on the mechanical properties of the interstitial bone tissue showing that the interstitial bone becomes stronger but more brittle as people age [21]. Finally, the results indicate that this is a valid approach to acquire material properties from localized regions in human bone [21].

Schriefer et al 2005 determined the most favorable long bone for assessing the mechanical properties of the mouse skeleton using three-point bending. Tibia produced precise results because its shape allows it to be easily positioned on to the support of the bending test device but the changes in cross-sectional geometry makes this bone inappropriate for assessing the mechanical behavior [22]. The radius satisfied the beam criteria fully and had the least amount of measurement errors while the humerus was the least favorable bone [22]. The amount of error associated with femur bone properties compared to the published data was as high as 35% [22]. *Glatt et al 2007* studied the changes in total body bone mineral density (BMD) and trabecular bone volume and showed that age related deterioration in trabecular architecture differed between the sexes and was more pronounced in females [23].

The first aim of the work presented in this dissertation is to investigate age related changes in strain response experienced by the bone with aging using the C57Bl/6 mice ulna and tibia

loading model. The second aim was to determine differences in biomechanical performance in the ulna, femur and tibia and to compare changes among these bones with aging and between males versus females.

The materials and methods used for analyzing the quality of the bone with aging are described in Chapter 2. The first part deals with the methods used to calculate the strains in ulna and tibia by loading these bones in axial compression. The strains were captured using digital image correlation (DIC) technique and strain gaging. The methods to calculate the biomechanical parameters using three-point bending test are described in the second part of the chapter. Femur, tibia and ulna were tested in three-point bending to calculate the primary indicators of the quality of bone. At the end, the stepwise procedures to calculate the micro-CT parameters using CTAn software are described.

The third chapter comprises of all the results obtained from the methods described in chapter two. The load-strain curves for each method at each level of load along with the changes in strain level experienced by the bone with aging is illustrated with the help of bar charts. The males and females are treated separately to identify gender differences.

The micro-CT parameters were calculated using CTAn software and cortical BV/TV, trabecular BV/TV and cortical bone area are reported at the end of the third chapter.

The fourth chapter includes all the discussion about the results presented in the third chapter. The goal of this chapter is to provide explanations for these results and to develop an understanding of how these results could be an indicator of the biological changes occurring within bone. In addition, the correlation analysis is discussed to develop the relationship between the biomechanical performance of the bone and its morphology.

The fifth chapter presents the conclusions of this dissertation work and the future scope of work. In this chapter, the details of how this work can be useful to understand the bone-muscle cross talk is also included. This work also provides a platform for future investigation of other factors that contributes in the biomechanical performance of the bone with aging.

CHAPTER 2
METHODS

This Chapter describes the design of the whole study. C57Bl/6 mice were obtained from the NIH Mouse Aging Colony at Charles Rivers Laboratories. The mice were divided into three age groups: 6 months old, 12 months old and 22 months old groups. There were six males (weight 35.1 ± 2.4 g) and six females (weight 24.3 ±1.5 g) in 6 months old group, six males (weight 37.4 ± 2.1 g) and six females (weight 27.9 ± 1.5 g) in 12 months old group and seven males (weight 34.1 ± 3.8) and seven females (weight 30.3 ± 4.5) in 22 months old group. All animal studies were approved by the UMKC IACUC.

The mice were euthanized by CO_2 inhalation followed by cervical dislocation. Skin was removed from hind limbs and forearms and the soft tissues were removed from the left and right ulnae, right tibiae and femurs and then wrapped in a PBS soaked gauze. The bones were stored in the -20 degree C freezer until needed [24].

All bones were scanned in a Bruker Skyscan 1174 micro-CT system at a nominal resolution of 9.6 microns employing an aluminum filter 0.5 mm thick and an applied x-ray tube voltage of 50 kV. Camera pixel binning was not applied. The scan orbit was 180 / 360 degrees with a rotation step of 0.4 degrees [25].

2.1 Digital Image Correlation (DIC)

The strain distribution within the mouse bone is of great importance in order to study the effects of compression loading on osteocytes and bone function. The strain response in terms of peak-to-peak strains was captured using Digital Image Correlation (DIC) system. The DIC system is composed of a loading system (Bose ElectroForce 3220, Bose Corp., ElectroForce Systems Group, Eden Praire, MN) and two digital single lens reflex (DSLR) cameras. Both

cameras (Canon Rebel T2i EOS 550D) were equipped with MP-E-65 mm macro photo lenses (Canon U.S.A. Inc. Melville, NY) which have a magnification ranging from 1x to 5x using manual focusing. Both cameras were mounted on to vertical adjustable columns bolted to an anti-vibration table. The columns were also equipped with sliding rails to adjust the distance of camera from the sample. LED light sources and external LCD monitors were also used for the optimization of the video quality. Loading caps specially designed for the bones were installed in the Bose loading system [26]. The DIC system at the School of Computing and Engineering is shown in *Figure 2.1.*

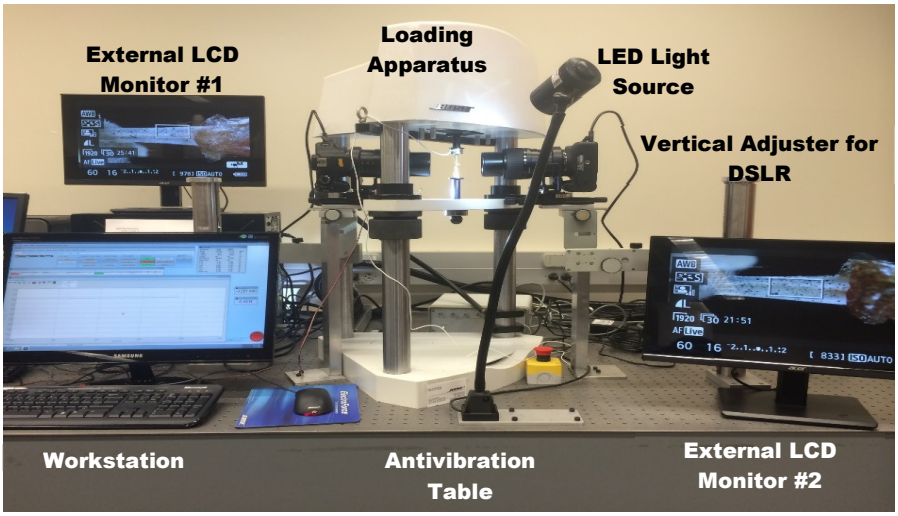

Figure 2-1*: Digital Image Correlation System (DIC)*

2.1.1 Sample preparation

Every sample of ulna and tibia was thawed for at least half an hour before preparing it for the testing. Any residual soft tissue, muscle and the ligaments were removed carefully from each of the sample using tweezers and scissors. Acetone was used to clean the surface of the bone to make the region of interest clearly visible.

2.1.2 Speckling

The samples were then speckled with a black paint using airbrush (Badger 200NH) as shown in *Figure 2.2.* The paint was sprayed from a distance of approximately 6 inches. Three passes were made just to make sure that the speckle pattern is uniform all over the bone on both lateral and medial sides. The samples were then observed under the microscope to see if the speckle pattern is good. The samples were speckled again if lighter dots were observed.

Figure 2-2*: Paintbrush and an ulna showing the speckle patter*

2.1.3 Loading a bone

The bone samples were placed in the loading caps as shown in *Figure 2.3.*

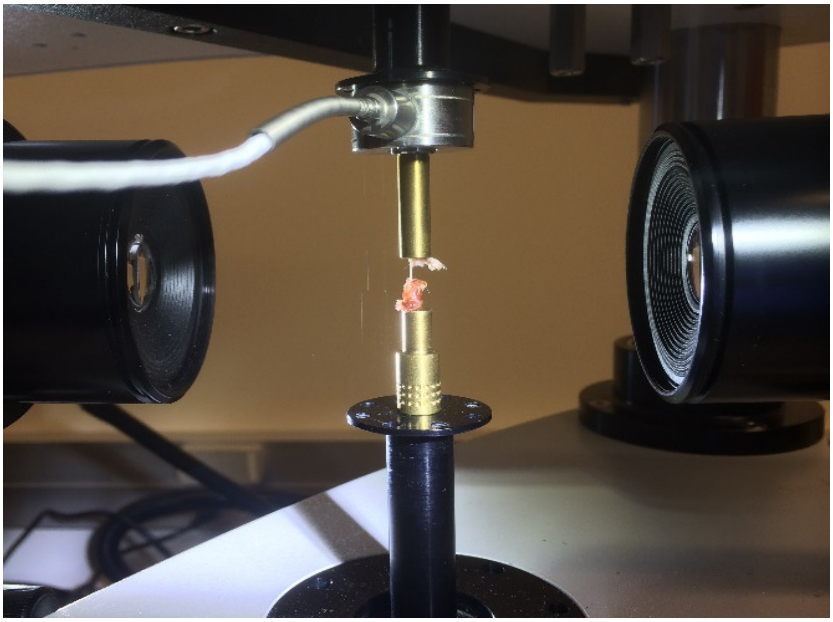

Figure 2-3: *Bone loaded in a Bose machine with two cameras capturing the video*

Both single lens DSLR cameras were adjusted to capture the whole bone within the frame after the bone is loaded and set at the required magnification. The magnification of 1x was used for recording the video of ulnae testing while 2x magnification was used for the testing of tibiae. The video was recorded at the rate of 30 frames per second from both cameras for each type of bone.

After placement of the bone and adjustments of the camera, the bones were preloaded using the WinTest software. A preload of 0.3 N was applied for the testing of ulnae and a preload of 0.5 N was applied for the tibiae.

Figure 2-4*: Screenshot from WinTest software*

Once the bone was stabilized on the fixture supports, the load was applied. There were three levels of load selected for both type of bones. The ulna was loaded at 1N, 3N and 5N load while tibia was loaded at 7N, 11N and 15N load. The videos were recorded at all the three loads for each bone. Ulnae were tested at the frequency of 0.2 Hz (5 cycles) and tibiae were loaded at 2 Hz (40 cycles). Three samples from each group were then tested again at the School of Dentistry to determine the strains using strain gages.

2.1.4 Strain measurements

The videos were broken into frames with the help of a MATLAB code. Then the frames were analyzed using another MATLAB code to estimate the strains at each loading cycle. The region of interest was selected in consistent with the area where the strain gage was applied after DIC testing. The results were then exported to excel file and took the average of the peak and peak strains of the three middle cycles. i.e. 2^{nd}, 3^{rd} and 4^{th} cycle for ulna and 19^{th}, 20^{th} and 21^{st} cycle of the tibia loading. The representative image of the strain map distribution on the speckled bone is shown in *Figure 2.5*.

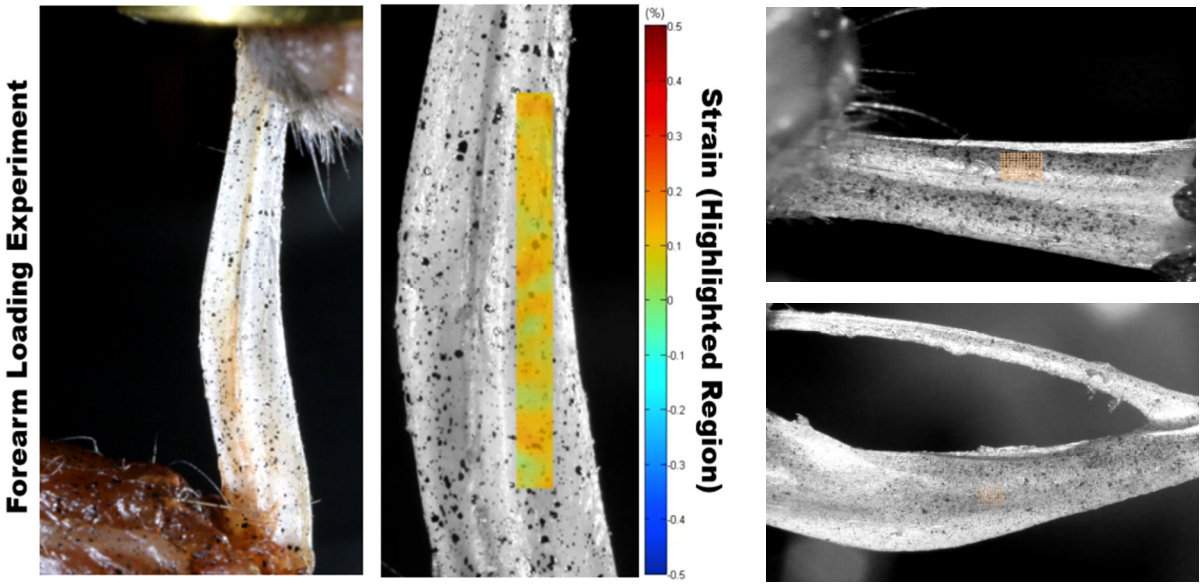

Figure 2-5*: Representative strain maps on ulna (left) and ROI on ulna and tibia (right)*

2.2 Strain Gaging

2.2.1 Wire preparation

A low resistance wire that has an insulation coated on it was cut into two small strips of about 3 inches long. The insulation was removed at the edges of each strip. Some solder flux was applied on the exposed portions of each wire at each end. The wires were twisted over one another and air dried for 10 minutes or till the polyurethane was not sticky.

2.2.2 Strain gage preparation

The extra plastic at all the four edges of the strain gage was removed carefully using a razor blade. Only that central portion that contains the gage and the metal strip at the long ends was left. Then a piece of transparent tape that is specific for strain gage bonding was laid over the shiny surface of the gage. The gage was placed on the flat surface with the shiny side facing upwards and one end of the tape was attached to the flat surface making a 45-degree angle with the surface. The tape was gently rolled over the strain gage and pressed hard. The tape was

peeled with the attached strain gage so that the bottom surface of the strain gage was exposed. A thin layer of catalyst C was brushed to the tape and to the bottom surface of the strain gage. As soon as the surface is dried, a thin layer of the catalyst was brushed over the gage again following with drying.

2.2.3 Sample preparation

The bone surface was cleaned to remove the impurities. With the help of 320 or 400 grit sandpaper the surface was made rough. The surface was cleaned with M-prep conditioner using the supplied cotton gage pads. The surface was cleaned again with a different cotton gage pad and then cleaned with M-Prep Neutralizer applied to the cotton gage pad. With a cotton applicator the bone surface was cleaned with acetone to allow the strain gage to stick properly to the surface of the bone.

2.2.4 Strain gage application

A small piece of solder wire was taken which was supplied with the strain gage kit. One end of this was inserted into the adhesive bottle. Then, after taking out, a small amount of adhesive was applied at the site of gage application. The strain gage was removed from associated tape, and the tape was placed across the site where gage was to be applied. The tape was placed gently down along the length of strain gage application. It was pressed hard for 1-2 minutes with a warm object (fingers preferred). The tape was peeled after 10 minutes. The tape usually comes off and the strain gage remains stuck to the sample. If the application was not successful, the surface was prepared again, and the procedure was repeated.

Another piece of solder wire was taken and dipped in the solder flux. Then an extremely small amount of solder was placed on the tabs of the strain gage. A small amount of solder was

applied to the tabs and the solder flux was applied again. Then the two wires that were prepared earlier were joined to the two ends of the strain gage tabs. The resistance across the two leads with a meter was recorded. If there was no value, solder flux was reapplied, and the two ends were soldered again.

2.2.5 Measurement

The sample was placed in the loading fixture. The prepared wires were soldered with the wires coming from the StrainSmart recording device. An appropriate loading cycle was selected (usually sine wave) and the load was applied, and the strains were recorded.

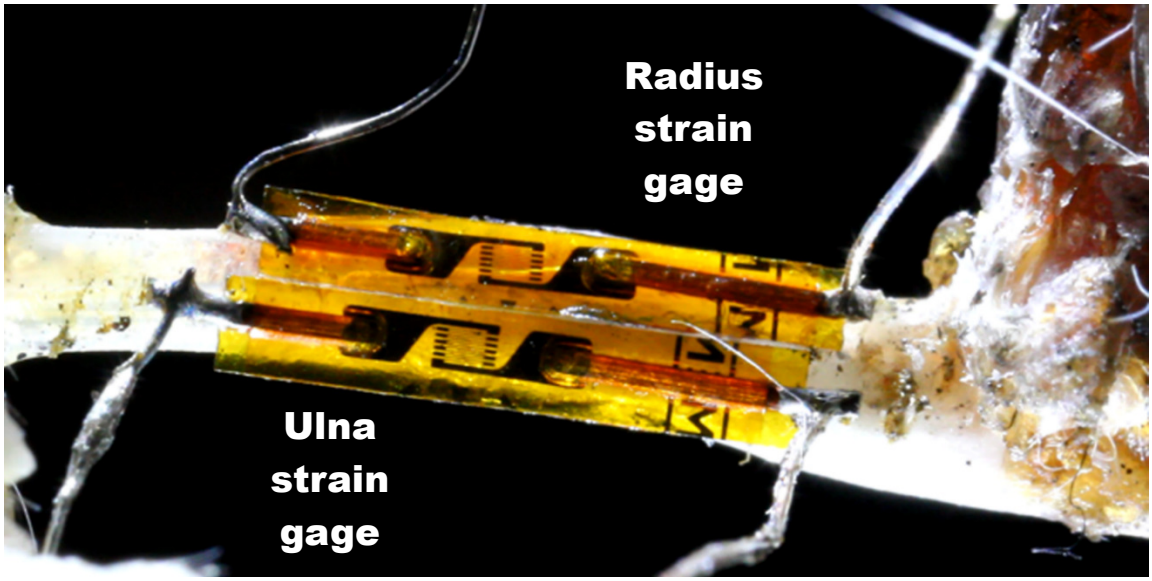

Figure 2-6*: Strain gages attached to the ulna and radius on the medial side of forearm.*

2.3 Biomechanical Parameters

2.3.1 Three-point bending test

A three-point bending was employed on all the samples of all the three type of bones i.e ulna, femur and tibia. The purpose of three-point bending test was to calculate the

biomechanical parameters of different type of bones and see how the biomechanical performance of the bones changes with aging.

The samples were thawed at least half an hour before testing using the ElectroForce 3230 system shown in *Figure 2.7*.

Figure 2-7: *Electroforce 3230 biomechanical tester*

The bones previously used for axial compression tests in digital image correlation (DIC) and strain gaging were used for three-point bending tests. Hence, extra soft tissue was already removed and there was nothing to prepare the sample especially for three-point bending test. However, for tibia testing, a cut was made in the fibula and a piece was removed in order to create a gap for the loading cap to pass through. The length, minimum and maximum diameter and weight was measured before the testing for each sample. The left and right overhangs were

measured after the sample was placed on the BOSE machine fixture. The schematic of the three-point bending is shown in *Figure 2.8*.

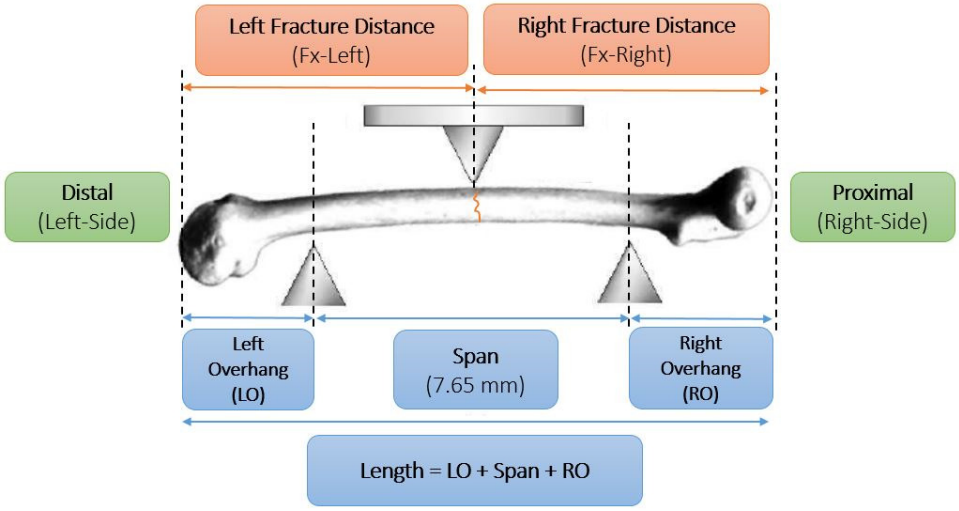

Figure 2-8: *Schemtaic of the three point bending test*

The span length of 7.6 mm was used for the femurs and ulnae while 10 mm was used for the tibiae. Femurs were positioned by keeping the anterior – posterior axis in the loading direction and medial - lateral axis in the bending direction. Ulnae were placed with the lateral - medial axis in the loading direction and the cranial - caudal axis in the bending direction. Tibia were tested while keeping the posterior - anterior axis in the loading direction and the lateral - medial axis in the bending direction. The ulnae and tibia loaded in a tester are shown in *Figure 2.9*.

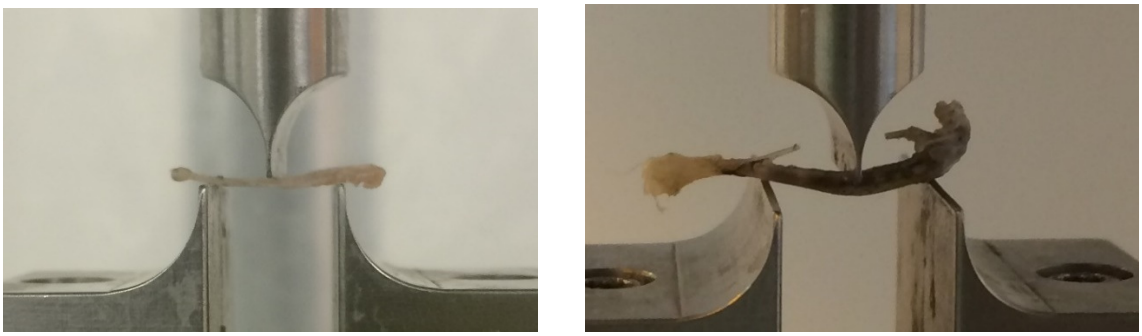

Figure 2-9: *Ulna (Left) and Tibia (Right) loaded in three point bending test*

All the bones were centered on the supports and the force was applied vertically to the midshaft. A constant speed of 0.155 mm/sec was applied to the bone until it fractured.

2.3.2 Estimation of ultimate load & elastic stiffness

A load dispacement curve was obtained from the three point bending test in a text file. The data was imported to the excel file and the load displacement curve was plotted. From the curve, we calculated the ultimate load (UL) which is the highest force that a bone experiences during the three point bending test. The elastic stiffness (ES) of the bone was estimated from the slope of the linear region of the curve.

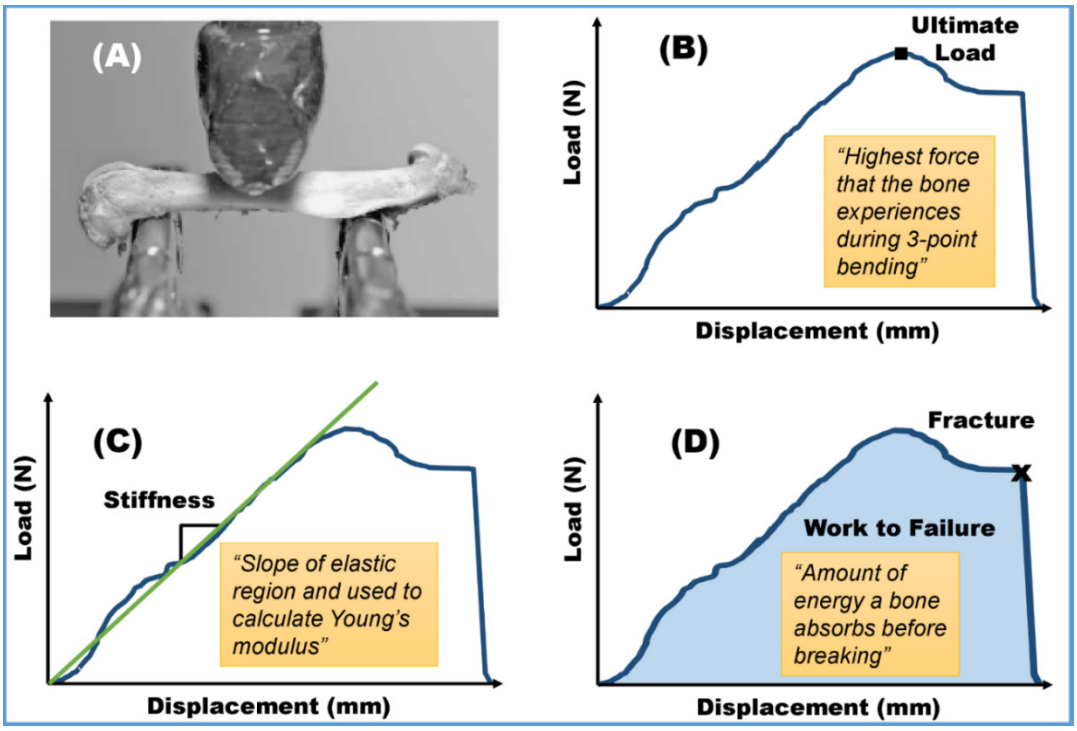

Figure 2-10: *(A) 3-point bending test. (B) the ultimate load is obtained from the load-displacement data. (C) Elastic stiffness is calculated using the slope of the curve (D) Total Work to failure is calculated from the area under the curve*

2.3.3 Estimation of work to failure & displacement

Total work to failure (TWTF), which is the amount of energy a bone abosrbs before breaking, was calculated from the area under the curve. The area under the curve was then divided into two regions, i.e elastic region and plastic region, to determine the work to failure and displacements in those regions. The elastic work to failure (EWTF) was calculated, which is defined as the amount of energy a bone abosrbs before yielding, and the plastic work to failure (PWTF) was also calculated, which is defined as the energy a bone absorbs after yielding and before fracture (see Figure 2-11).

Total displacement was calculated and divided into two parts i.e elastic dispacement (EDISP) which was defined as the amount of bone displacement up to the yield point and post yield displacement (PYD) which is defined as the amount of displacement after yielding but before fracture.

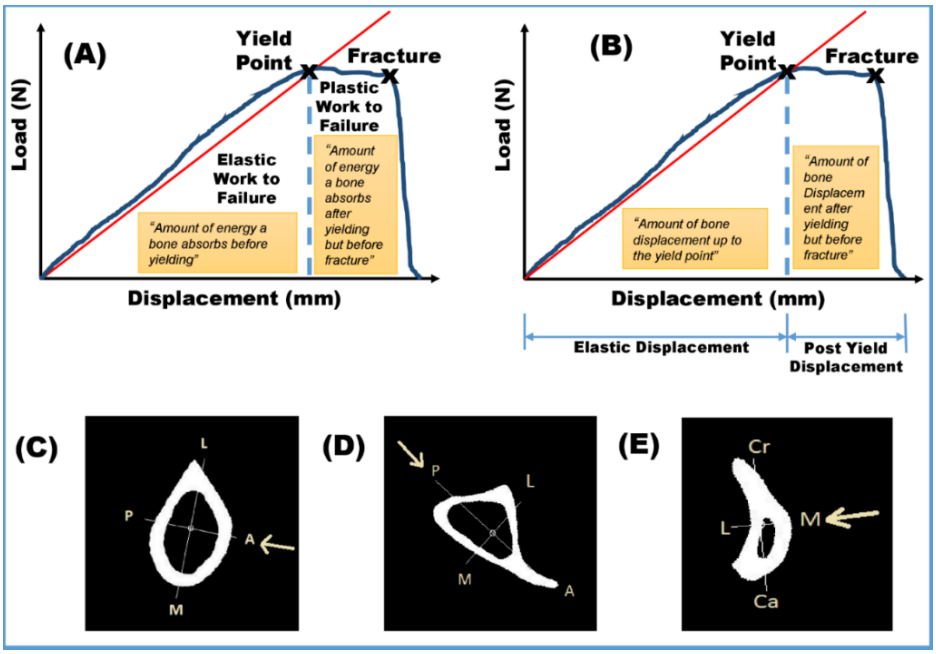

Figure 2-11: *Calculation of (A) elastic and plastic work to failure (B) displacement in elastic and plastic regions and cross section of (C) Femur, (D) Tibia & (E) Ulna showing actual loading orientation for the calculation of bending strength and moment of inertia using BoneJ.*

2.3.4 Calculation of moment of inertia

The moment of inertia (MOI) about the bending axis was calculated using ImageJ according to actual loading orientation. The images of orientation of each type of bone were captured and then compared with the microCT images of the bone in literature to determine the loading and bending axis. The average moment of inertia of all the slices within the span was used to calculate moment of inertia. Every slice was 9.6 micrometers in thickness according to the pixel size and hence we took 791 slices for femurs and ulnae (7.6 mm span) and 1042 slices for tibiae (10 mm span) to calculate the moment of inertia. The left and right overhangs helped in figuring out the starting and the ending slice.

The DICOM stack, which contained all the images within the span length were loaded in ImageJ as shown in the *Figure 2.12*.

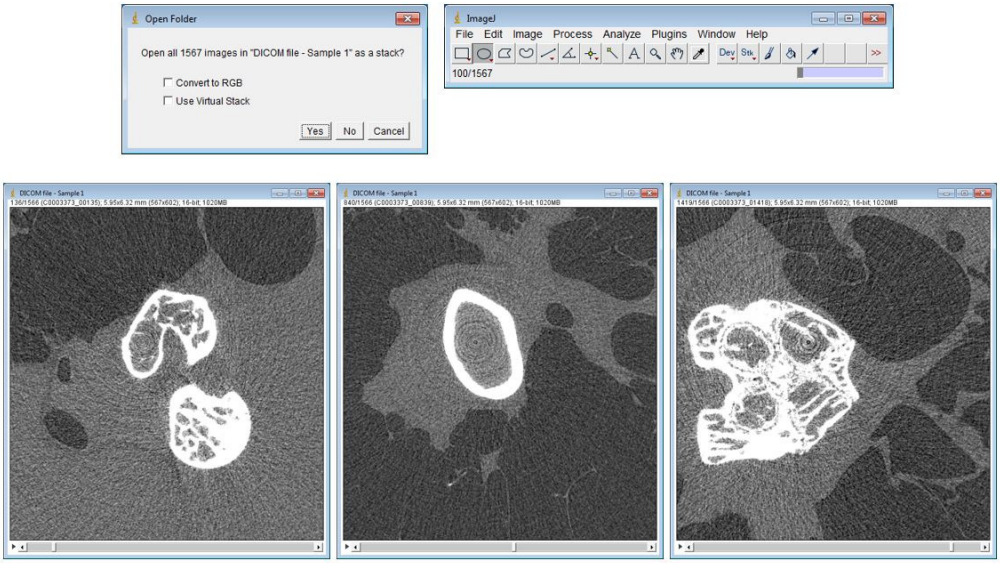

Figure 2-12: *DICOM images loaded in ImageJ*

The "optimize threshold" option was selected, and the options shown in the *Figure 2.13* were checked to apply the threshold.

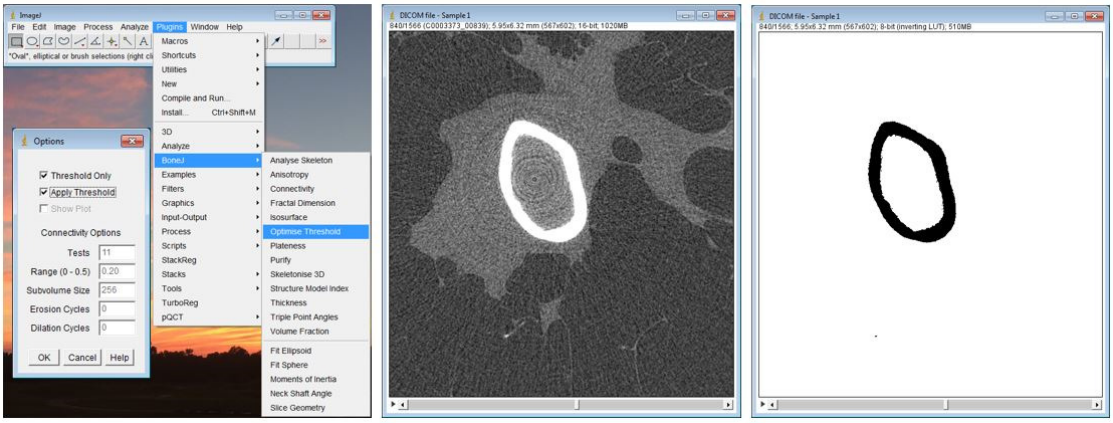

Figure 2-13: *Optimizing Threshold using ImageJ*

The "despeckle" command was used to automatically remove some artifacts and the whole stack was selected to be processed as shown in the *Figure 2.14*.

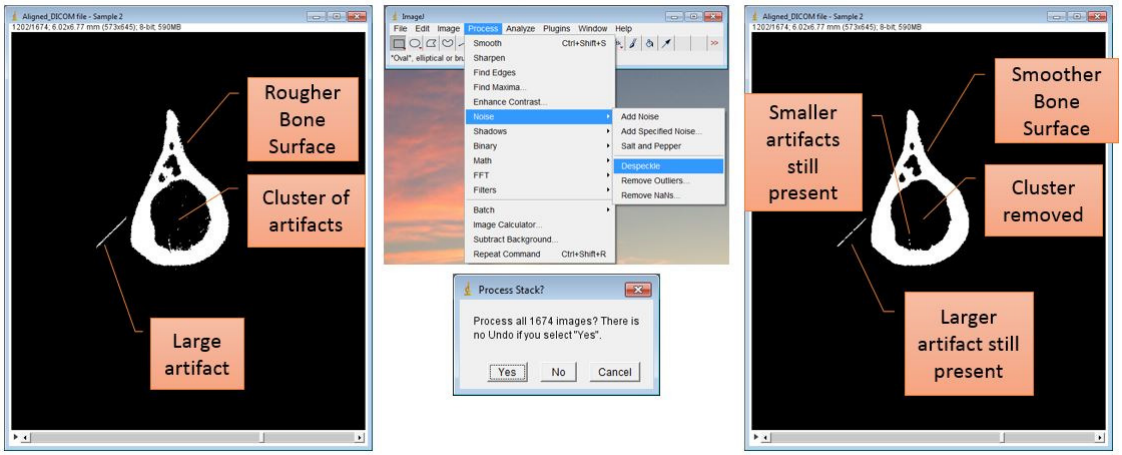

Figure 2-14: *Despeckiling using ImageJ*

The larger artifacts were removed automatically using 'Remove Outliers' command by keeping the values to default as shown in the *Figure 2.15*. The preview option was activated to see how many artifacts could be removed and the artifacts that were still present were removed using the manual removal of artifacts.

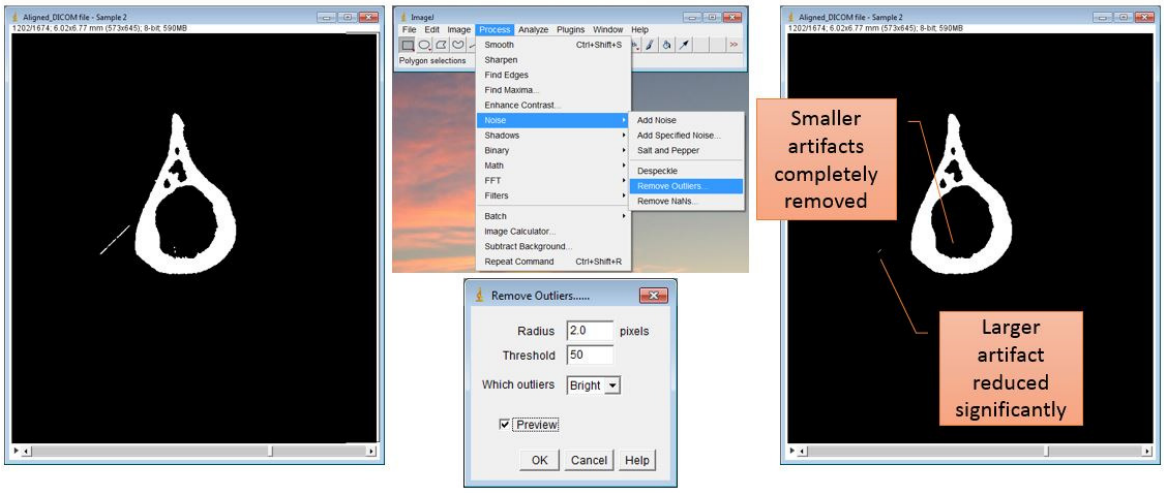

Figure 2-15: *Removing outliers using ImageJ*

The images of each type of bone were then oriented according to the original loading conditions. The bottom right small window as shown in *Figure 2.16* was used to select a loading axis as a principal direction and the bending axis as a secondary direction.

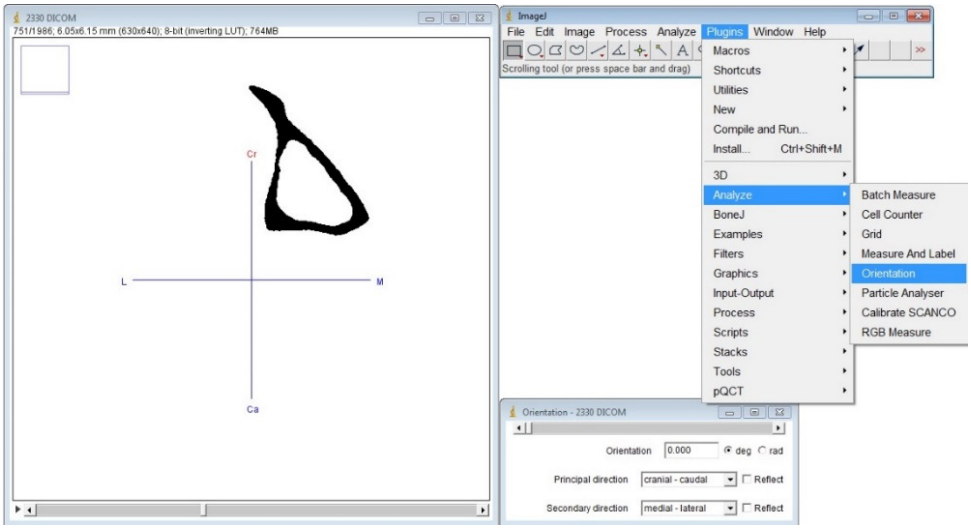

Figure 2-16: *Orientating the bone in ImageJ as per actual loading conditions*

The moment of inertia command was used to align the results and the options were selected as shown in *Figure 2.17*.

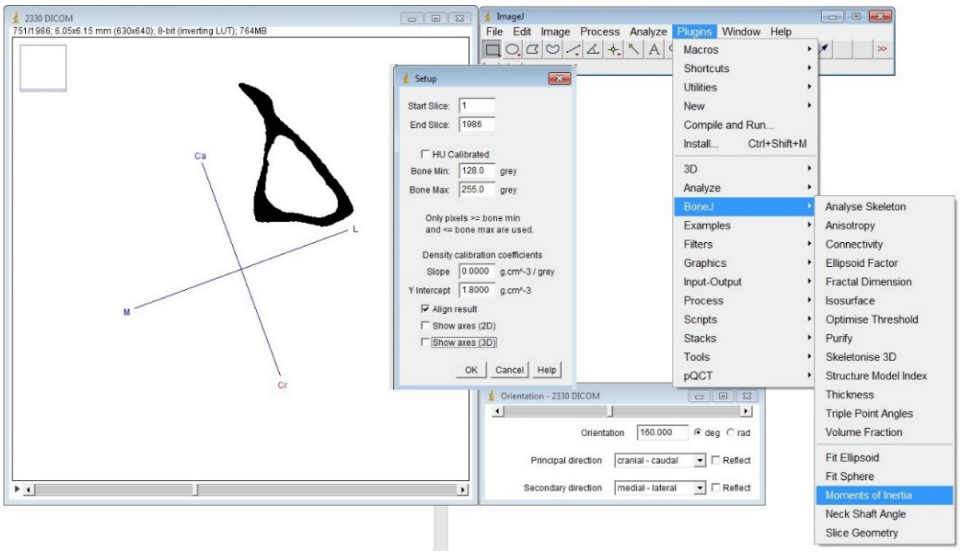

Figure 2-17: *Moment of Inertia calculation using ImageJ*

The results of the aligned stack were saved in a new location and then slice geometry results were obtained using the slice geometry command and the options selected are shown in *Figures 2.18 & 2.19*.

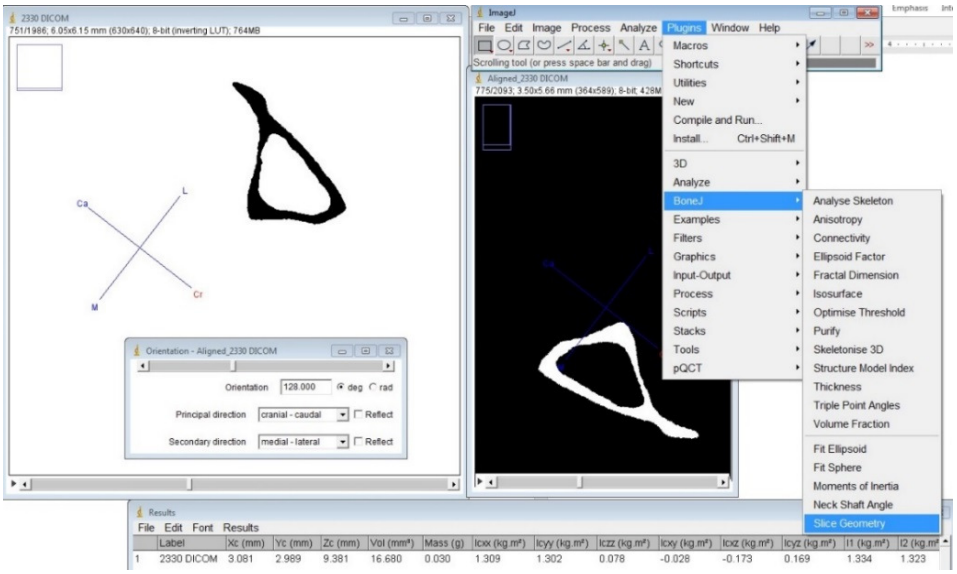

Figure 2-18: *Using slice geometry command in ImageJ*

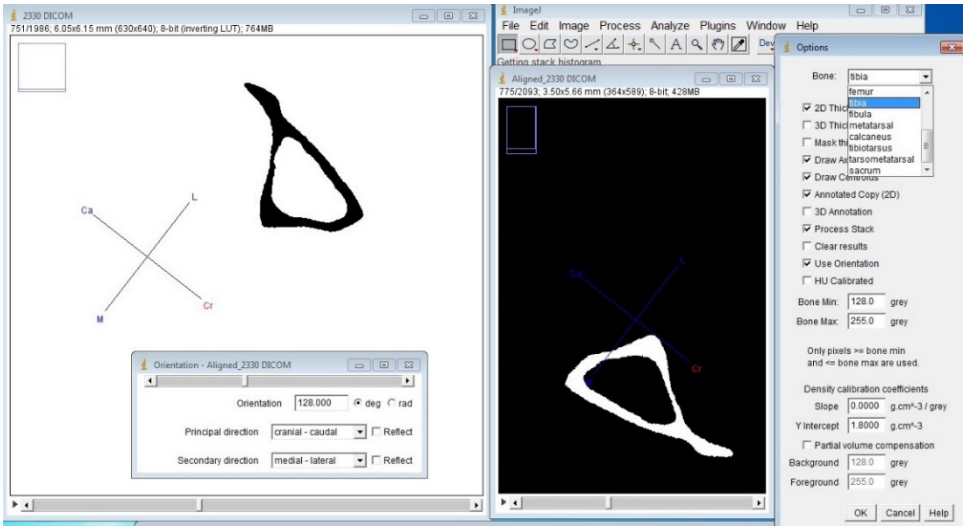

Figure 2-19: *Selection of options for slice geometry results in ImageJ*

The moment of inertia results of all the slices are displayed as shown in *Figure 2.20* and were saved in the excel file to find the average moment of inertia. The annotated stack of the images was also saved for further analysis.

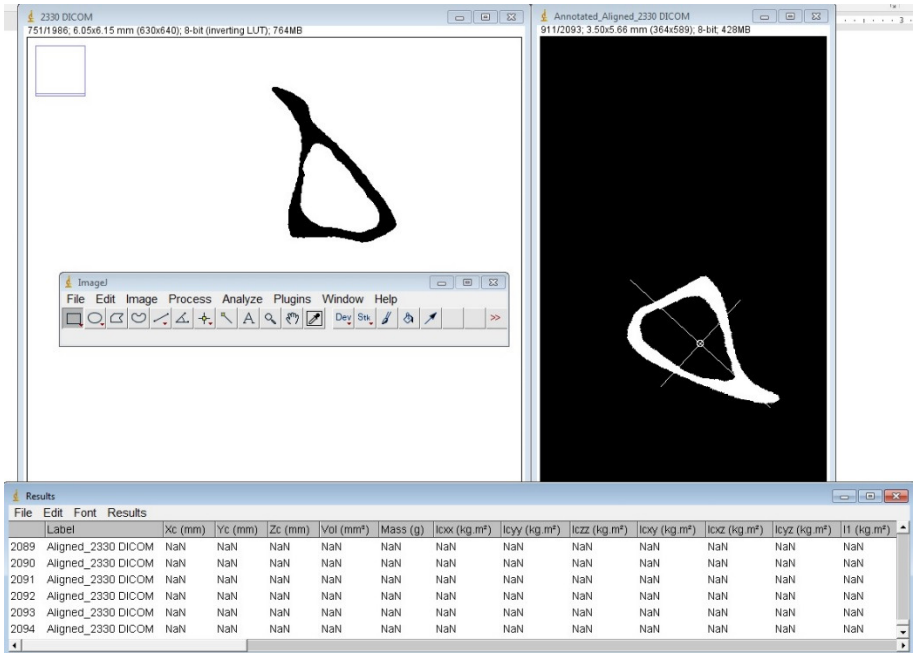

Figure 2-20: *Slice geometry results and annotated realinged images*

2.3.5 Calculation of Young's modulus

Young's modulus (E) was calculated using the following formula

$$E = \frac{Sl^3}{48I} \quad \text{..... Eq 2-1}$$

Where

S = Elastic Stiffness

L = Span length

I = Average moment of inertia

2.3.6 Calculation of compressive & tensile Strength:

The compressive strength (CST) and tensile strength (TST) of the bone were calculated based on the geometry of the mid slice. The distance between the centroid and the periosteal points on the loading axis line were calculated using ImageJ. Strength was calculated using *Equation 2.2*. Distance from the centroid point to the farthest point on the loading axis towards the loading surface gave us a compressive strength while the distance from centroid to the farthest point away from the loading surface resulted in a tensile strength.

$$Max.\ Bending\ Stress = \frac{MC}{I} \quad \text{..... Eq 2-2}$$

Where

M = *Bending Moment* $= \frac{Pmax}{4}$

P_{max} = *Ultimate Load*

L= Length of Span

C = *Distance from the centroid to the farthest point on the loading axis*

I = *moment of inertia about bending axis*

2.4 Micro-CT Analysis

2.4.1 Scan parameters

The mouse bones were scanned in the Bruker Skyscan 1174 at a nominal resolution of 9.6 microns employing an aluminum filter 0.5mm thick and an applied x-ray tube voltage of 50 kV. Camera pixel binning was not applied. The scan orbit was 180 / 360 degrees with a rotation step of 0.4 degrees.

2.4.2 Reconstruction

Reconstruction was carried out with a modified Feldkamp algorithm using the SkyScanTM NRecon software accelerated by GPU3. Gaussian smoothing, ring artefact reduction and beam hardening correction were applied.

2.4.3 Region/Volume of interest selection for trabecular and cortical bone

Region / volume of interest selection, segmentation to binary and morphometric analysis were all performed using Skyscan CT-Analyser ("CTAn") software. For cortical bone analysis a region was selected starting at a position where the third trochanter feature was no longer visible in the cross-sectional slices. The region was selected by moving slice by slice towards the distal metaphysis. The size of the region analyzed was 0.5mm (50 slices). For trabecular bone analysis, a region was selected starting where the condensed epiphyseal trabecular bone first becomes separated. The trabecular region was selected by moving slice by slice proximally away from the growth plate. The size of the region analyzed was 1.0mm (100 slices). Within the trabecular VOI, separation of the trabecular from cortical bone was done using a freehand drawing tool, the boundaries of the selected trabecular VOI running parallel and close to the endocortical boundary.

The cortical VOI was achieved using a freehand drawing tool and a shrink-wrap step that excluded the marrow space from the analysis.

2.4.4 Image segmentation to binary

Global thresholds were selected by visual matching with greyscale images. The same global threshold values were applied to all measured bone samples corresponding to BMD values of 0.38138 to 2.49007 g/cm^3 for cortical bone and 0.27595 to 0.80312 g/cm^3 for trabecular bone calcium hydroxyapatite (CaHA), calibrated by reference phantoms (Bruker-micro-CT, Kontich, Belgium) containing 0.25 and 0.75 g/cm^3 CaHA evenly mixed in epoxy resin rods which were of similar diameter to the scanned bones to minimize beam hardening error.

2.4.5 Morphometric analysis

3D and 2D morphometric parameters were calculated for the trabecular and cortical selected VOIs. The signal to noise ratios of the reconstructed images and segmented binary images did not necessitate any subsequent image processing. Morphometric parameters in 3D were based on the analysis of a Marching Cubes type model with a rendered surface. Calculation of all 2D areas and perimeters was based on the Pratt algorithm of sub-pixel perimeter interpolation.

Morphometric parameters measured by CT-analyzer have been validated on both virtual objects and aluminum foil and wire phantoms. Structure thickness in 3D was calculated using the local thickness or “sphere-fitting” method.

2.4.6 3D model construction

Volume rendered 3D images were generated using an RGBA transfer function in SkyScan CT-Voxel (“CTVox”) software.

2.4.7 Cortical bone analysis

The stack of the reconstructed images was opened in CTAn software and the range of the slices was selected as shown in *Figure 2.21*. We selected 50 slices from the mid diaphysis for each type of bone to calculate the cortical bone parameters as described in *Section 2.4.3*.

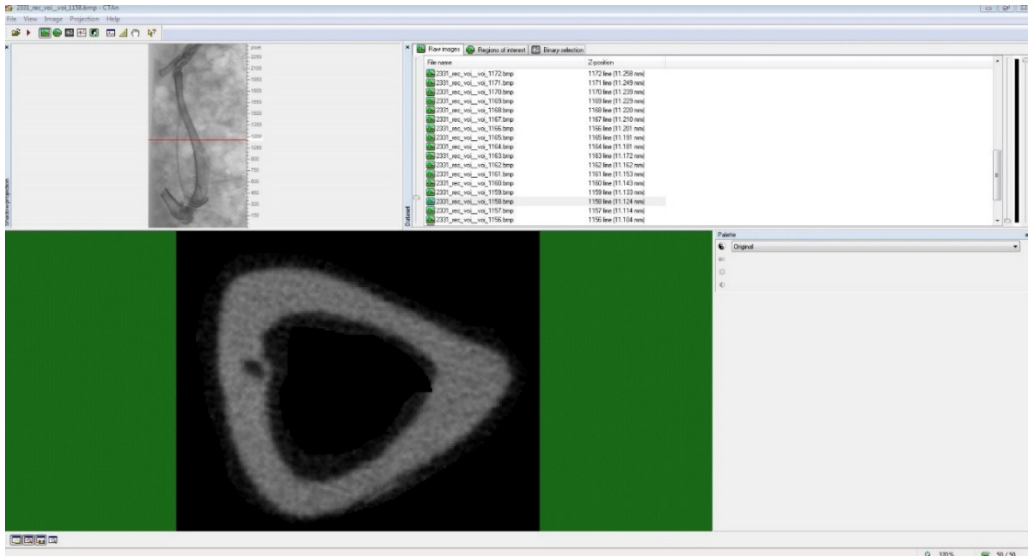

Figure 2-21*: Stack of reconstructed images in CTAn software*

The region of interest was then viewed, and the slices were contoured for the cortical bone analysis as shown in *Figure 2.22*.

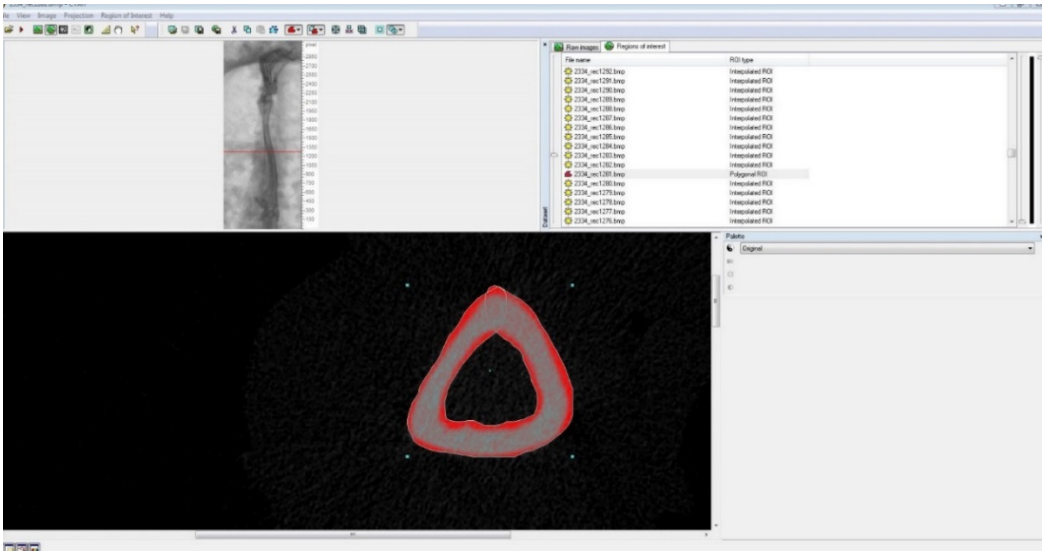

Figure 2-22*: Selection of ROI for cortical bone analysis*

The ROI was saved and then the dataset was opened again for further processing. The images were opened in a binary selection mode and the threshold level was adjusted to a minimum of 55 and to the maximum of 255 as shown in *Figure 2.23.*

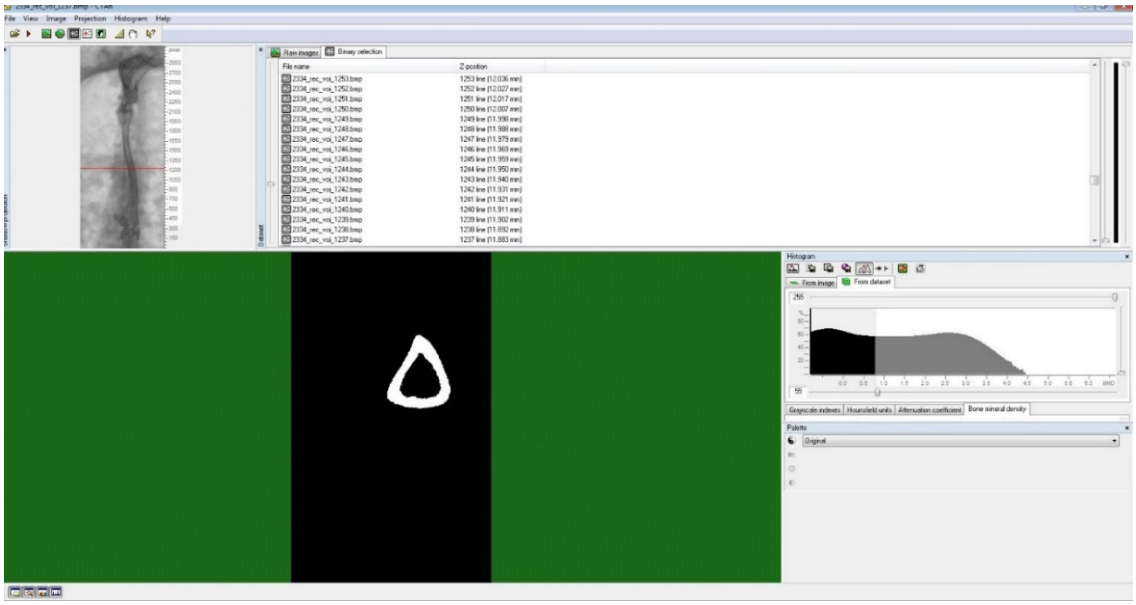

Figure 2-23*: Threshold level adjustment and bone mineral density estimation*

The bone mineral density was saved from the dataset using the save histogram option. The dataset was then opened in a custom processing mode. The task list for the cortical bone analysis was imported for the further processing of data. The sequence of the task performed for the cortical analysis is shown in *Figure 2.24.*

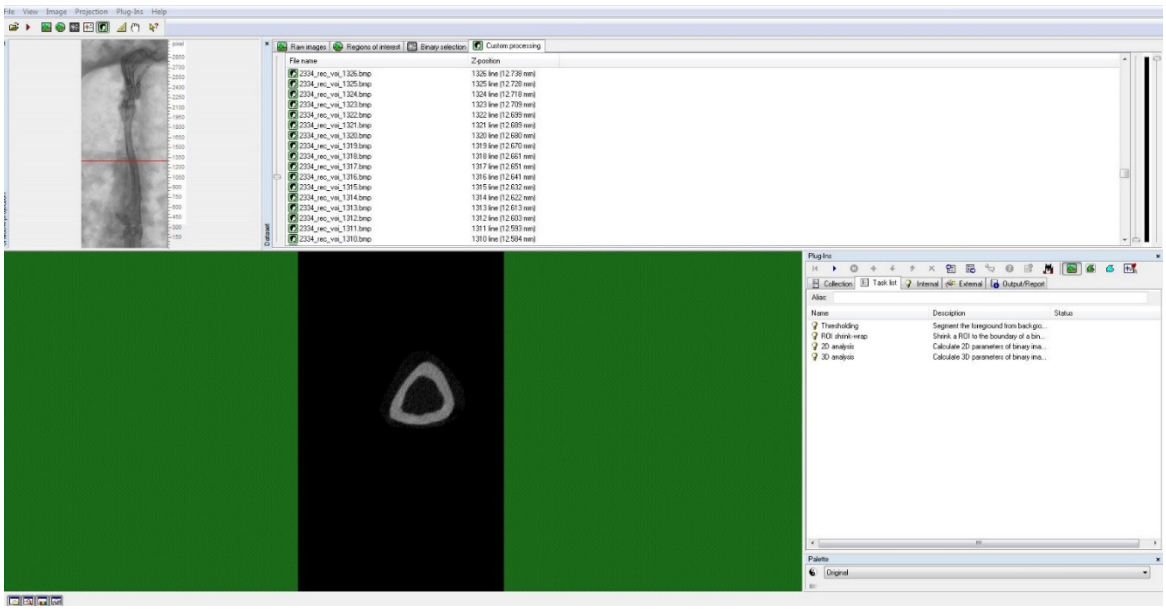

Figure 2-24*: Digital Image Correlation setup*

After the task was finished, the data was saved, and the cortical bone parameters were compiled for the statistical analysis.

2.4.8 Trabecular bone analysis

The stack of the reconstructed images was opened in CTAn software and the range of the slices was selected. We selected 100 slices from the distal femur and the proximal tibia for the trabecular bone analysis as described in *Section 2.4.3*.

The region of interest was then viewed, and the slices were contoured for the trabecular bone analysis as shown in *Figure 2.25*.

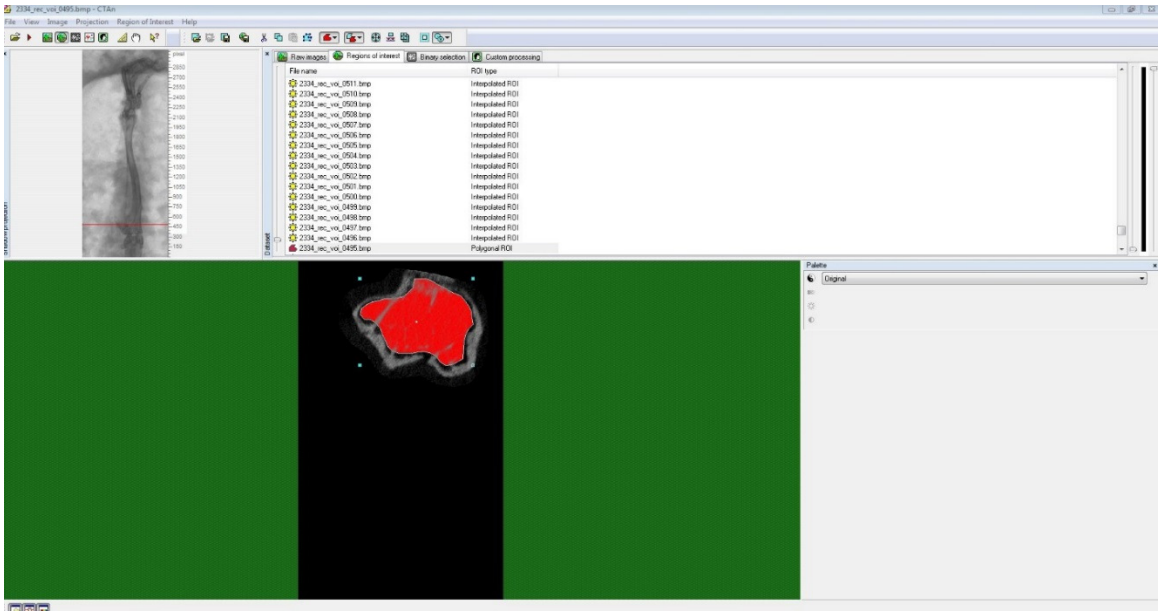

Figure 2-25*: Selection of ROI for trabecular analysis*

The ROI was saved and then the dataset was opened again for further processing. The images were opened in a binary selection mode and the threshold level was adjusted to a minimum of 45 and to the maximum of 95.

The bone mineral density was saved from the dataset using the save histogram option. The dataset was then opened in a custom processing mode. The task list for the trabecular bone analysis was imported for the further processing of data. The sequence of the task performed for the trabecular analysis is shown in *Figure 2.26.*

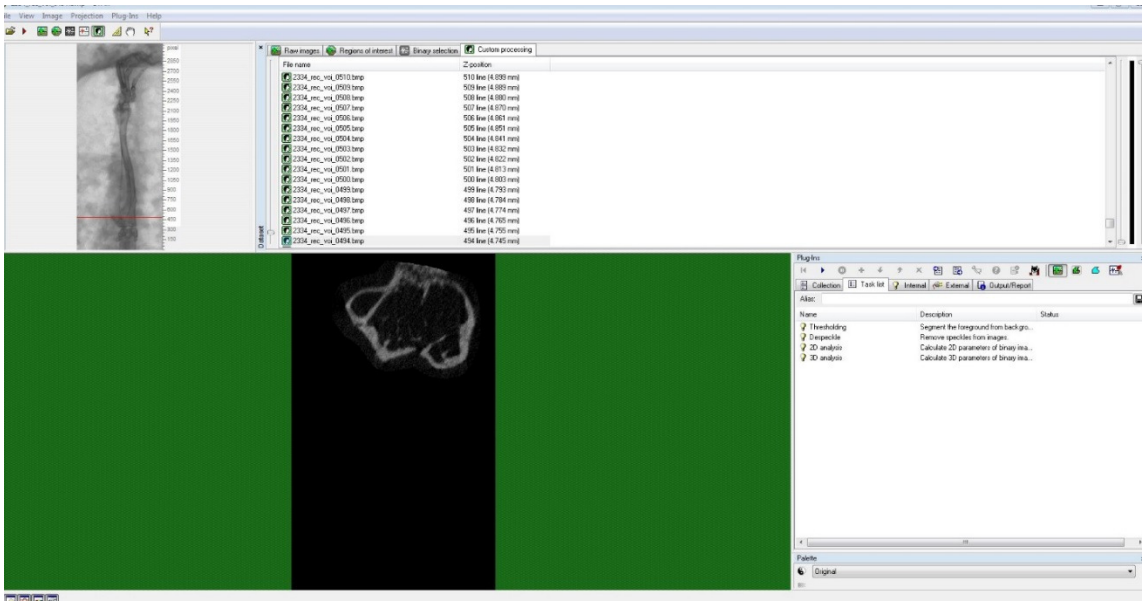

Figure 2-26*: Task list for the trabecular bone analysis*

After the task was finished, the data was saved, and the trabecular bone parameters i.e. bone volume/tissue volume for cortical and trabecular part, bone area were compiled for the statistical analysis.

CHAPTER 3
RESULTS

This chapter includes the data generated by following the methods described in Chapter 2. The strain response was calculated in terms of microstrains from two methods: strain gaging and digital image correlation techniques. The data presented in this chapter shows the comparison of the strains captured from these two different methods and the differences observed in strain response during aging. The biomechanical performance of the bones is presented based on all the parameters listed in *Table-1* calculated from the data obtained from three-point bending test. In the end, micro-CT analysis data is presented to see the correlation of the biomechanical parameters with the structure of the bone, which will be discussed in the next chapter.

3.1 Strain Response in Tibia & Ulna

The strain response (microstrains) was captured using Digital Image Correlation (DIC) system and strain gaging. The peak-to-peak strains were calculated from the middle of the three peak cycles i.e. 19^{th}, 20^{th} and 21^{st} cycle for tibiae and 3^{rd}, 4^{th} and 5^{th} cycle for ulnae. The average of these three strain values was used as the strain experienced on that bone sample. Then average strains for each age group was calculated at each level of load and were compared between the two methods. The effects of aging were also observed. The comparisons between the two methods and between the age groups were made by using linear regression models with robust standard error testing and the significance level was set to 0.05. Significant differences ($p<.05$) are marked with an asterisk (*) in the figures. The corresponding equations from a linear regression analysis are in the box on the left side of each graph corresponds to each age group on the right side, i.e., top equation corresponds to the group listed at the top, middle equation corresponds to the group listed in the middle and bottom equation corresponds

to the group listed at the bottom. The R^2 values represent the regression value, which ranges from zero to one. The slope of equation is used to estimate the stiffness and the negative value does not have any significance because the load in the x-axis are not starting from zero. The testing started with a preload of 0.5 N for the tibia and 0.3 N for the ulnae.

3.1.1 Tibia – Load strain curves

When the load-strain curves obtained from digital image correlation technique (Figure 3-1) were compared with the load-strain curves obtained from strain gaging method (Figure 3-2) in female tibiae at three different levels of load, there were no significant differences observed between the results of the two methods. The slope of the curve represents the flexibility of the bone.

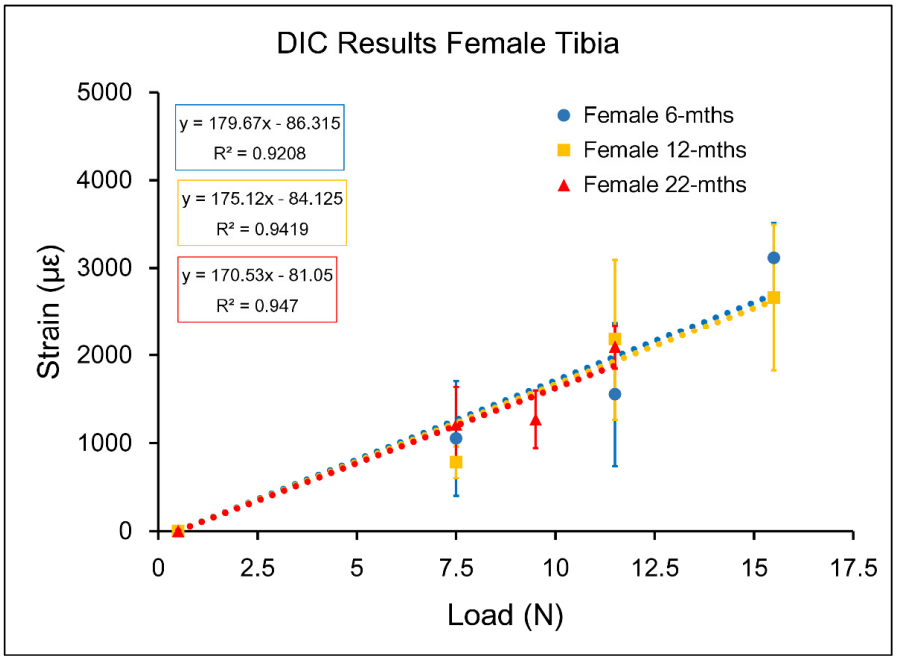

Figure 3-1*: Strains captured by Digital Image Correlation (DIC) in female tibiae*

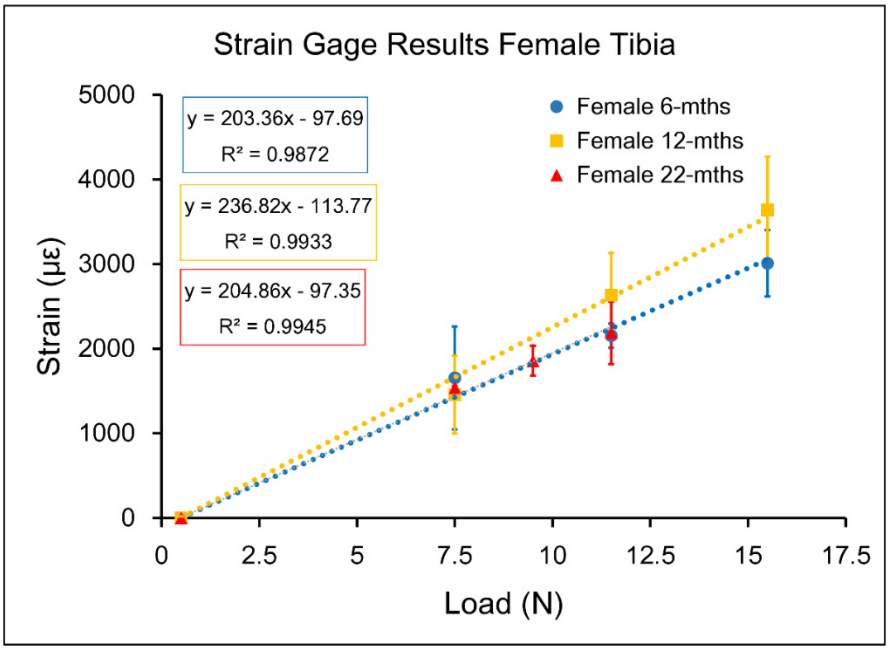

Figure 3-2*: Strains captured by strain gaging in female tibiae*

The load-strain curves obtained from digital image correlation and from strain gaging in male tibiae at three different levels of load are shown in *Figures 3.3* and *3.4* respectively. Like

female tibiae, there were no significant differences observed between the results of two methods in males.

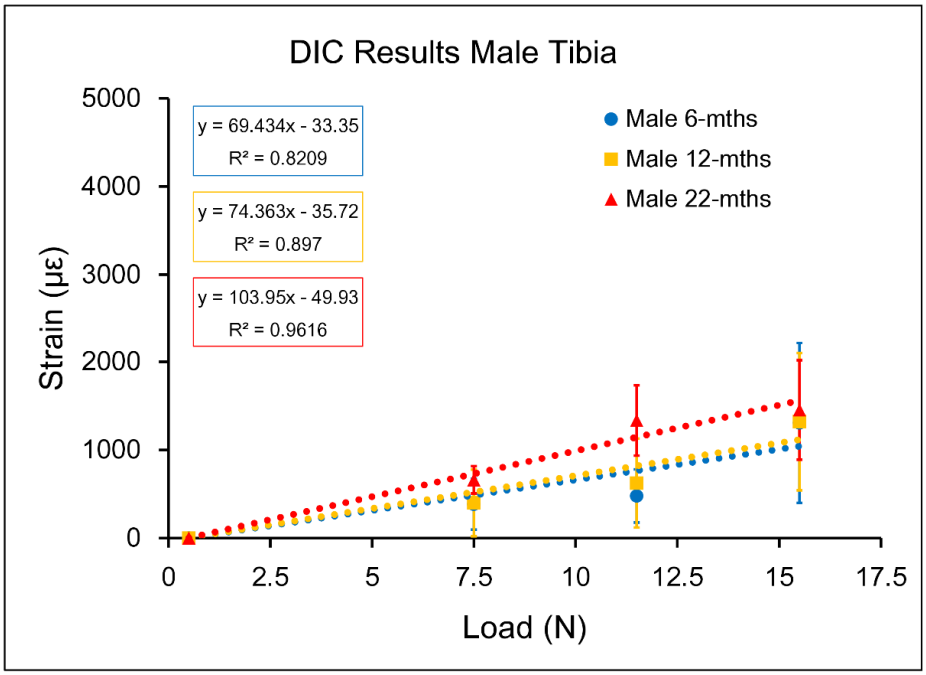

Figure 3-3*: Strains captured by Digital Image Correlation (DIC) in male tibiae*

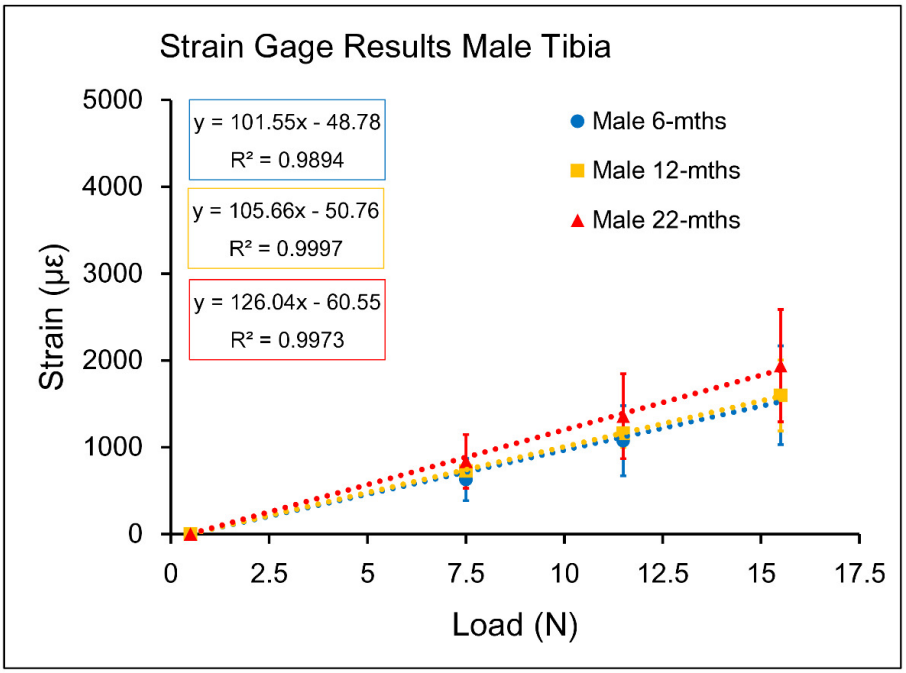

Figure 3-4*: Strains captured by strain gaging in male tibiae*

3.1.2 Ulna – Load strain curves

The load-strain curves obtained from digital image correlation approach (Figure 3-5) can be compared with the load-strain curves obtained from strain gaging method (Figure 3-6) in female ulnae at three different levels of load. The DIC strains are significantly higher at the age of 6 months at lower load (1.3N) only.

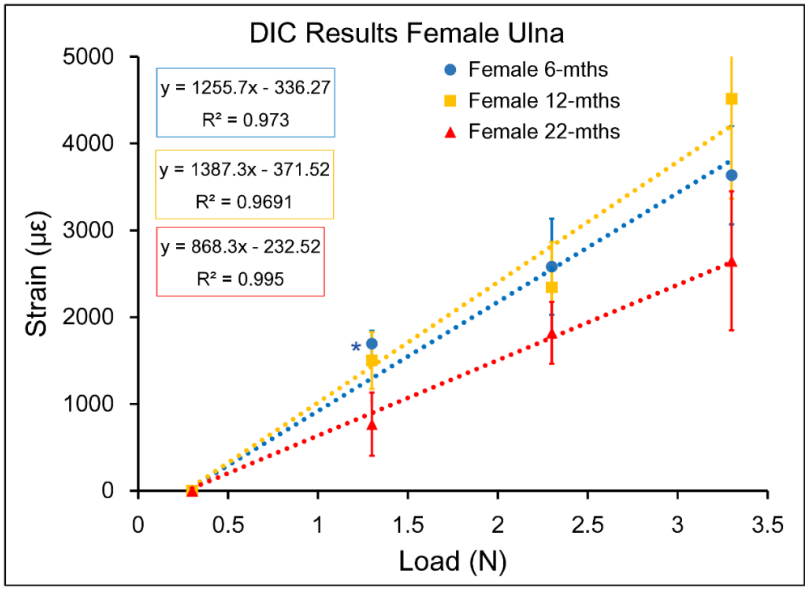

Figure 3-5*: Strains captured by Digital Image Correlation (DIC) in female ulnae*

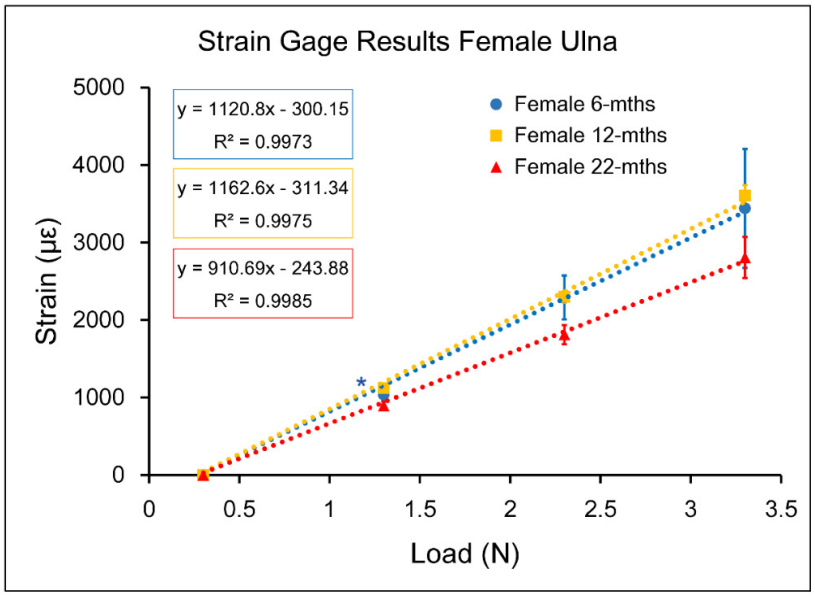

Figure 3-6*: Strains captured by strain gaging in female ulnae*

The load-strain curves obtained from digital image correlation approach and from strain gaging method are shown in *Figures 3.7* and *3.8,* respectively, for male ulnae at three different levels of load. The DIC strains in male ulnae are significantly higher at 6 months at all loads and at 12 months at lower load (1.3N) only.

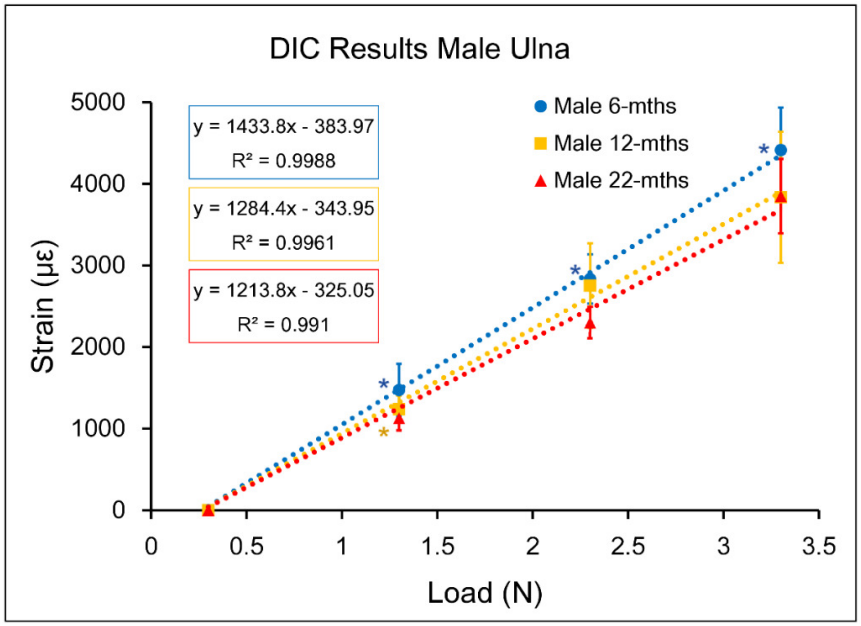

Figure 3-7*: Strains captured by Digital Image Correlation (DIC) in male ulnae*

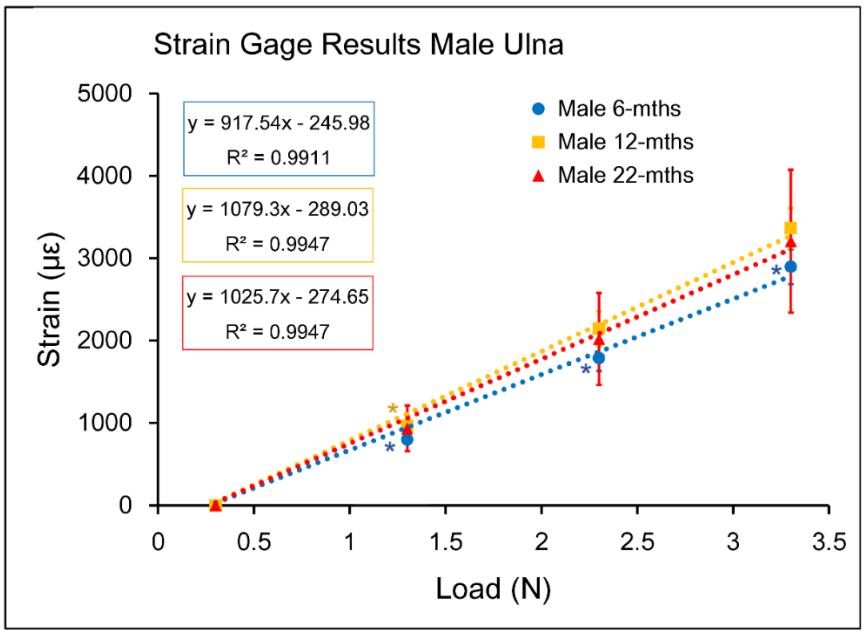

Figure 3-8*: Strains captured by strain gaging in male ulnae*

3.1.3 Tibia – Effects of aging

The aging effects in the strain response (microstrains) of female tibiae at lower (7.5N), medium (11.5N) and higher (15.5N) load are shown in *Figures 3.9*, *3.10 and 3.11* respectively. The strain data for female in the 22 months group in *Figure 3.11* was not included because the samples started to break at the 15.5N load. The strain gaging and DIC data showed no significant changes in female tibiae.

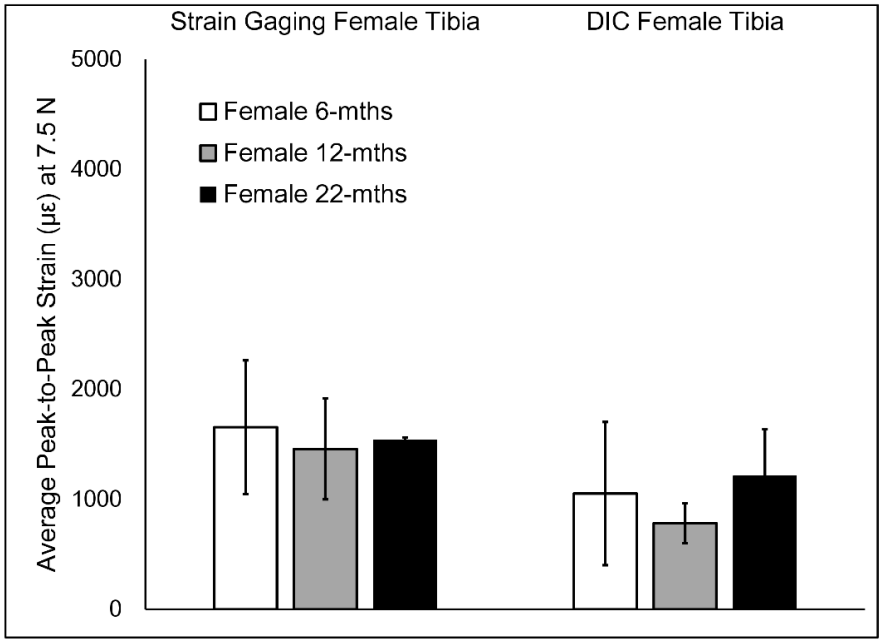

Figure 3-9*: Strains captured at 7.5N in female tibiae*

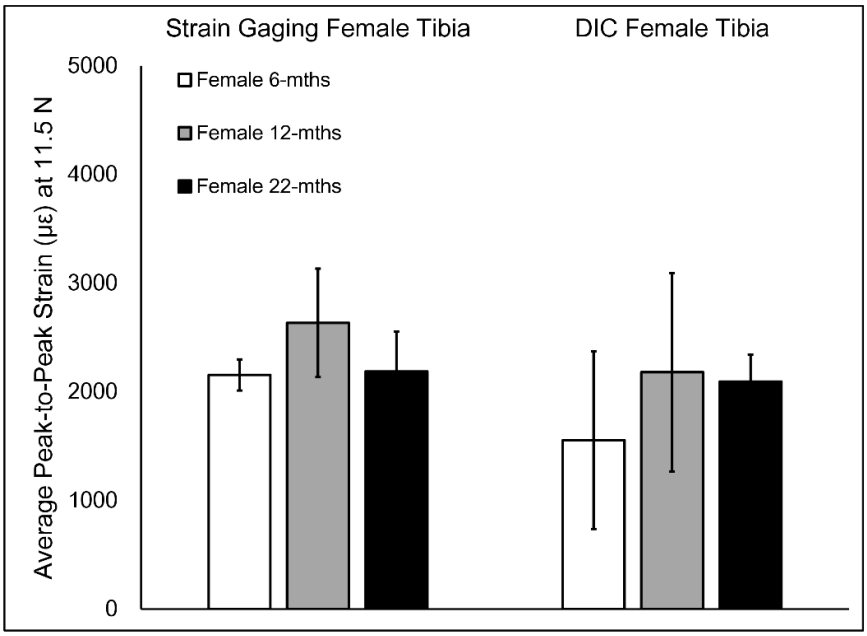

Figure 3-10*: Strains captured at 11.5N in female tibiae*

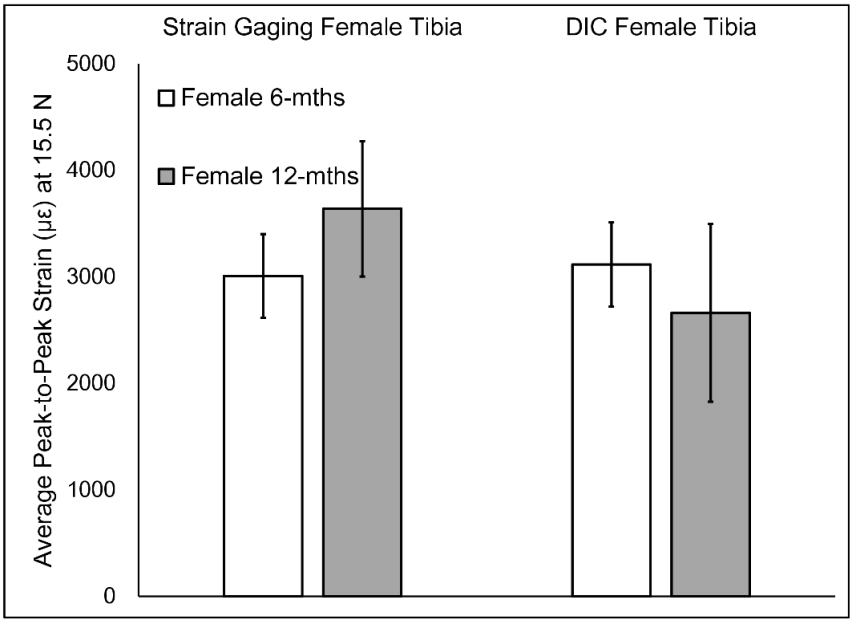

Figure 3-11*: Strains captured at 15.5N in female tibiae*

The aging effects in the strain response (microstrains) of male tibiae at lower (7.5N), medium (11.5N) and higher (15.5N) load are shown in *Figures 3.12*, *3.13* and *3.14,*

respectively. The DIC data showed significant increase in strains from 6 months to 22 months at the load of 11.5N only.

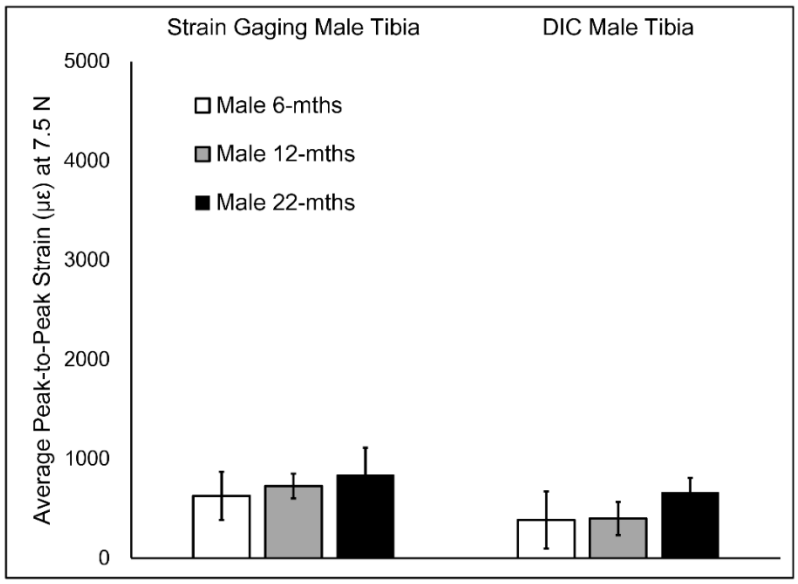

Figure 3-12*: Strains captured at 7.5N in male tibiae*

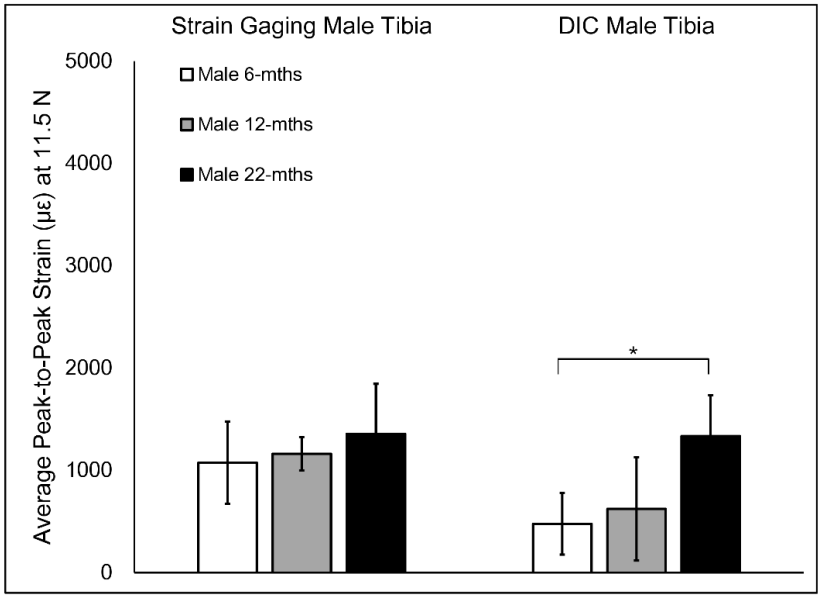

Figure 3-13*: Strains captured at 11.5N in male tibiae*

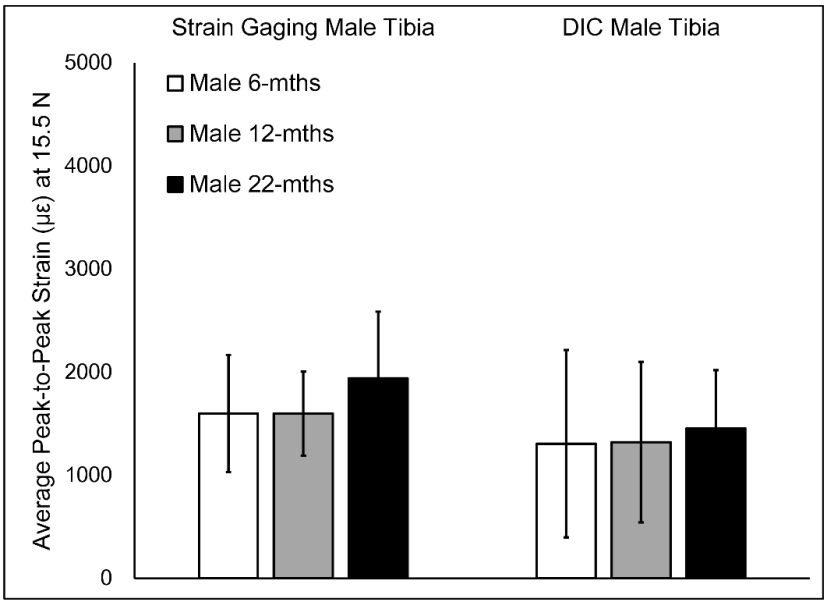

Figure 3-14*: Strains captured at 15.5N in male tibiae*

3.1.4 Ulna – Effects of Aging

The aging effects in the strain response (microstrains) of female ulnae at lower (1.3N), medium (2.3N) and higher (3.3N) load are shown in *Figures 3.15*, *3.16* and *3.17,* respectively. The DIC strains decreased significantly from 6 to 22 months at all the loads while strain gaging data showed siginificant decrease in strains from 6 to 22 months at 2.3N load only.

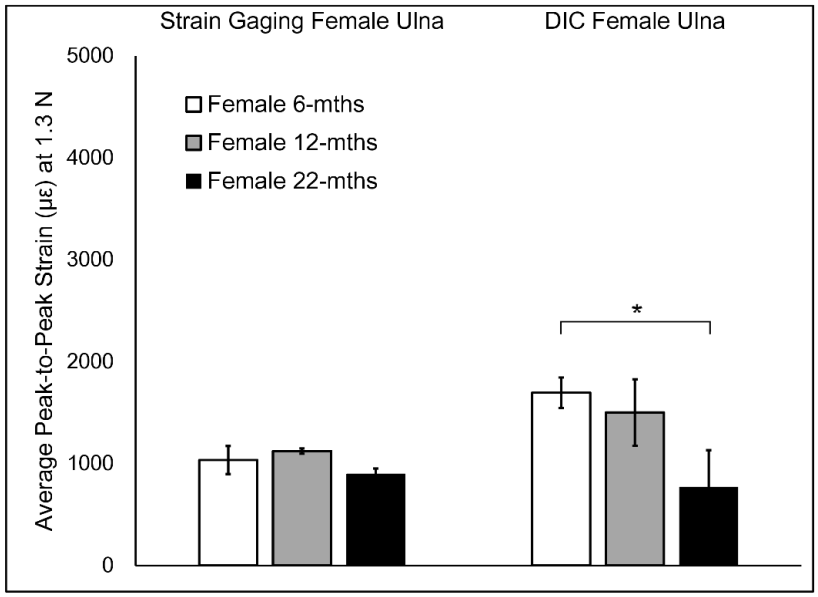

Figure 3-15*: Strains captured at 1.3N in female ulnae*

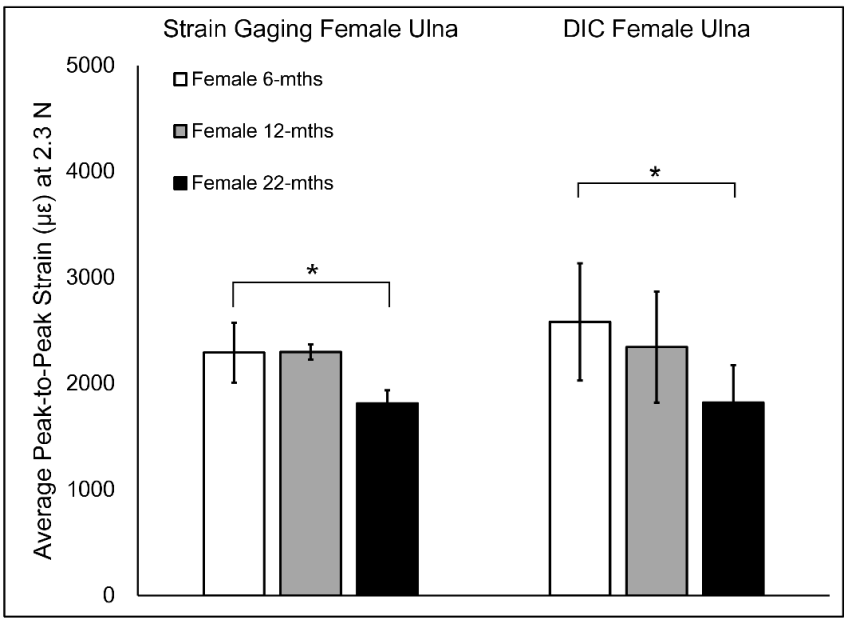

Figure 3-16*: Strains captured at 2.3N in female ulnae*

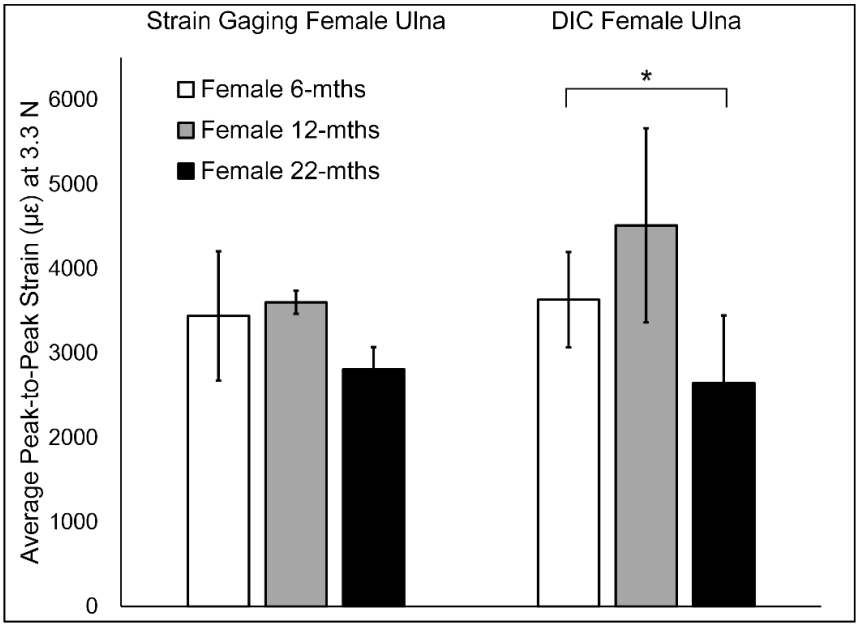

Figure 3-17*: Strains captured at 3.3N in female ulnae*

The aging effects in the strain response (microstrains) of male ulnae at lower (1.3N), medium (2.3N) and higher (3.3N) load are shown in *Figures 3.18, 3.19 and 3.20,* respectively.

The DIC strains decreased significantly from 6 to 22 months 1.3N and 2.3N loads while strain gaging data showed siginificant increase in strains from 6 to 22 months at 1.3N and 3.3N load.

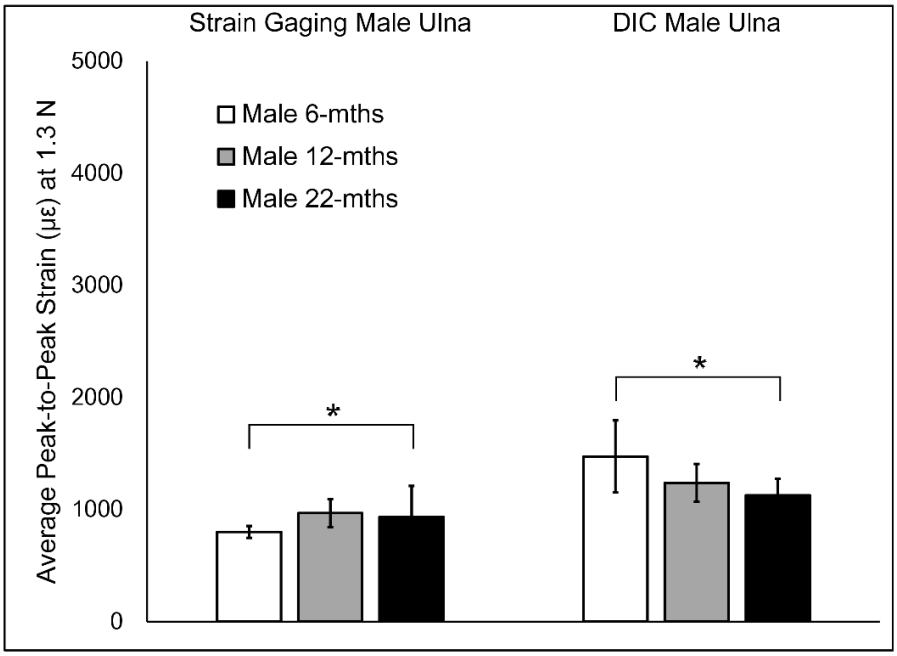

Figure 3-18*: Strains captured at 1.3N in male ulnae*

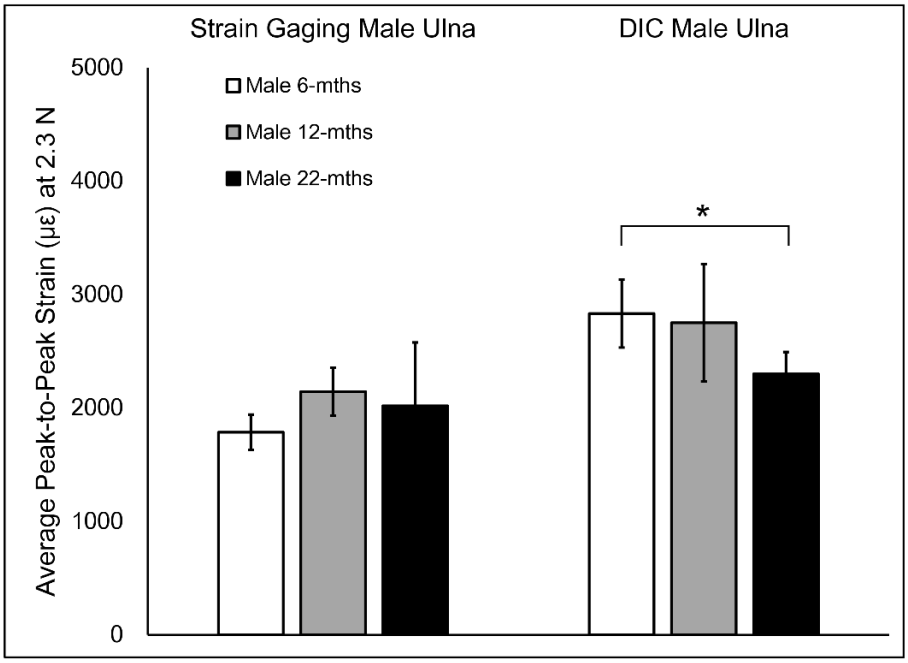

Figure 3-19*: Strains captured at 2.3N in male ulnae*

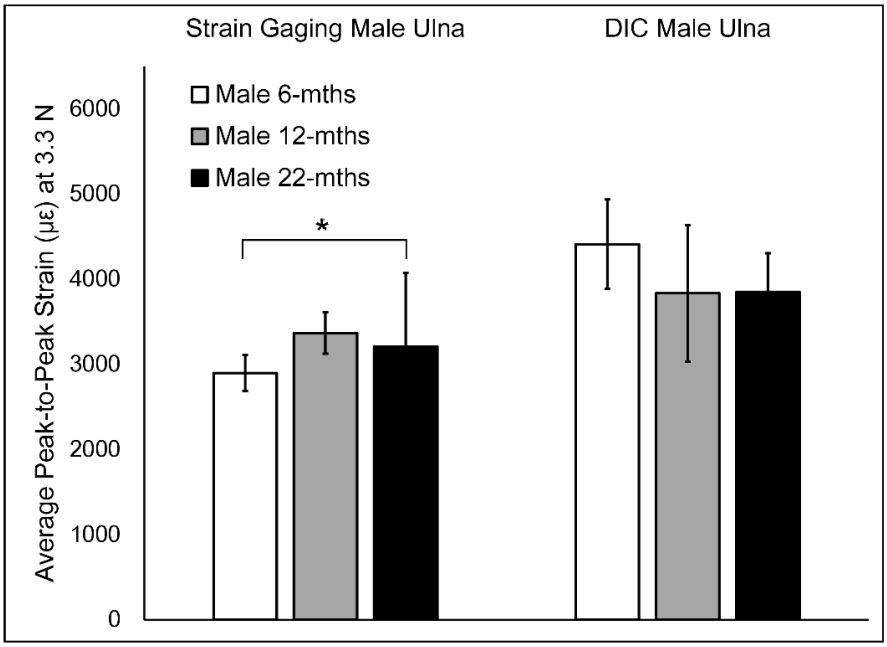

Figure 3-20*: Strains captured at 3.3N in male ulnae*

3.2 Biomechanical Parameters in Female Femur, Tibia & Ulna

The biomechanical parameters were determined by three-point bending test on each bone sample. The methods are described in *Section 2.3* of Chapter 2. Statistics were done using a linear regression model with robust standard error testing and significance level set to 0.05. Differences observed in 12 and 22 months in each parameter with reference to 6 months group are marked with an asterisk (*) on the graph. The following biomechanical parameters were calculated to assess the quality of the bone and are illustrated using the bar charts.

Table 1*: List of Biomechanical parameters*

Biomechanical Parameter	**Unit**
Ultimate Load **(UL)**	N
Elastic Stiffness **(ES)**	N/mm
Moment of Inertia **(MOI)**	mm^4
Modulus of elasticity **(E)**	GPa
Total work to failure **(WTF)**	mJ
Elastic work to failure **(EWTF)**	mJ
Plastic work to failure **(PWTF)**	mJ
Elastic displacement **(EDISP)**	mm
Post yield displacement **(PYD)**	mm
Compressive strength **(CST)**	N/mm^2
Tensile strength **(TST)**	N/mm^2

3.2.1 Ultimate load

The ultimate load in female femurs, tibiae and ulnae is shown in *Figures 3.21, 3.22 and 3.23,* respectively. In female femurs and tibiae, ultimate load decreased significantly at 22 months compared to 6 months while ulnae showed no differences.

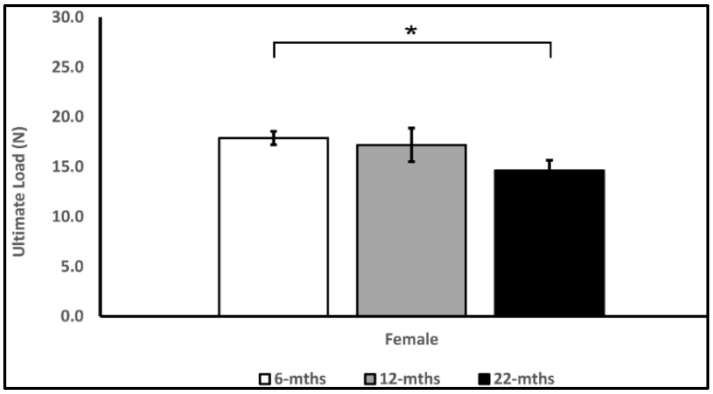

Figure 3-21*: Ultimate Load in female femurs*

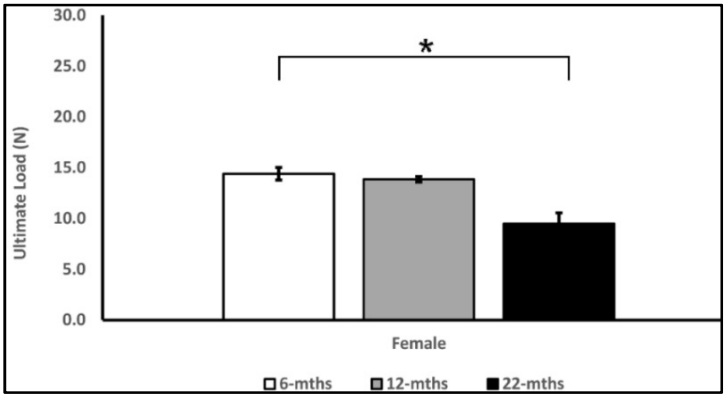

Figure 3-22*: Ultimate Load in female tibiae*

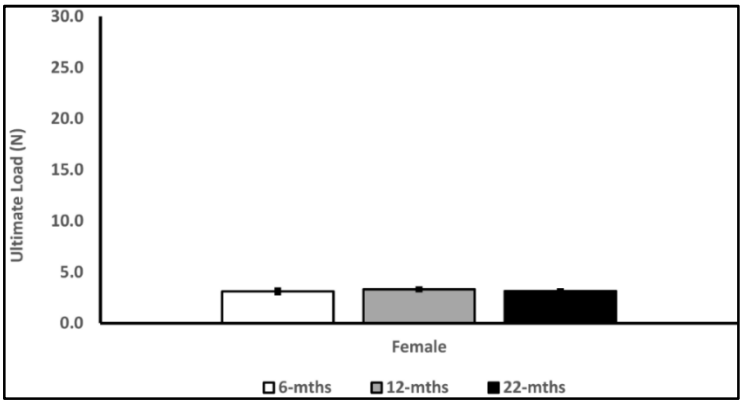

Figure 3-23*: Ultimate Load in female ulnae*

3.2.2 Elastic stiffness

The elastic stiffness in female femurs, tibiae and ulnae is shown in *Figures 3.24, 3.25 and 3.26,* respectively. In female tibiae, elastic stiffness decreased from 6 months to 22 months, while it increased in ulnae from 6 months to 22 months. No change was observed in female femurs.

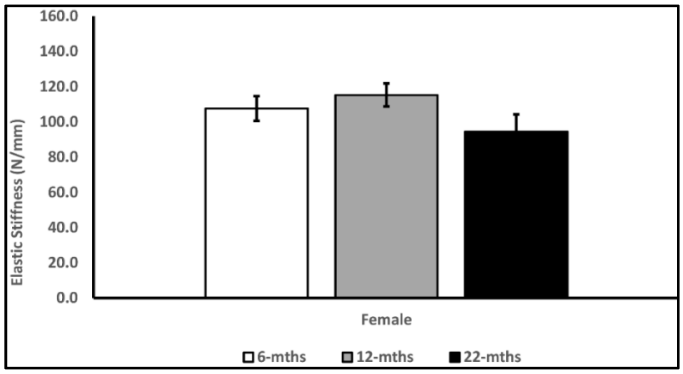

Figure 3-24*: Elastic Stiffness in female femurs*

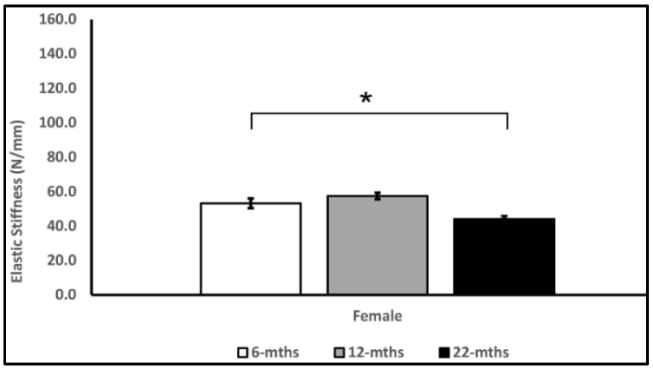

Figure 3-25*: Elastic Stiffness in female tibiae*

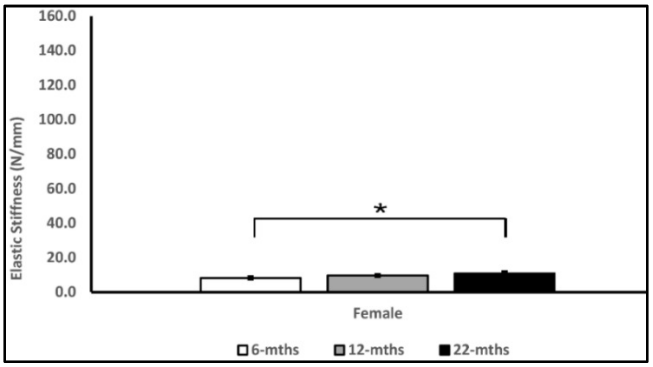

Figure 3-26*: Elastic Stiffness in female ulnae*

3.2.3 Modulus of elasticity

The modulus of elasticity in female femurs, tibiae and ulnae is shown in *Figures 3.27, 3.28 and 3.29,* respectively. In female femurs, modulus of elasticity decreased from 6 months to 22 months while it increased in ulnae from 6 months to 12 and 22 months. There was no change observed in female tibiae.

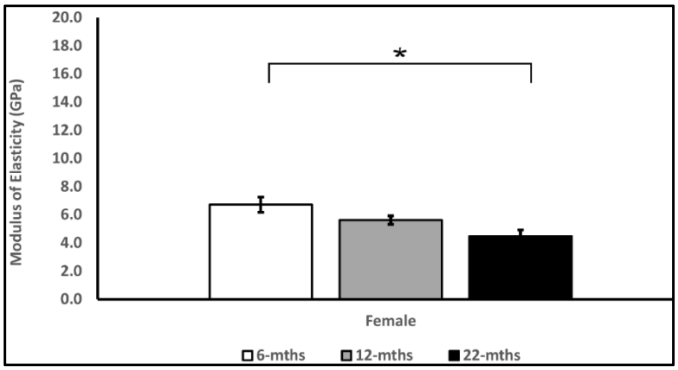

Figure 3-27*: Modulus of Elasticity in female femurs*

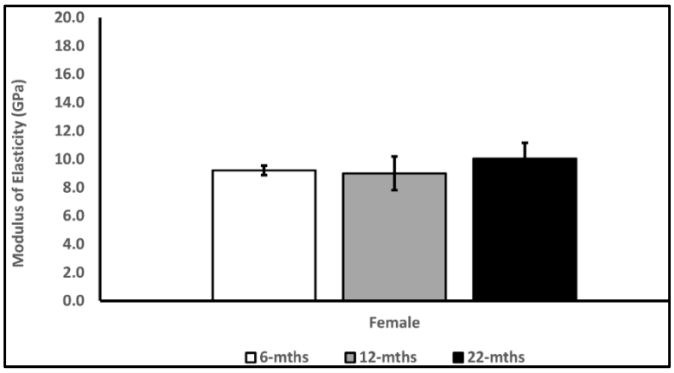

Figure 3-28*: Modulus of Elasticity in female tibiae*

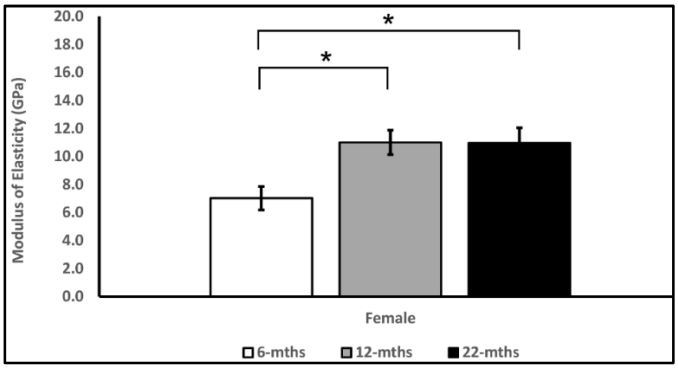

Figure 3-29*: Modulus of Elasticity in female ulnae*

3.2.4 Moment of inertia

Moment of inertia in female femurs, tibiae and ulnae is shown in *Figures 3.30, 3.31 and 3.32,* respectively. Female tibiae and ulnae showed no change while female femurs showed that moment of inertia increased significantly at 12 months compared to 6 months.

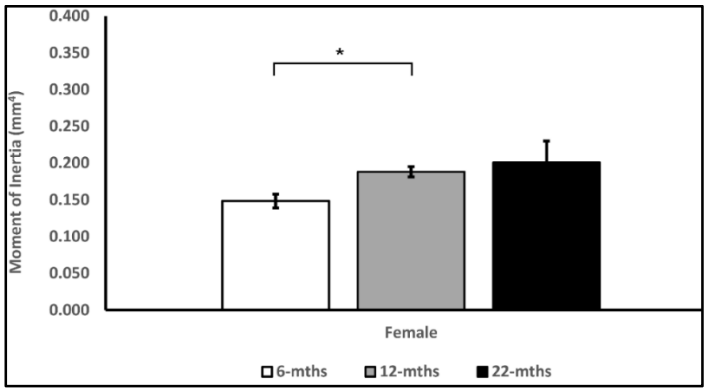

Figure 3-30*: Moment of Inertia in female femurs*

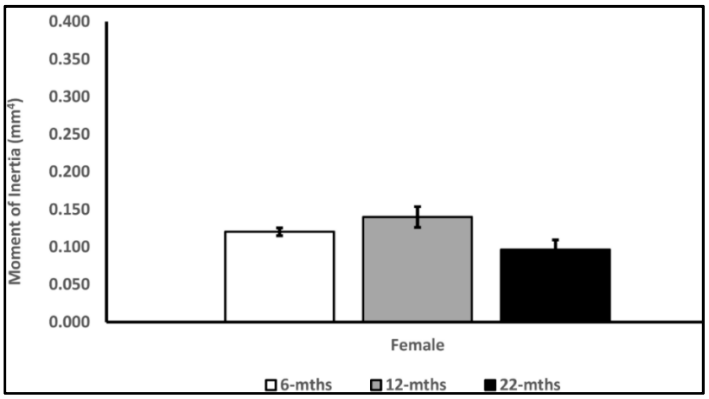

Figure 3-31*: Moment of Inertia in female tibiae*

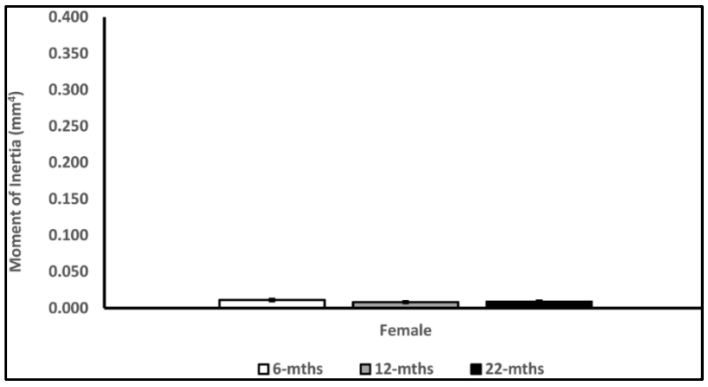

Figure 3-32*: Moment of Inertia in female ulnae*

3.2.5 Total work to failure

Total work to failure in female femurs, tibiae and ulnae is shown in *Figures 3.33, 3.34 and 3.35,* respectively. Female femurs and tibiae showed decrease in total work to failure from 6 months to 22 months while ulnae showed that total work to failure decreased significantly in 12 and 22 months compared to 6 months.

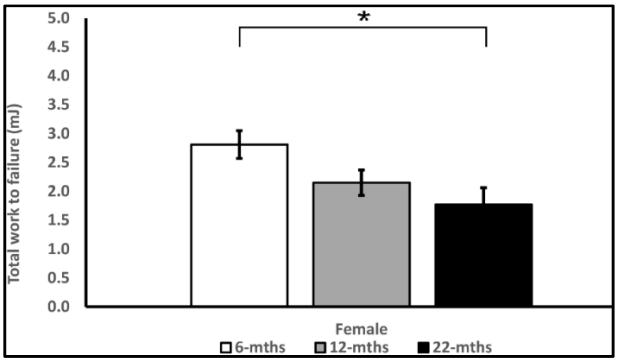

Figure 3-33*: Total work to failure in female femurs*

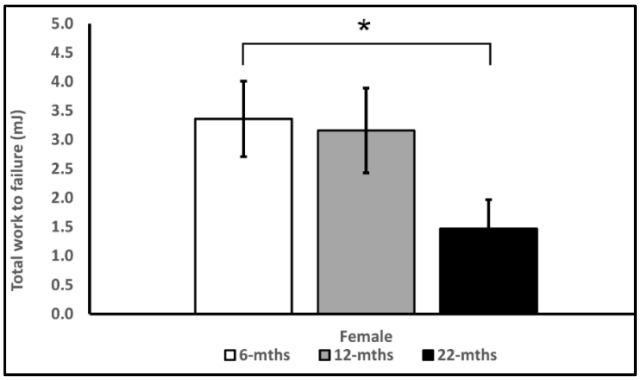

Figure 3-34*: Total work to failure in female tibiae*

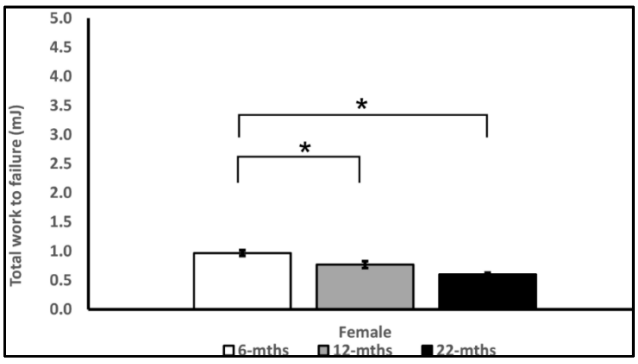

Figure 3-35*: Total work to failure in female ulnae*

3.2.6 Elastic work to failure

Elastic work to failure in female femurs, tibiae and ulnae is shown in *Figures 3.36, 3.37 and 3.38,* respectively. Female femurs showed no change while in tibiae, elastic work to failure decreased from 6 months to 12 and 22 months. In female ulnae, elastic work to failure increased significantly from 6 months to 12 months.

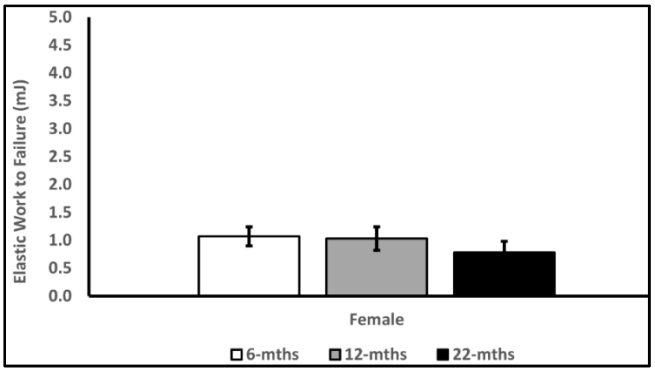

Figure 3-36*: Elastic work to failure in female femurs*

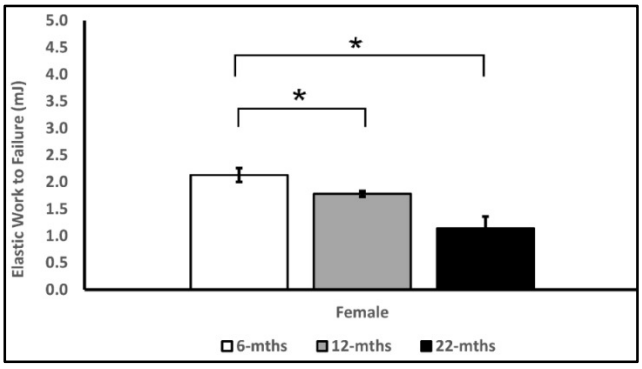

Figure 3-37*: Elastic work to failure in female tibiae*

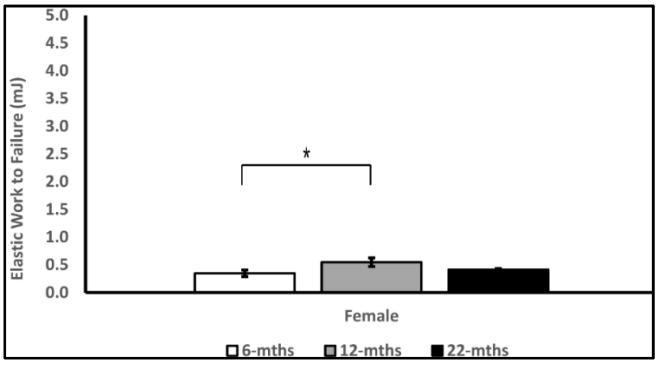

Figure 3-38*: Elastic work to failure in female ulnae*

3.2.7 Plastic work to failure

Plastic work to failure in female femurs, tibiae and ulnae is shown in *Figures 3.39, 3.40 and 3.41,* respectively. Female femurs and tibiae showed no change while in female ulnae, plastic work to failure decreased significantly from 6 months to 12 and 22 months.

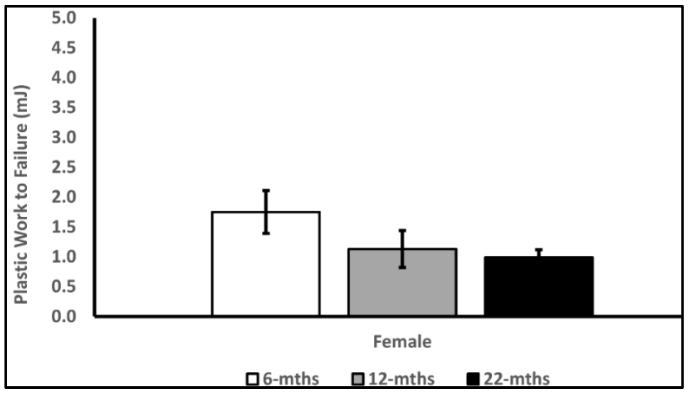

Figure 3-39*: Plastic work to failure in female femurs*

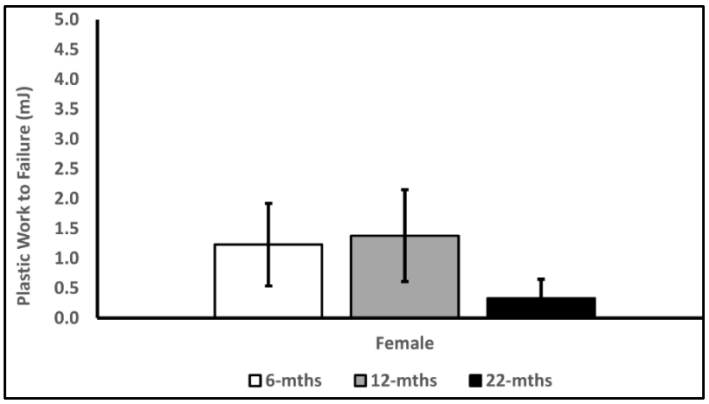

Figure 3-40*: Plastic work to failure in female tibiae*

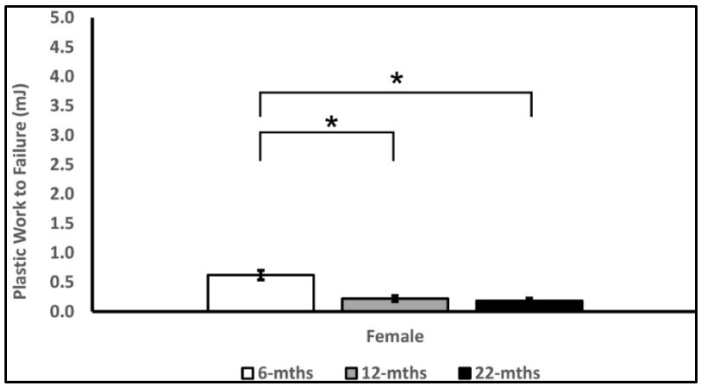

Figure 3-41*: Plastic work to failure in female ulnae*

3.2.8 Elastic displacement

Elastic displacement in female femurs, tibiae and ulnae is shown in *Figures 3.42, 3.43 and 3.44,* respectively. Female femurs and ulnae showed no change while in tibiae, elastic displacement decreased significantly from 6 months to 12 and 22 months.

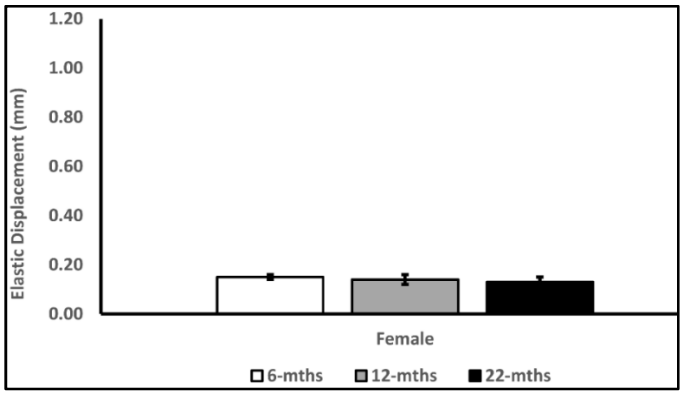

Figure 3-42*: Elastic displacement in female femurs*

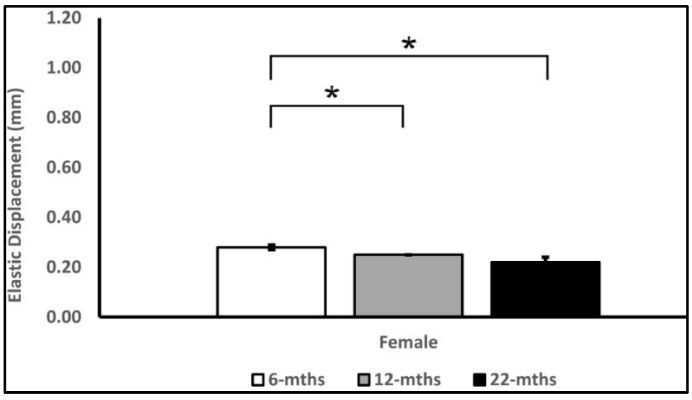

Figure 3-43*: Elastic displacement in female tibiae*

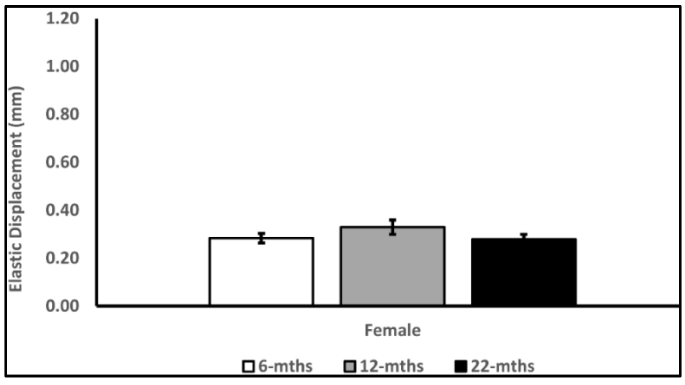

Figure 3-44*: Elastic displacement in female ulnae*

3.2.9 Post yield displacement

Post yield displacement in female femurs, tibiae and ulnae is shown in *Figures 3.45, 3.46 and 3.47,* respectively. Female femurs and tibiae showed no change while in female ulnae, post yield displacement decreased significantly from 6 months to 12 and 22 months.

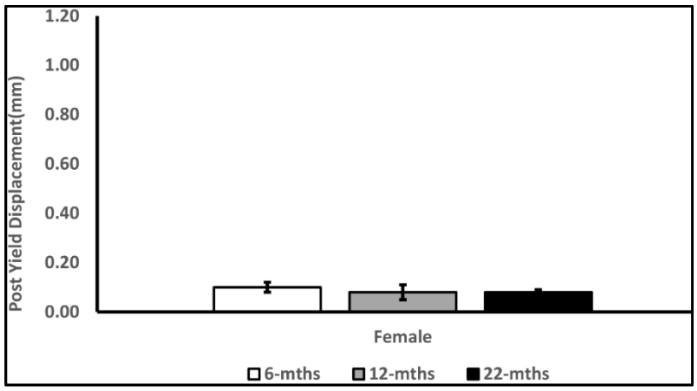

Figure 3-45*: Post yield displacement in female femurs*

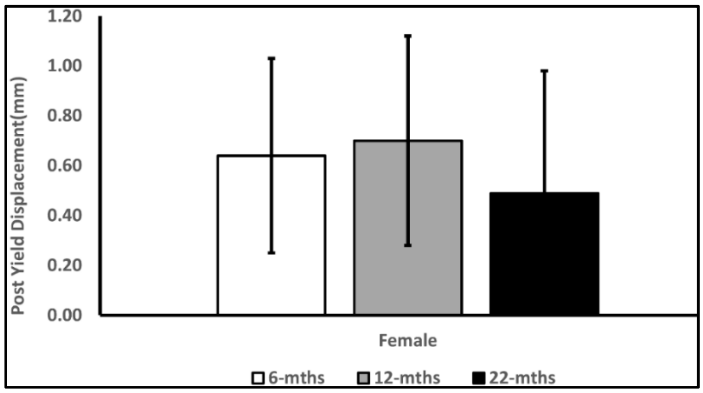

Figure 3-46*: Post yield displacement in female tibiae*

Figure 3-47*: Post yield displacement in female ulnae*

3.2.10 Compressive strength

Compressive strength in female femurs, tibiae and ulnae is shown in *Figures 3.48, 3.49 and 3.50,* respectively. In female femurs, compressive strength decreased at 12 months compared to 6 months, while in ulnae it increased at 12 months compared to 6 months. In tibiae, compressive strength decreased significantly at 22 months compared to 6 months.

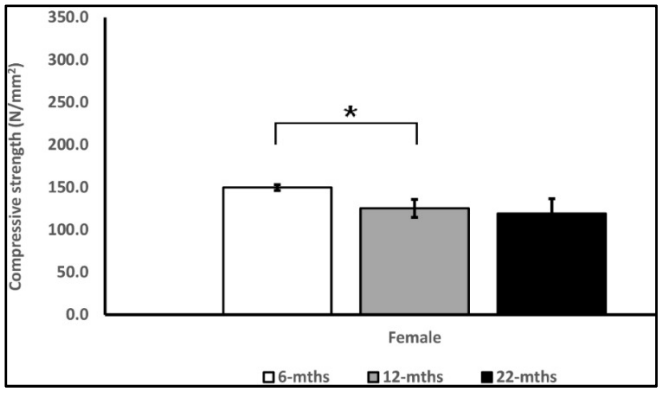

Figure 3-48*: Compressive Strength in female femurs*

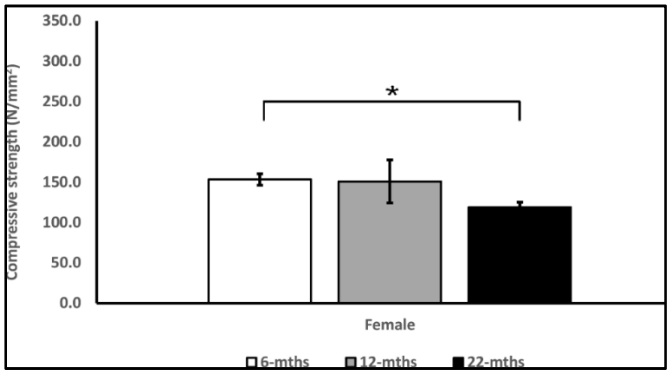

Figure 3-49*: Compressive Strength in female tibiae*

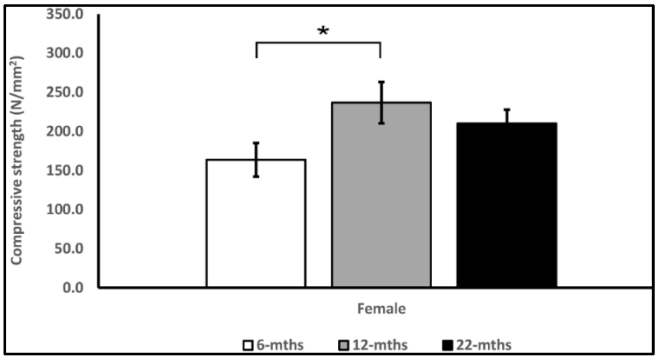

Figure 3-50*: Compressive Strength in female ulnae*

3.2.11 Tensile strength

Tensile strength in female femurs, tibiae and ulnae is shown in *Figures 3.51, 3.52 and 3.53,* respectively. In female femurs, tensile strength decreased significantly at 12 and 22 months of age compared to 6 months. In female ulnae, tensile strength increased at 12 months while in tibiae, no differences were observed.

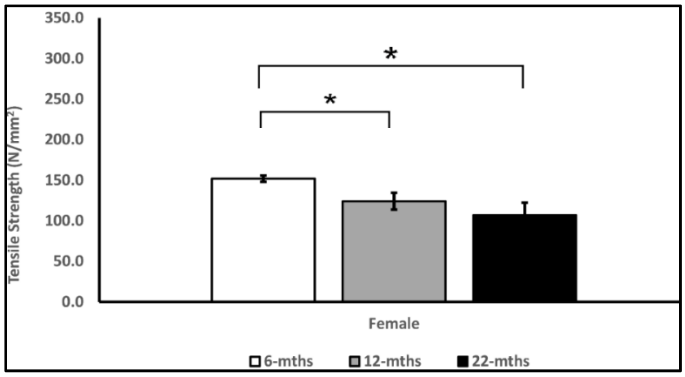

Figure 3-51*: Tensile Strength in female femurs*

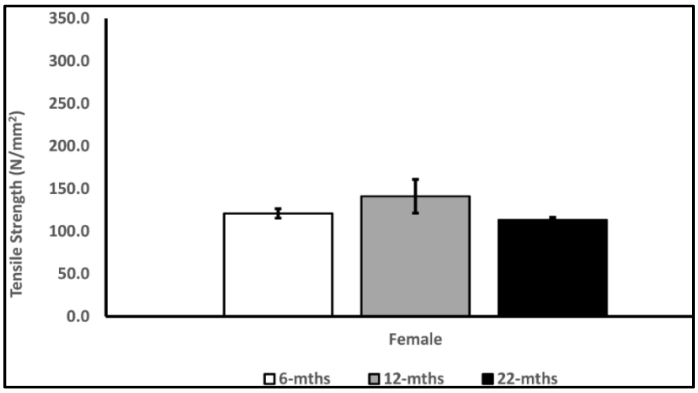

Figure 3-52*: Tensile Strength in female tibiae*

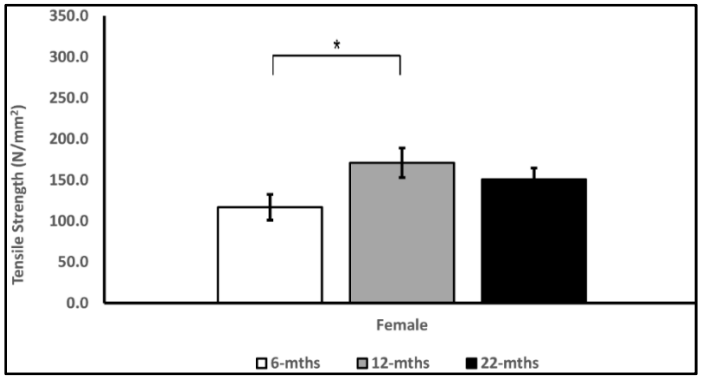

Figure 3-53*: Tensile Strength in female ulnae*

3.3 Biomechanical Parameters in Male Femur, Tibia & Ulna

3.3.1 Ultimate load

The ultimate load in male femurs, tibiae and ulnae is shown in *Figures 3.54, 3.55 and 3.56,* respectively. In male femurs and tibiae, ultimate load decreased significantly at 22 months compared to 6 months while ulnae showed no differences.

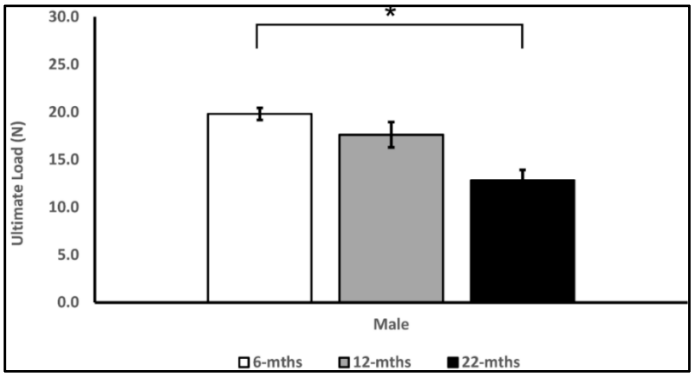

Figure 3-54*: Ultimate Load in male femurs*

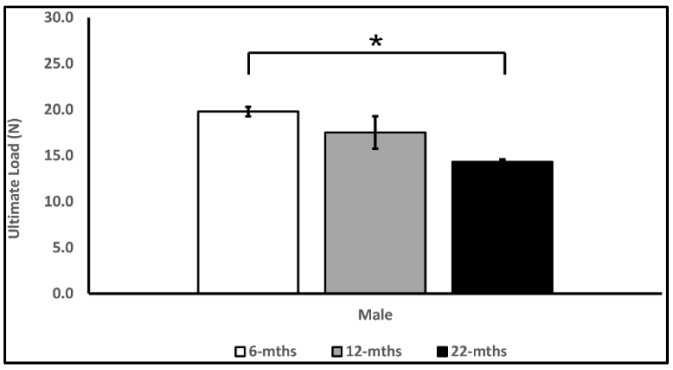

Figure 3-55*: Ultimate Load in male tibiae*

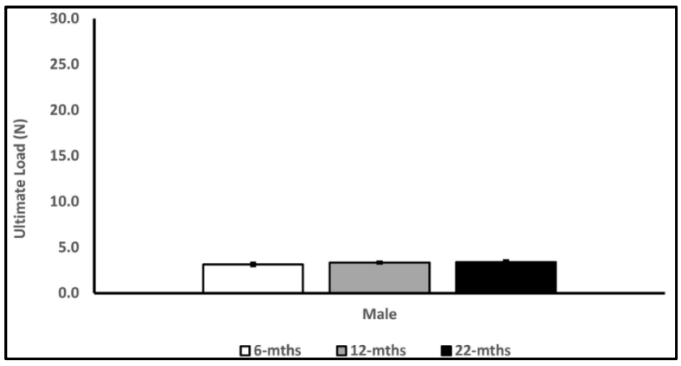

Figure 3-56*: Ultimate Load in male ulnae*

3.3.2 Elastic stiffness

The elastic stiffness in male femurs, tibiae and ulnae is shown in *Figures 3.57, 3.58 and 3.59,* respectively. In male femurs and tibiae, elastic stiffness decreased from 6 months to 12 and 22 months, while there was no change observed in male ulnae.

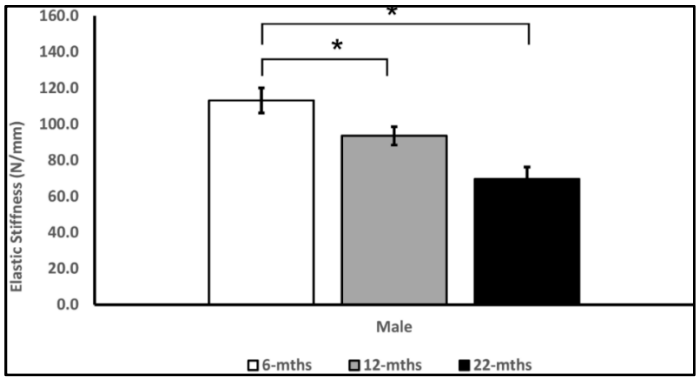

Figure 3-57*: Elastic Stiffness in male femurs*

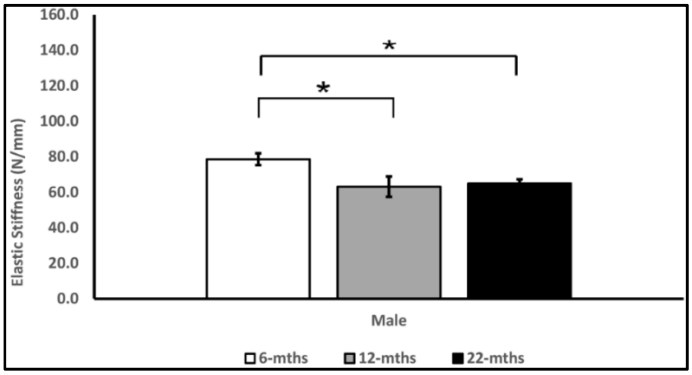

Figure 3-58*: Elastic Stiffness in male tibiae*

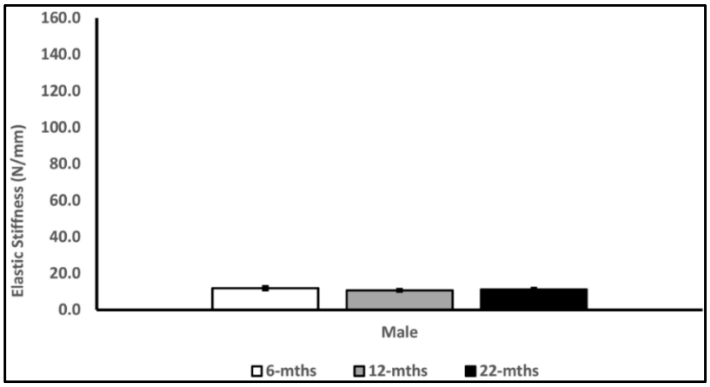

Figure 3-59*: Elastic Stiffness in male ulnae*

3.3.3 Modulus of elasticity

The modulus of elasticity in male femurs, tibiae and ulnae is shown in *Figures 3.60, 3.61 and 3.62,* respectively. In male femurs, modulus of elasticity decreased from 6 months to 22 months while there was no change observed in male tibiae and ulnae.

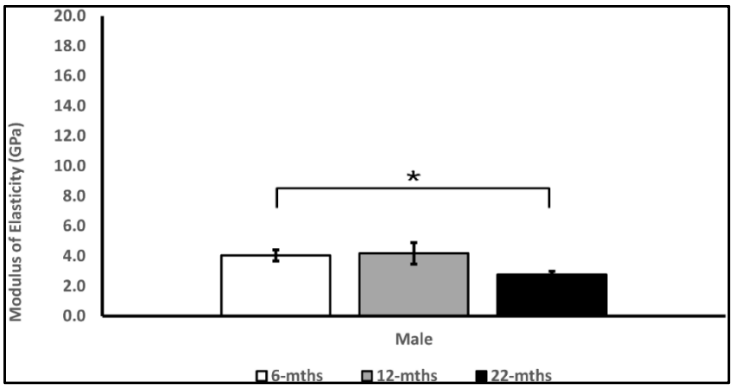

Figure 3-60*: Modulus of Elasticity in male femurs*

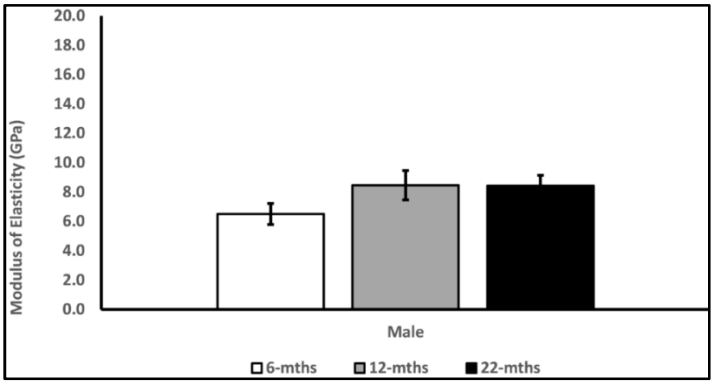

Figure 3-61*: Modulus of Elasticity in male tibiae*

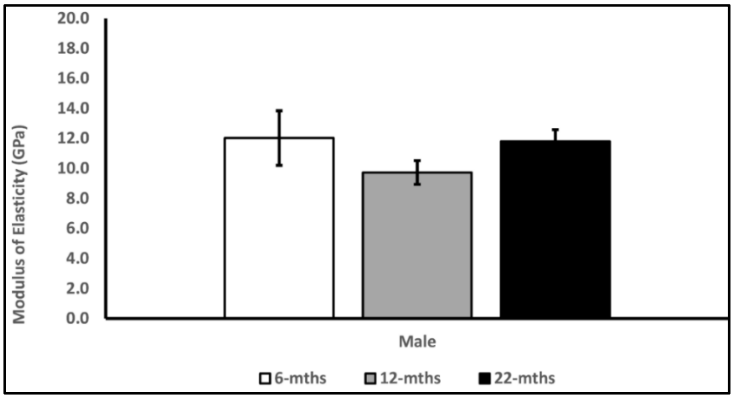

Figure 3-62*: Modulus of Elasticity in male ulnae*

3.3.4 Moment of inertia

The moment of inertia in male femurs, tibiae and ulnae is shown in *Figures 3.63, 3.64 and 3.65,* respectively. Male femurs and ulnae showed no change while male tibiae showed that moment of inertia decreased significantly at 12 and 22 months compared to 6 months.

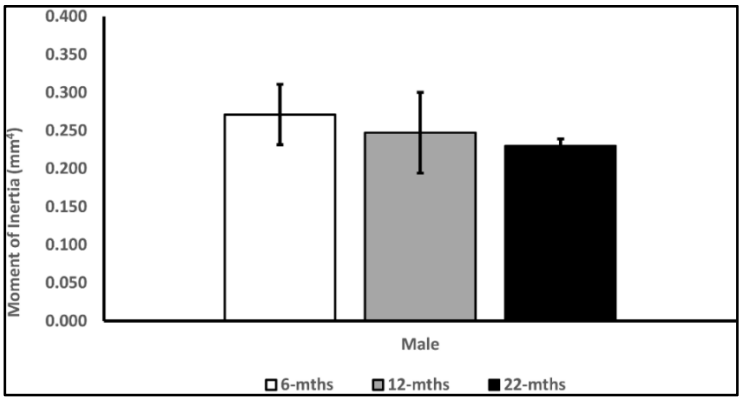

Figure 3-63*: Moment of Inertia in male femurs*

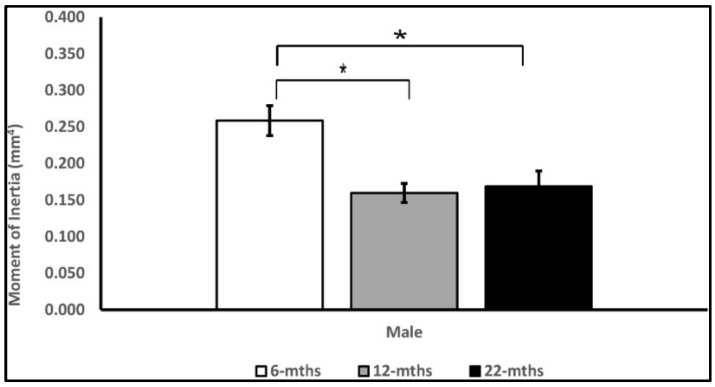

Figure 3-64*: Moment of Inertia in male tibiae*

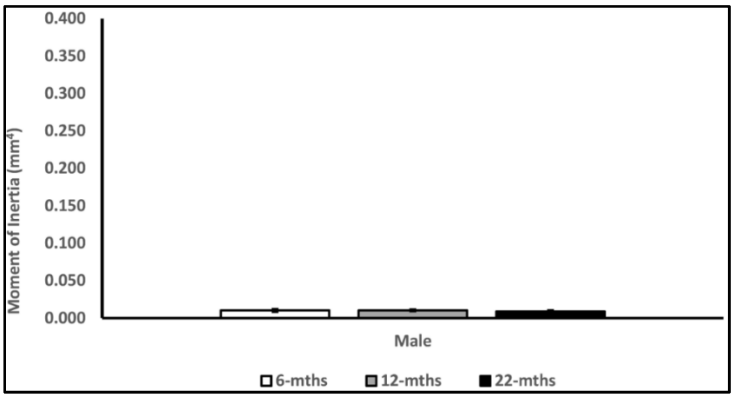

Figure 3-65*: Moment of Inertia in male ulnae*

3.3.5 Total work to failure

Total work to failure in male femurs, tibiae and ulnae is shown in *Figures 3.66, 3.67 and 3.68,* respectively. Male femurs and tibiae showed a decrease in total work to failure from 6 months to 22 months while ulnae showed no differences.

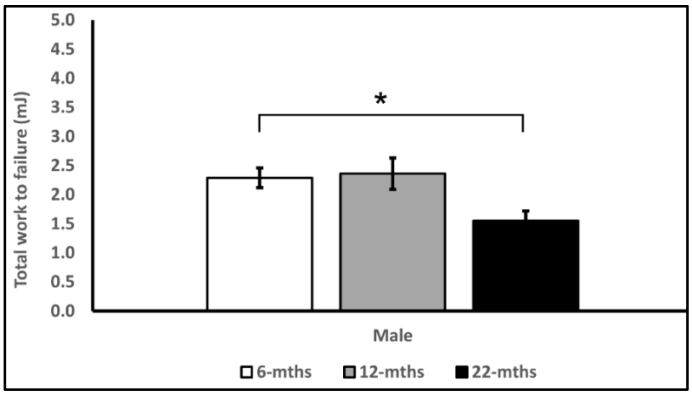

Figure 3-66*: Total work to failure in male femurs*

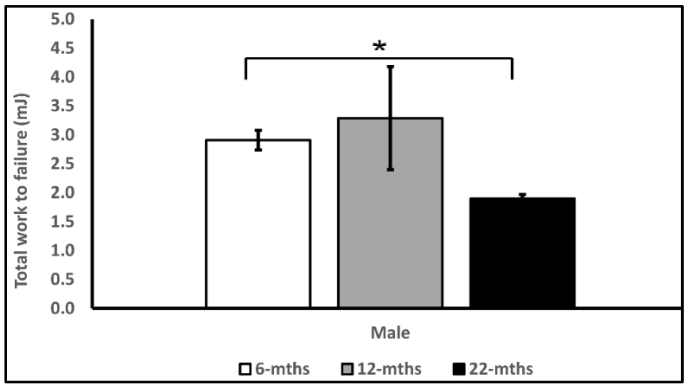

Figure 3-67*: Total work to failure in male tibiae*

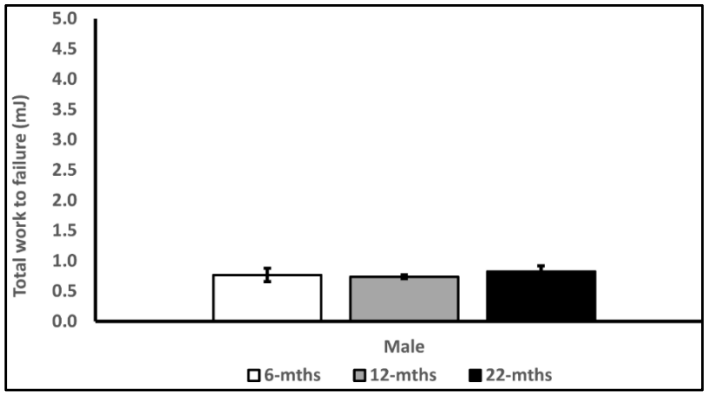

Figure 3-68*: Total work to failure in male ulnae*

3.3.6 Elastic work to failure

Elastic work to failure in male femurs, tibiae and ulnae is shown in *Figures 3.69, 3.70 and 3.71,* respectively. Male femurs and tibiae showed that elastic work to failure decreased from 6 months to 22 months. In male ulnae, elastic work to failure increased significantly from 6 months to 12 months.

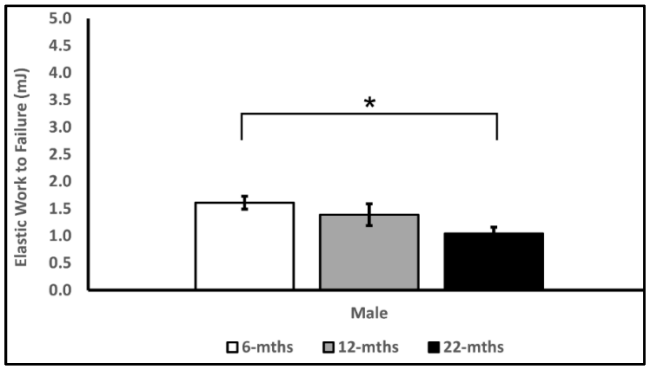

Figure 3-69*: Elastic work to failure in male femurs*

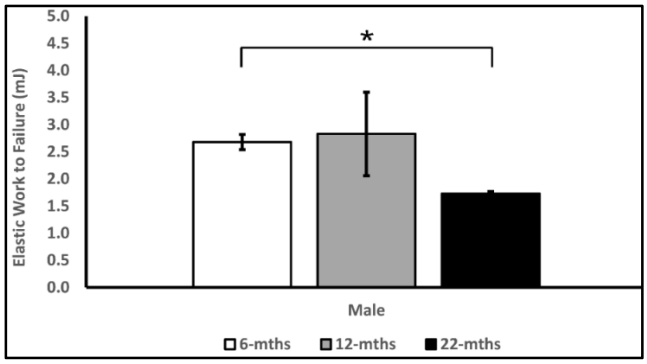

Figure 3-70*: Elastic work to failure in male tibiae*

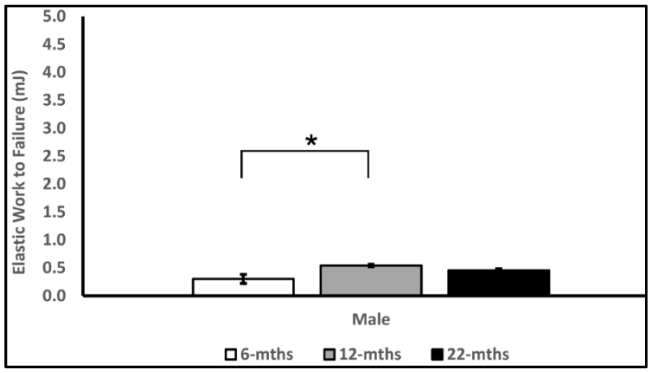

Figure 3-71*: Elastic work to failure in male ulnae*

3.3.7 Plastic work to failure

Plastic work to failure in male femurs, tibiae and ulnae is shown in *Figures 3.72, 3.73 and 3.74,* respectively. Male femurs and tibiae showed no change while in male ulnae, plastic work to failure decreased significantly from 6 months to 12 months.

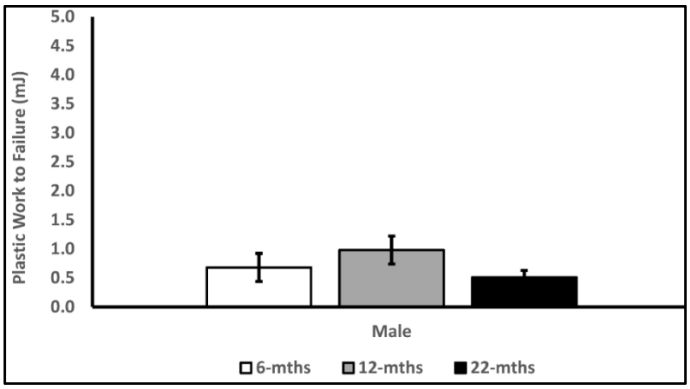

Figure 3-72*: Plastic work to failure in male femurs*

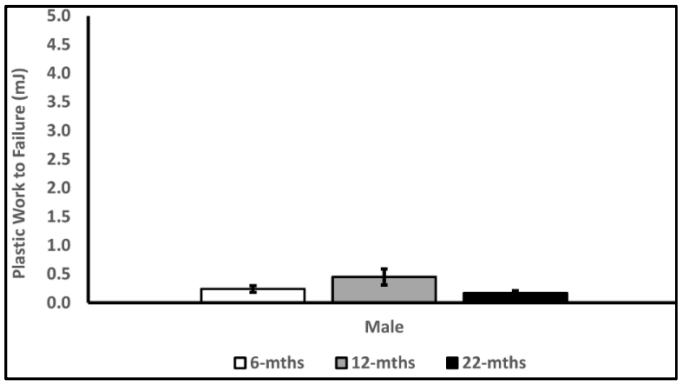

Figure 3-73*: Plastic work to failure in male tibiae*

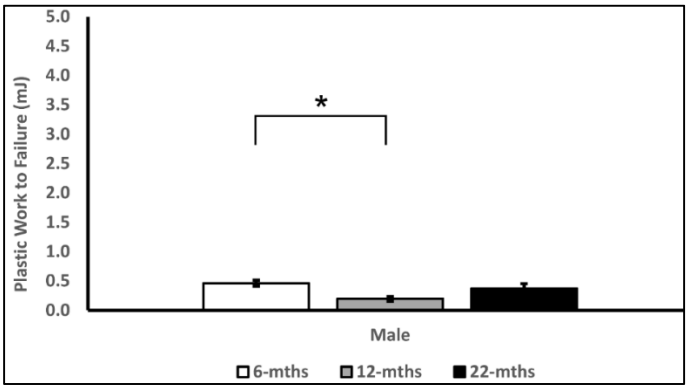

Figure 3-74*: Plastic work to failure in male ulnae*

3.3.8 Elastic displacement

Elastic displacement in male femurs, tibiae and ulnae is shown in *Figures 3.75, 3.76 and 3.77,* respectively. Male femurs showed no change while in tibiae, elastic displacement decreased significantly from 6 months to 22 months. In ulnae, elastic displacement increased from 6 months to 12 months.

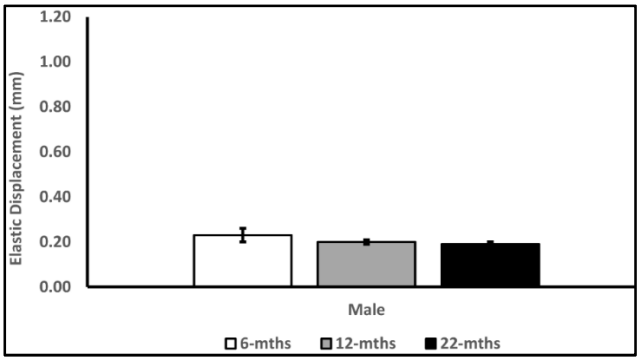

Figure 3-75*: Elastic displacement in male femurs*

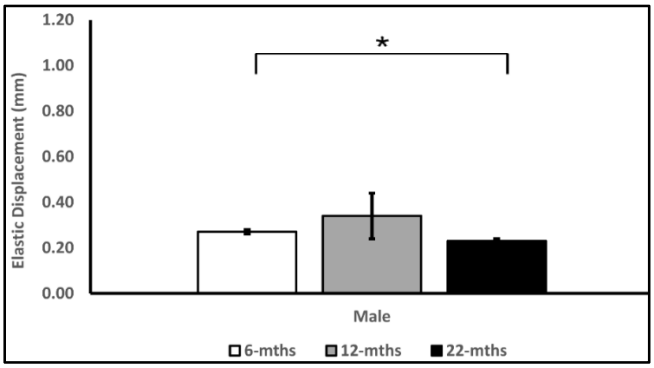

Figure 3-76*: Elastic displacement in male tibiae*

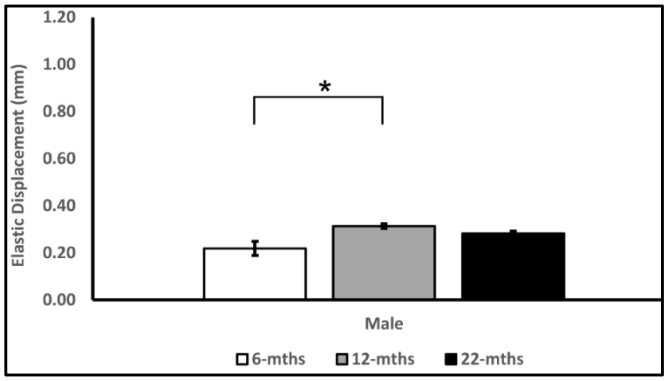

Figure 3-77*: Elastic displacement in male ulnae*

3.3.9 Post yield displacement

Post yield displacement in male femurs, tibiae and ulnae is shown in *Figures 3.78, 3.79 and 3.80,* respectively. Male femurs and tibiae showed no change while in male ulnae, post yield displacement decreased significantly from 6 months to 12 months.

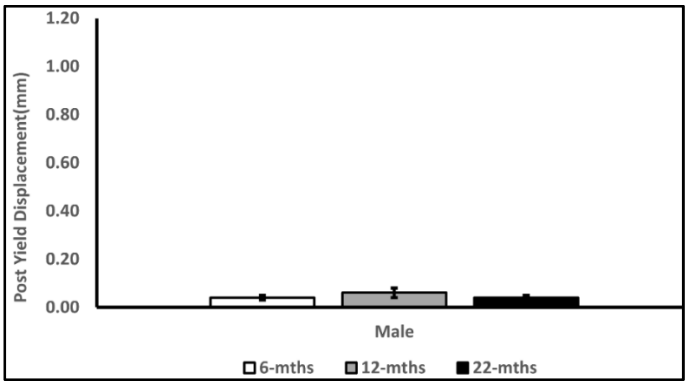

Figure 3-78*: Post yield displacement in female femurs*

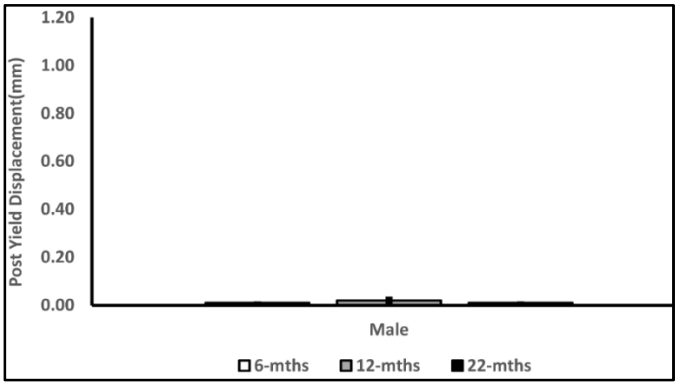

Figure 3-79*: Post yield displacement in male tibiae*

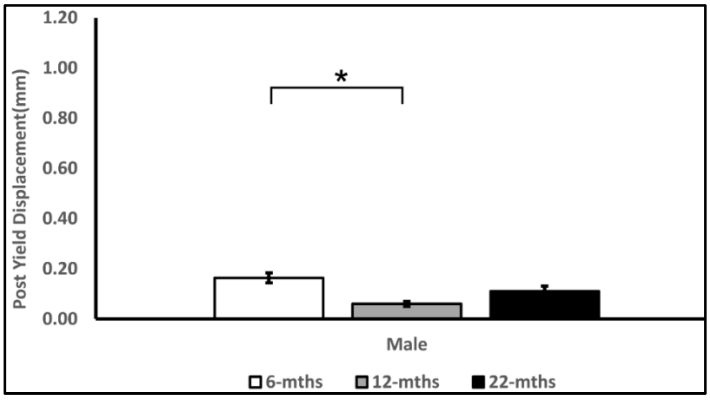

Figure 3-80*: Post yield displacement in male ulnae*

3.3.10 Compressive strength

Compressive strength in male femurs, tibiae and ulnae is shown in *Figures 3.81, 3.82 and 3.83,* respectively. There is no change observed in compressive strength of any of the male bones.

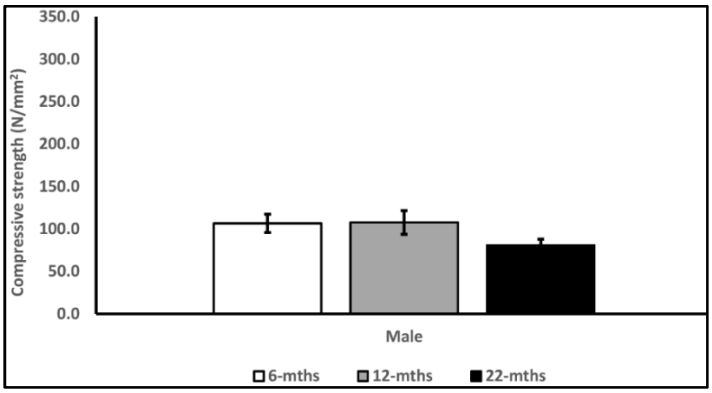

Figure 3-81*: Compressive Strength in male femurs*

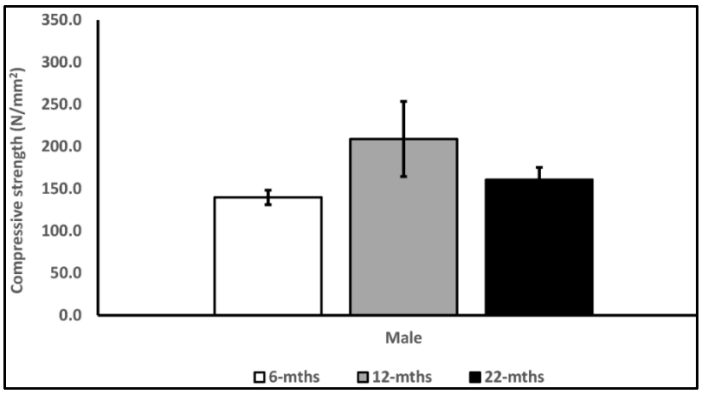

Figure 3-82*: Compressive Strength in male tibiae*

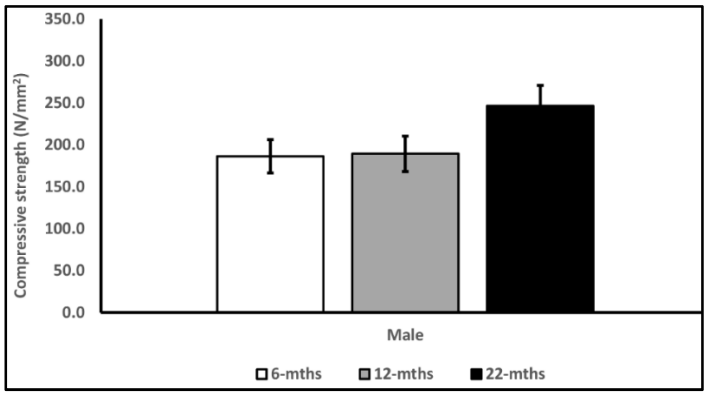

Figure 3-83*: Compressive Strength in male ulnae*

3.3.11 Tensile strength

Tensile strength in male femurs, tibiae and ulnae is shown in *Figures 3.84, 3.85 and 3.86,* respectively. In male femurs, tensile strength decreased significantly in 22 months compared to 6 months, while in tibiae and ulnae, no differences were observed.

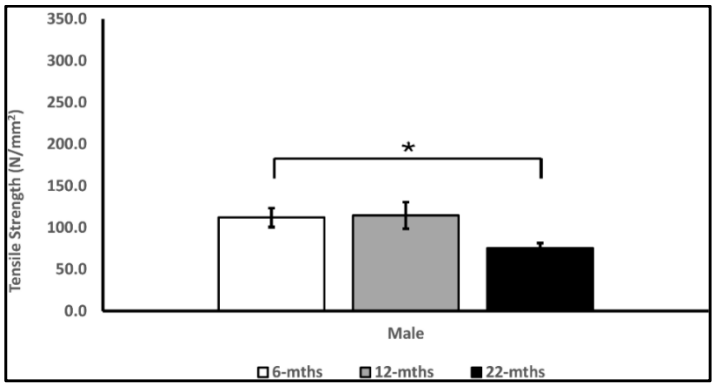

Figure 3-84*: Tensile Strength in male femurs*

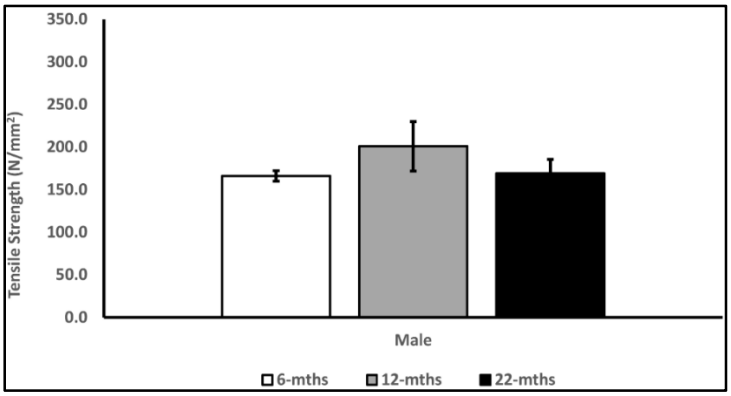

Figure 3-85*: Tensile Strength in male tibiae*

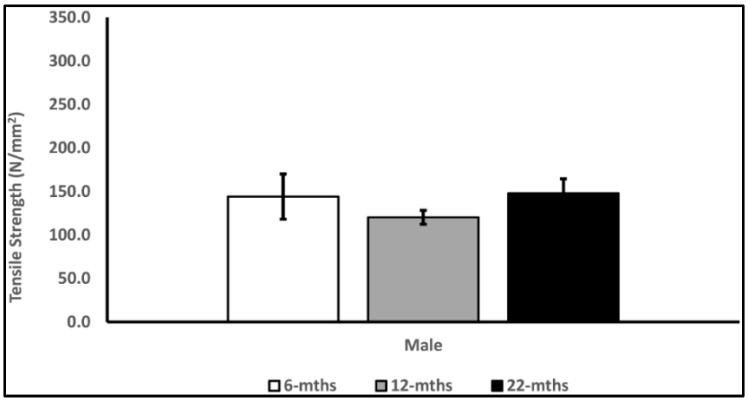

Figure 3-86*: Tensile Strength in male ulnae*

3.4 Micro-CT Analysis

Micro-computed tomography or micro-CT is a valuable technique for the investigation of bone microstructural parameters and its quantitative assessment. The most important parameter obtained from micro-CT analysis is bone volume density or bone volume over total volume (BV/TV). It indicates the fraction of a given volume of interest that is occupied by mineralized bone and usually reported as a percentage value. The BV/TV of cortical as well as trabecular bone was calculated for each sample. The ulna does not have any trabecular bone, so trabecular BV/TV was not calculated in ulnae. Cortical bone area is also considered as a good predictor of whole bone strength and the estimated cortical bone area is presented in the following sections.

3.4.1 Micro-CT analysis – Female femurs, tibiae and ulnae

3.4.1.1 Cortical bone volume / total volume (BV/TV) - Females

Cortical BV/TV of female femurs, tibiae and ulnae is shown in *Figures 3.87, 3.88 and 3.89,* respectively. There were no differences observed in cortical BV/TV for any of the female bones with aging.

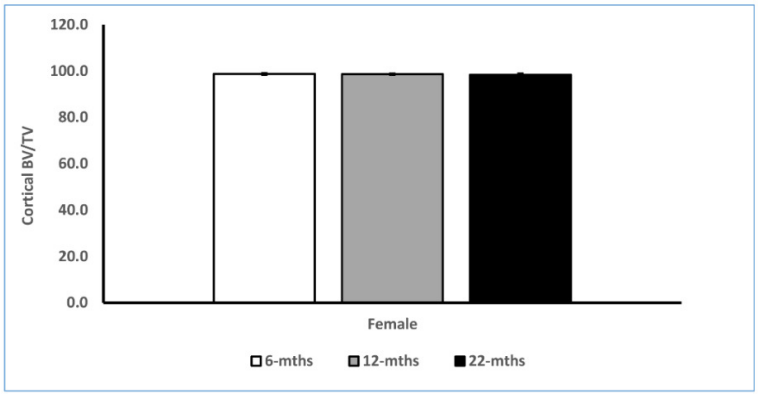

Figure 3-87*: Cortical BV/TV female femurs*

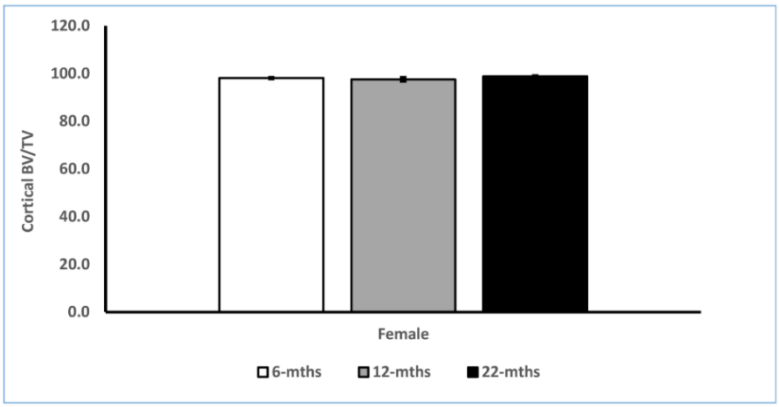

Figure 3-88*: Cortical BV/TV female tibiae*

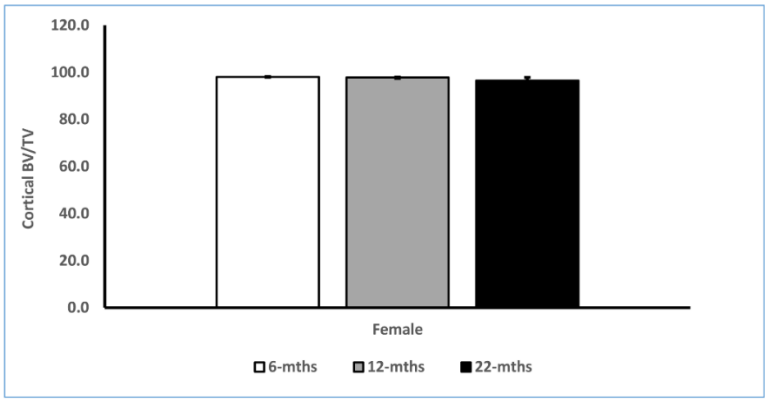

Figure 3-89*: Cortical BV/TV female ulnae*

3.4.1.2 Trabecular bone volume / total volume (BV/TV) - Females

Trabecular BV/TV of female femurs and tibiae is shown in *Figures 3.90 and 3.91,* respectively. In female femurs, trabecular BV/TV decreased significantly in 12 months and 22 months compared to 6 months. There were no differences observed in trabecular BV/TV of

tibiae with aging. Trabecular bone for ulnae was not measured as it makes up only a very small fraction of this bone.

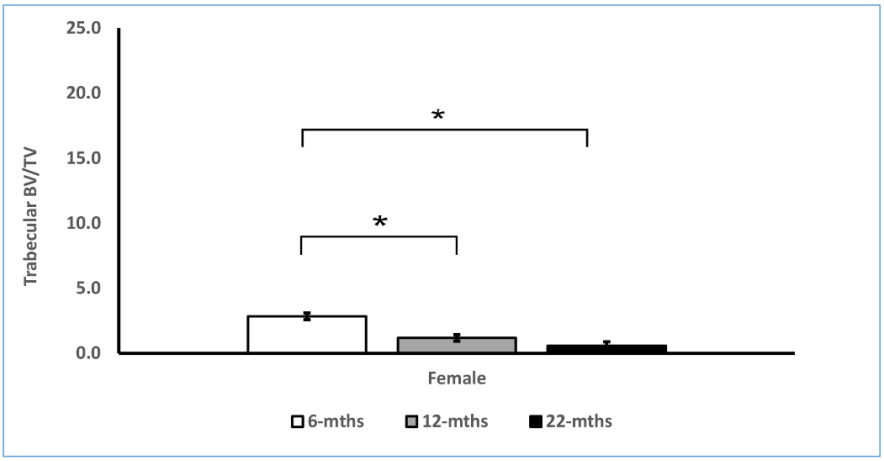

Figure 3-90*: Trabecular BV/TV female femurs*

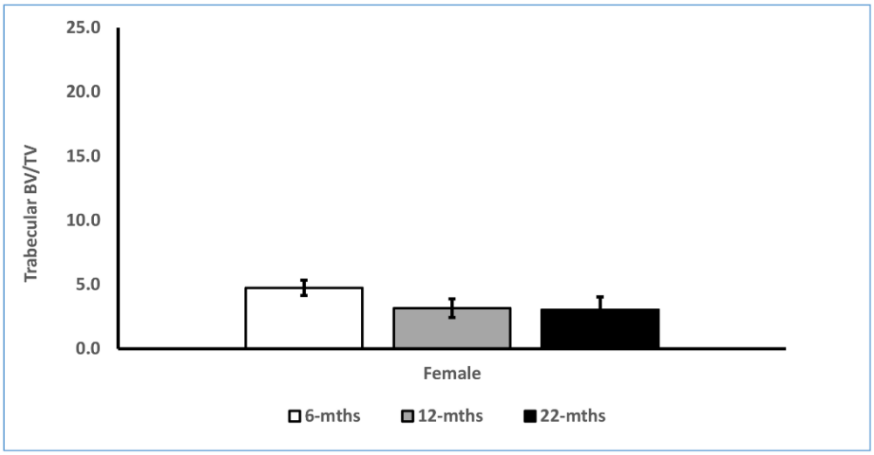

Figure 3-91*: Trabecular BV/TV female tibiae*

3.4.1.3 Cortical bone area - Females

Cortical bone area of female femurs, tibiae and ulnae is shown in *Figures 3.92, 3.93 and 3.94,* respectively. There were no differences observed in cortical bone area of any of the female bones with aging.

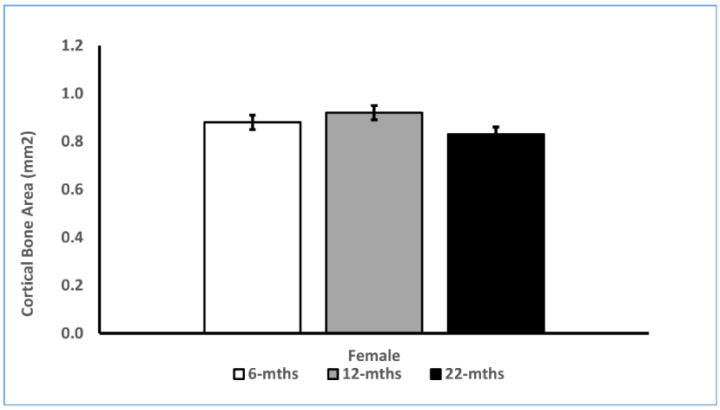

Figure 3-92*: Cortical bone area female femurs*

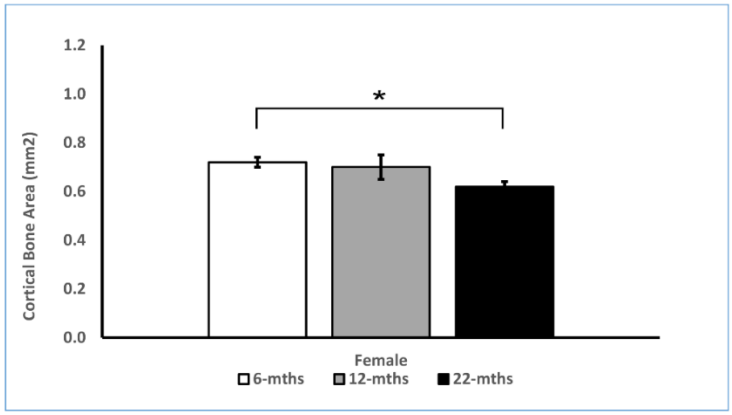

Figure 3-93*: Cortical bone area female tibiae*

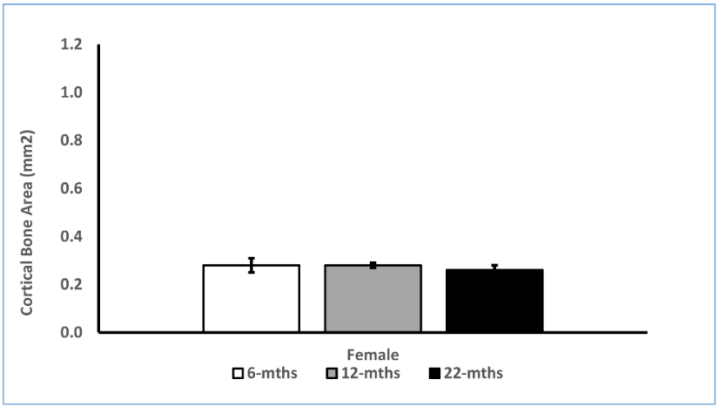

Figure 3-94*: Cortical bone area female ulnae*

3.4.2 Micro-CT analysis – Male femurs, tibiae and ulnae

3.4.2.1 Cortical bone volume / total volume (BV/TV) – Males

Cortical BV/TV of male femurs, tibiae and ulnae is shown in *Figures 3.95, 3.96 and 3.97,* respectively. There were no changes/differences observed in cortical BV/TV of any of the male bone with aging.

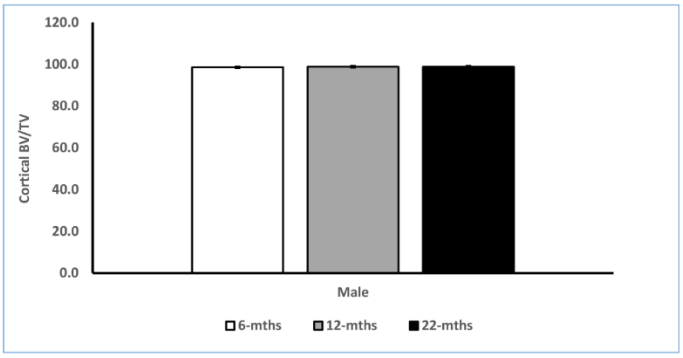

Figure 3-95*: Cortical BV/TV male femurs*

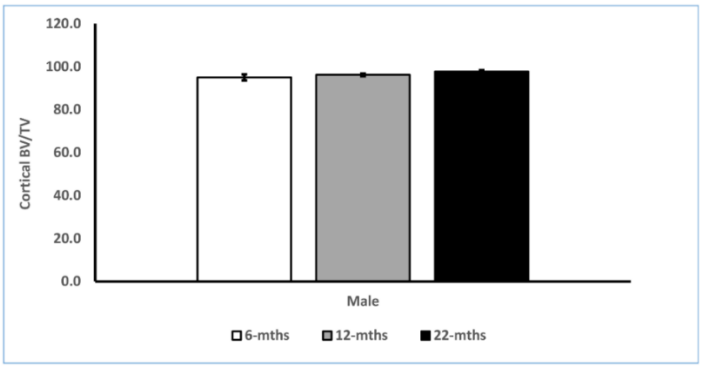

Figure 3-96*: Cortical BV/TV male tibiae*

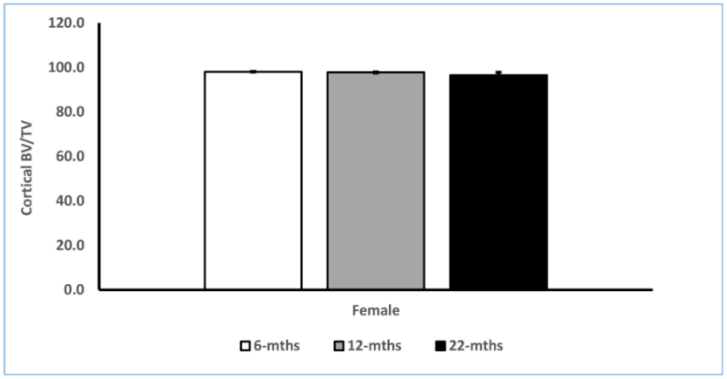

Figure 3-97*: Cortical BV/TV male ulnae*

3.4.2.2 Trabecular bone volume / total volume (BV/TV) - Males

Trabecular BV/TV of male femurs and tibiae is shown in *Figures 3.98 and 3.99,* respectively. In male femurs, trabecular BV/TV decreased significantly at 12 months and 22 months compared to 6 months while tibiae showed that trabecular BV/TV decreased at 22 months only.

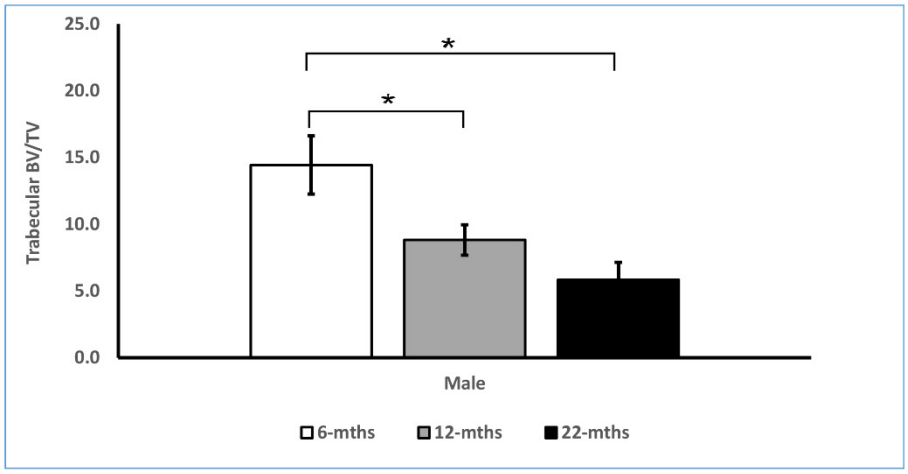

Figure 3-98*: Trabecular BV/TV male femurs*

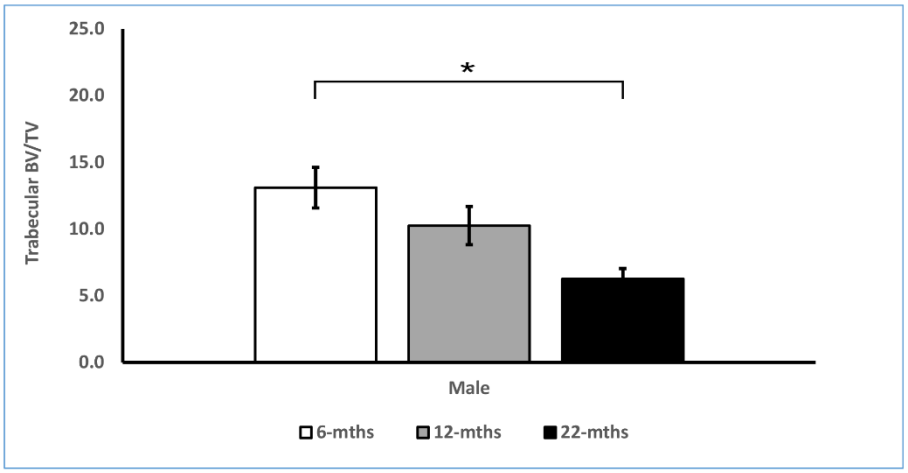

Figure 3-99*: Trabecular BV/TV male tibiae*

3.4.2.3 Cortical bone area - Males

Cortical bone area of male femurs, tibiae and ulnae is shown in *Figures 3.100, 3.101 and 3.102,* respectively. There were no differences observed in cortical bone area of any of the male bones with aging.

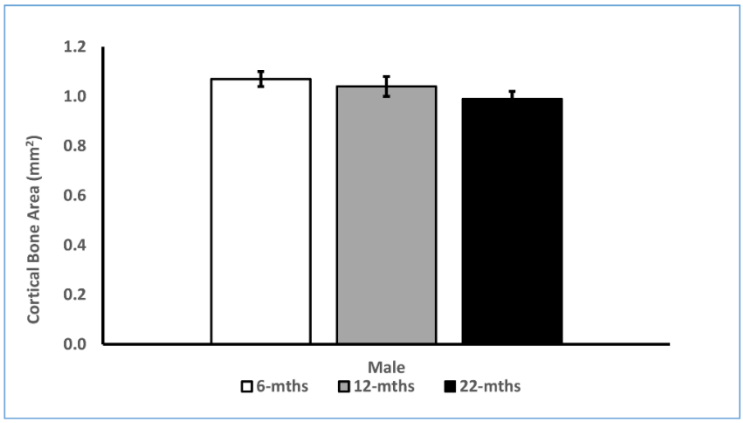

Figure 3-100*: Cortical bone area male femurs*

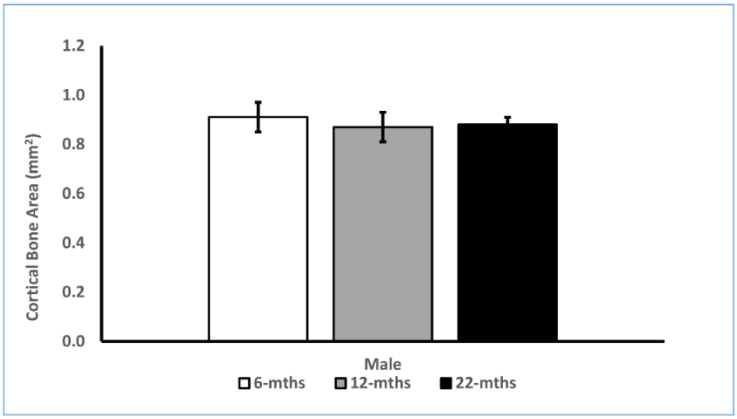

Figure 3-101*: Cortical bone area male tibiae*

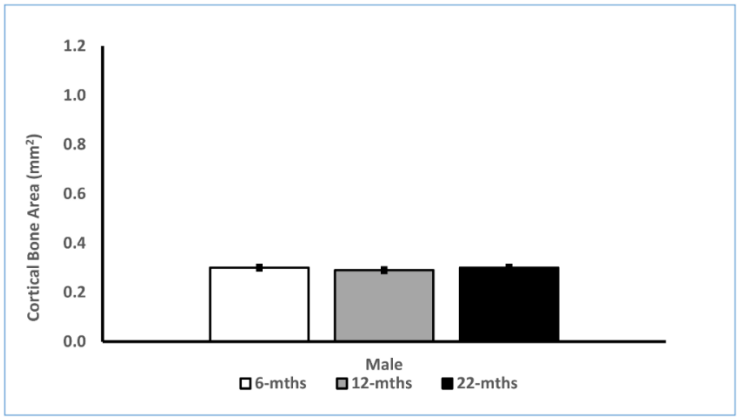

Figure 3-102*: Cortical bone area male ulnae*

In this chapter, all the results are presented using graphs along with the indication of the significant changes observed with aging. The summary of these results with their interpretation will be discussed in the following chapter. The correlation of micro-CT parameters with the biomechanical parameters will also be discussed to provide a rationale for the behavior of the bones as they age.

CHAPTER 4
DISCUSSION

4.1 Strain Response

It was hypothesized that the strains captured from the digital image correlation technique will be significantly higher than the strains captured from the traditional strain gaging because the strain gage artificially stiffens the surface of the bone due to the application of the glue. It was observed that the strains captured by DIC technique in ulnae were significantly higher than the strain gage strains while tibia showed no significant differences in strains captured between the two methods. The strain results presented in chapter 3 are summarized in *Figure 4.1* with an illustration of the research questions addressed. The changes observed are based on linear regression analysis with robust standard error testing and the level of significance was set to 0.05.

Hypothesis 1

DIC strains higher than SG strains?

ULNA	Male	Female
6 Mo	Yes (L,M & H)	Yes (L)
12 Mo	Yes (L)	No
22 Mo	No	No

TIBIA	Male	Female
6 Mo	No	No
12 Mo	No	No
22 Mo	No	No

* **L**=low load, **M**=medium load & **H**=high load

Hypothesis 2

Changes observed in strains with aging

Significant Decrease *Significant Increase* *No Change*

ULNA	Strain Gage Results		DIC Results	
	Male	Female	Male	Female
Strains at 1.3 N	$		$	$
Strains at 2.3 N		$	$	$
Strains at 3.3 N	$			$

TIBIA	Strain Gage Results		DIC Results	
	Male	Female	Male	Female
Strains at 7.5 N				
Strains at 11.5 N			$	
Strains at 15.5 N				

$ 6 to 22 months only, no changes observed from 6 to 12 months

Fig 4-1: *Summary of strain response – Methods comparison (left) and Aging comparisons (right)*

Ulnae represents the forearm compression loading model while tibia represents the hindlimb compression loading model which has completely different strain distribution with respect to the applied loading. *Lee et al 2002* showed that ulna experiences compressive strains on the medial surface [27] and *Sztefek et al 2010* demostrated that tibia experiences tensile strains on the medial surface due to its curved shape [28].

The ulna is a bone that mostly consists of a cortical part, while the tibia represents a mixed model of cortical and trabecular bone. *Chen et al 2013* concluded in human studeis, that the trabcelar bone loss is one of the most important age related bone changes [29]. *Boskey et al 2010* has reviewed the age related changes in bone and found that trabecular number in bones decline significantly with aging in both humans and mice [1].

Due to the differences in morphology and the manner in which load is distributed between the two kinds of bones, it would be reasonable to expect different strain responses between the ulna and tibia. This might explain why the ulna showed higher strains with DIC technique, but tibia did not show differences between the two methods. The shape of the bone could also play an important role in the strains experienced on the surface of the bone. The flatter the surface of the bone, the better the capture of 2D strain response. *Verhulp et al 2004* and *Franck et al 2007* demonstrated that 2D-DIC method only captures a plane strain field corrsponding to the sample surface. When the sample deforms out of plane or the sample is a non planar geometry, 3D-DIC technique would be a better approach [30] [31]. Hence, the strain gage could work better than DIC for non planar samples because the strain gage sticks with the surface according to its shape and thereby reduces the non planar effects. In the case of DIC, it is difficult to align the plane of the camera to the plane of the region of interest on the bone surface or conversely, it is difficult to pick the region of interest from the surface which is

aligned with the lens and also consistent with the location where the strain gage could be applied later on the sample. *Ramault et al 2011* determined that delamination can occur at the central portion of the bone during loading and this could effect the strain results [32]. Hence, care must be taken while attaching the strain gage on the bone surface.

In tibiae, there was no difference between the strains captured by both methods. A stiffer response was expected due to the application of the strain gage and glue, but was not observed. This could be in part due to the comparatively irregular surface of this bone or it could be due to the number of limitations associated with this technique. *Bornert et al 2009* determined that the number of parameters that have to be set in DIC measurements influences the quality of the results obtained [33]. *Hensley et al 2017* showed that the quality of speckle pattern could directly impact the ability to capture the accurate results [34].

In conclusion, this study confirmed the hypothesis of higher predicted strains using DIC compared to strain gaging for ulnae, but rejected the hypothesis for tibiae. However, as discussed above, this study has limitations and what clearly emerges from these results is that using one method versus another is not as critical as applying the same method across treatment groups in an experiment and between experiments if direct comparisons are required for the analysis.

It was also hypothesized that ulnae and tibiae will show a stiffer repsonse with aging using both DIC technique and strain gaging method. According to the *Figure 4.1*, the changes are very obvious in ulnae using either of the methods, while there is almost no changes observed in the tibiae with either DIC or strain gaging methods.

The changes observed in ulnae align well with the hypothesis. *Leucht et al 2013* showed that the strains on the medial surface of ulnar mid shaft increased as a function of load [35]

and hence the medial surface of ulna can be considered as a best site to capture surface strains. Due to the flatter medial surface in ulnae compared to tibiae, DIC can be considered as a viable method to capture the bone surface strains in ulnae and similar flat bones. The DIC results show a significant decrease in strain at the age of 22 months compared to 6 months in both males and females at all the loads except in males at higher load. There was no change found at the age of 12 months compared to 6 months. On the other hand, strain gage results showed a significant increase in males while a decrease in females was observed at the age of 22 months compared to 6 months of age.

No changes were observed at the age of 12 months compared to the 6 months of age. *Ferguson et al 2003* showed that the percentage mineralization in femurs of C57Bl/6 mice increased rapidly thorugh 3 months of age and maintained at mature levels through 13 months and decreased significantly at the age of 26 months. Also, the bone loss in mice occured after 20 months of age [16]. This data suggests that mineralization could play an important role in the resulting stiffness of the bone with aging. Bone mineral density (BMD) was measured but the data was not analyzed statistically, so at this point it is difficult to suggest that mineralization was a critical determinant of age changes in strains generated by loading. Another possibility is that the collagen organization changed in some fashion with aging. As the collagen structure was not specifically measured, any specific conclusion cannot be drawn in this regard.

The tibiae showed no changes while ulnae showed a stiffer response with aging. Since the tibia has both trabecular and cortical bone, while the ulna is largely cortical bone, the presence of trabecular elements would favor structural flexibility over stiffness and it can absorb more

energy by deforming [36]. On the basis of these observations and previous literature, hypothesis for ulnae can be accepted and this hypothesis for tibia can be rejected.

4.2 Biomechanical Parameters

The decreased bone mass, which results in an increased risk of fracture in humans was also expected in mice bones. Therefore, it was hypothesized that both genders will display a significant decrease in biomechanical performance at the age of 12 months and 22 months compared to 6 months in all the bones.

While size and shape are the morphological traits that determine the strength of the bone [37], the composition and mechanical properties of the bones will vary as a function of age. Understanding the factors controlling the aging of cells and identifying specific pathways that control these factors at different ages is a great challenge [1].

In *Figure 4.2*, the biomechanical performance of all the bones is summarized and the changes observed are also described. The biomechanical parameters listed in *Table 1* are grouped into structural, material and geometric properties.

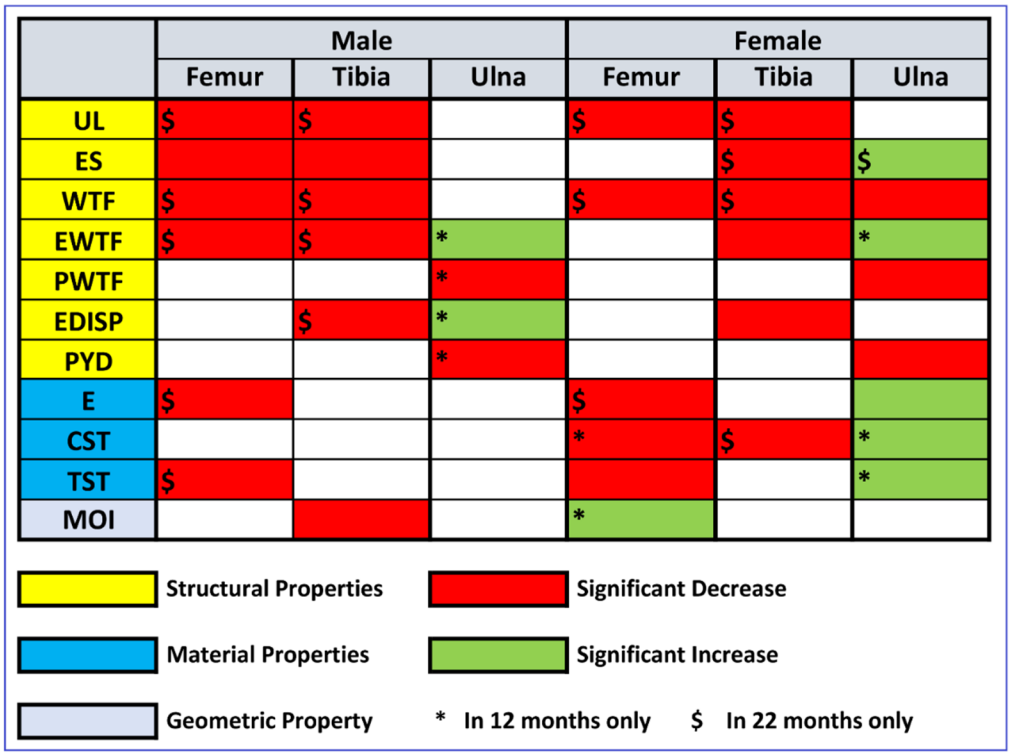

Fig 4-2: *Summary of biomechanical parameters*

However, before discussing all the biomechanical parameters in detail, it is necessary to understand the definition of these parameters, which is given in *Table 2.*

Table 2: *Definition of biomechanical parameters*

Ultimate load	The bone is stronger if the ultimate load is higher
Elastic stiffness	If the bone is stiffer, more force is required to displace it from the original position
Modulus of elasticity	It represents the stiffness of the material. A stiff material has a higher modulus of elasticity, while a flexible material has lower modulus of elasticity
Moment of inertia	It is the geometric property of cross-sectional area that represents the magnitude of the resistance to bending

Bending strength	It represents the maximum stress (compression or tension) that a bone can withstand in bending before fracture
Work to failure	The more the work to failure, tougher is the bone
Elastic work to failure	The more the elastic work to failure, more is the brittleness
Plastic work to failure	The more the plastic work to failure, more is the plasticity
Post yield displacement	The higher the post yield displacement, more ductile is the bone

The summary of the parameters in *Figure 4.2*, illustrates the age and gender effects on the biomechanical performance of femurs, tibiae and ulnae. The red tab shows a significant decrease at 12 and 22 months of age compared to 6 months while the green tab shows a significant increase at 12 and 22 months compared to 6 months. An asterisk (*) was used to denote statistically significant changes only at 12 months while the dollar ($) sign demarks significant changes only at 22 months.

Ferguson et al 2003 studied the age-related changes in male femur of C57Bl/6 mice of age between 1 to 26 months and found a substantial increase in bone size, mineral mass and mechanical properties at the age of 3 months. These peak values were maintained through 11 months of age [16]. Then these values start to decline and elastic stiffness along with bone mass reduced substantially at the age of 26 months [16].

In this study, clear differences in structural properties, e.g. ultimate load, elastic stiffness and work to failure, were observed. Specifically, femurs and tibiae showed a significant decrease in these structural properties with most of the changes observed at 22 months

compared to 6 months. Ulnae also showed some significant increase in the structural properties with age.

Currey 1969 studied the mineral content of the bone and found that it increases with age. It increases the ultimate load and decreases the toughness of the bone [38]. *Currey 1984* reported the inverse relationship between stiffness and ductility in the cortical bone of both mice and humans. In addition, high mineralization content resulted in a high modulus of elasticity and low work to failure and eventually low toughness [39].

Ritchie et al 2006 demonstrated that non-enzymatic cross-linking in the collagen increases with aging, which reduces the post yield deformation in collagen fibers and thus results in the reduction of growth toughness [40]. *Gautieri et al 2014* also reported that the increased cross-linking in the collagen fibers reduces toughness and increases the ultimate load and elastic stiffness of the bone [41].

The femurs and tibiae are the bones that contains both cortical and trabecular bone while ulna have no trabecular bone. With this in mind, these findings suggest that the loss of trabecular bone plays a more dominant role in aging and could play a bigger part in the decline of biomechanical performance of the bone. *Beamer et al 1996* reported that inbred strains including C57Bl/6 mice showed no bone loss until 12 months of age [42] and these results are in strong agreement with this. Most of the published data is based on the studies conducted on femurs and this data shows similar behavior in structural properties of femurs and tibiae. On the other hand, the ulnae showed completely different behavior.

Femurs showed a decline in the material properties in both males and females while tibiae showed no changes except for compressive strength, which decreased in female tibiae at 22

months of age. Male ulnae showed no changes while female ulnae showed enhanced material properties with aging.

The moment of inertia decreased in male tibiae but increased in female femurs at 12 months of age only. No changes were observed in the rest of the bones. Moment of inertia is a geometric property and directly dependent on the cross-sectional area of the bone. However, no changes were observed in the cross-sectional area of the bones with aging. The diameter of the bone increases with aging but cortical thickness decreases that compensates the resulting resistance to bending and hence maintains the moment of inertia in most of the cases.

Based on the observations and discussion in the light of previous literature, the hypothesis held true for both femur and tibia, but the hypothesis for ulnae regarding the decline of biomechanical performance with aging can be rejected.

Gender differences were also examined in this data. The comparisons were made using a 2 sample T-Test with unequal variance and the significance level was set to 0.05. Tensile strength in ulnae, and elastic displacement along with elastic stiffness in femur were significantly different between sexes at 12 months while there were no differences found in tibiae. A considerable difference was observed at the age of 22 months in all the bones while most of the differences were found in tibiae.

To find the explanations for the results obtained from the biomechanical parameter analysis, micro-CT analysis was performed, and the biomechanical parameters were correlated with the micro-CT parameters. Cortical BV/TV, trabecular BV/TV and cortical bone area were calculated and correlated with ultimate load, elastic stiffness, modulus of elasticity and moment of inertia. The Pearson correlation analysis was done by merging all the age groups

together in one and the significance level was set to 0.05. The correlation results for all the male bones are summarized in *Figure 4.3* and females are summarized in *Figure 4.4*.

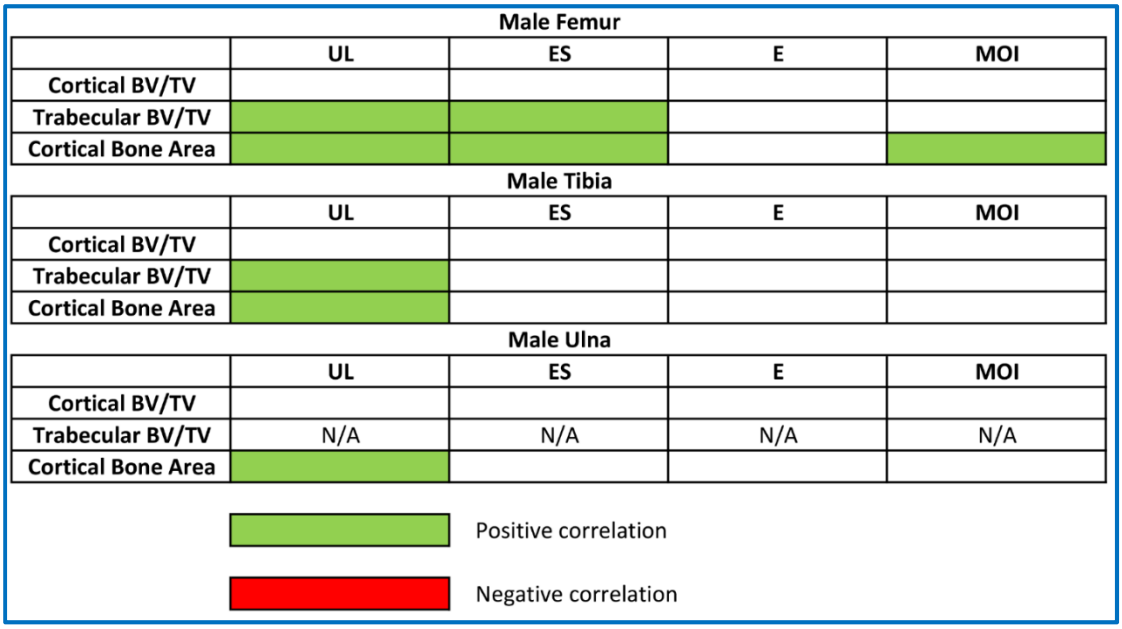

Fig 4-3: *Correlation analysis males*

It was observed that the cortical BV/TV is not influencing any of the biomechanical parameters in all type of male bones. Ultimate load is positively correlated with the trabecular BV/TV and cortical bone area in all male bones and will maintain its strength if trabecular BV/TV can be maintained with aging. Elastic stiffness of the male femur is positively correlated with the trabecular BV/TV and cortical bone area too. Moment of inertia of male femur increases with the increase in the cortical bone area.

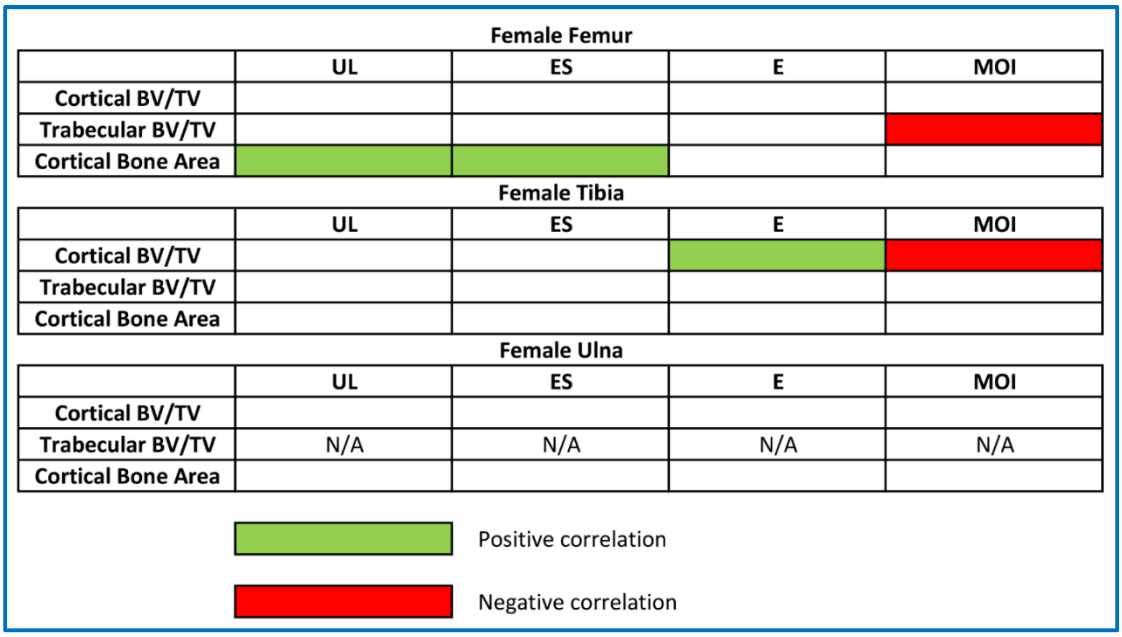

Fig 4-4: *Correlation analysis females*

Ultimate load and elastic stiffness of the female femurs is positively correlated to the cortical bone area. Cortical BV/TV is not playing a role in the biomechanical performance while trabecular BV/TV is only influencing on the moment of inertia of female femurs and is negatively correlated. Cortical BV/TV is only influencing the modulus of elasticity and moment of inertia of the female tibiae. As the cortical bone area increases, it tends to increase the modulus of elasticity while it reduces the moment of inertia.

Collectively these data suggest that different bones change with aging in different fashions, while this study does not address the molecular basis of these changes. Future work focused on understanding the underlying collagen structure and how it might be changing could provide a means to address this question.

CHAPTER 5
CONCLUSION AND FUTURE WORK

Aging is the process of decline in biomechanical performance of the skeleton that occurs after reaching maturity. Overall, an imbalance in bone resorption and formation results in overall bone loss leading to increased fracture risk. However, a detailed aging study on the human skeleton is extremely difficult to accomplish and that is why there is still insufficient understanding of how human bones age. An aging study of the mouse skeleton is presented in this dissertation to ascertain changes in the performance of different bones.

This is a unique study performed on three different bones of the same mice. It provided us an opportunity to perform direct comparisons of different bones of the same skeleton. The first aim of the study was based on the hypothesis that DIC strains will be higher than strains captured from traditional strain gaging. The hypothesis for ulnae was accepted while the hypothesis for tibiae was rejected. Secondly, it was hypothesized that both ulnae and tibiae will show a stiffer response with aging, but the hypothesis was held true only for ulnae.

Ulna and tibia behaved differently in strain response. Also, femur, tibia and ulna all behaved differently in terms of biomechanical parameters. Therefore, it was concluded that the study of the bones should be performed in a site-specific manner and one cannot extrapolate the data of one bone to another bone.

Most of the gender differences were found at 22 months of age, which suggests that the biomechanical performance of both males and females were similar from 6 months to 12 months and showed changes only with advanced aging.

Normal aging of the mouse skeleton does closely mimic the normal aging of human skeleton. *Moran et al 2007* demonstrated that estrogen levels are maintained in mature C57Bl/6 female mice [43]. *Recker et al 2000* studied the perimenopausal bone loss and concluded that

significant bone loss was caused by estrogen deprivation in women [44]. In this study, no significant differences were observed between mature male and female mice up through 12 months of age, and this may be due to adequate levels of estrogen, which are maintained during aging in C57Bl/6 mice.

This work will add to our understanding, the effects of age and gender in the biomechanical performance and the strain response of the mouse bones. It also represents an attempt to investigate the mechanisms behind the differences found during aging. This study gathered a useful information about the differences in strains experienced by the bone with aging. However, a comprehensive study is required for understanding the function of these strains to assess the anabolic bone response.

Due to the difference in response to mechanical stimuli in periosteal and endosteal bone, the cross-sectional geometry should be studied in detail by conducting histomorphometric comparisons of young, adult and aged mice. Also, smaller cortical thickness and greater minimum moment of inertia in aged mice compared to adult mice reported in literature suggested a future study to investigate these details as well.

Raman spectroscopy and Fourier-transform infrared spectroscopy (FTIR) on these bones to see the characterization of collagen and mineral phases would help to support our speculations about the correlation of these factors with the biomechanical parameters and strain results.

An important finding from all the data is that different bones behave differently at different ages. These differences appear to be due to shape differences and biomechanical properties. Therefore, investigators using the mouse aging models should be careful to draw conclusions only on the bones being studied and not attempt to make broad generalizations to the entire

skeleton. There are also important differences between the aging changes of the male mouse skeleton compared to the female mouse skeleton and each gender needs to be specifically studied.

List of References

[1] Boskey AL, Coleman, R. Aging and Bone. *J Dent Res,* 2010; 89(12): 1333-1348.

[2] Tommasini SM, Nasser P, Jespsen KJ. Sexual dimorphism affects tibia size and shape but not tissue-level mechanical properties. *Bone*, 2007; 40: 498-505.

[3] Chan GK, Duque G. Age related bone loss: old bone, new facts. *Gernotology,* 2002; 48: 62-71.

[4] Eileen M. Crimmins. Lifespan and healthspan: Past, present and promise. *Gerontologist,* 2015; 55(6): 901-911.

[5] Johnell O, Kanis JA. An estimate of the worldwide prevalence and disability associated with osteoporotic fractures. *Osteoporos Int,* 2006; 17(12): 1726-33.

[6] Melton LJ 3rd, Atkinson EJ, O'Connor MK, O'Fallon WM, Riggs BL. Bone density and fracture risk in men. *J Bone Miner Res,* 1998; 13(12): 1915-1923.

[7] Melton LJ 3rd, Chrischilles EA, Cooper C, Lane AW, Riggs BL. Perspective. How many women have osteoporosis? *J Bone Miner Res,* 1992; 7(9): 1005-10

[8] Gullberg B, Johnell O, Kanis JA. World-wide projections for hip fracture. *Osteoporos Int,* 1997; 7(5): 407-13

[9] Robling AG, Burr DB, Turner CH. Recovery periods restore mechanosensitivity to dynamically loaded bone. *J Exp Biol.* 2001; 204(19): 3389-99.

[10] Sugiyama T, Price JS, Lanyon LE. Functional adaptation to mechanical loading in both cortical and cancellous bone is controlled locally and is confined to the loaded bones. *Bon,* 2010; 46(2): 314-321.

[11] Willinghamm MD, Brodt MD, Lee KL, Stephens AL, Ye J, Silva MJ. Age-related changes in bone structure and strength in female and male BALB/c mice. *Calcif Tissue In,* 2010; 86(6): 470-83.

[12] Patel TK, Brodt DM, Silva MJ. Experimental and finite element analysis of strains induced by axial tibial compression in young-adult and old female C57Bl/6 mice. *J Biomech,* 2014; 47(2): 451-457.

[13] Moustafa A, Sugiyama T, Saxon LK, Zaman G, Sunters A, Armstrong VJ, Javaheri B, Lanyon LE, Price JS. The mouse fibula as a suitable bone for the study of functional adaptation to mechanical loading. *Bone,* 2009; 44(5): 930-935.

[14] Willie BM, Birkhold AI, Razi H, Thiele T, Aido M, Kruck B, Schill A, Checa S, Main RP, Duda GN. Diminished response to in vivo mechanical loading in trabecular and not cortical bone in adulthood of female C57Bl/6 mice coincides with a reduction in deformation to load. *Bone,* 2013; 55(2): 335-346.

[15] Syed F.A, Hoey K.A. Integrative physiology of the aging bone: insights from animal and cellular models. *Annals of the New York academy of Sciences,* 2010; 1211: 95-106.

[16] Ferguson VL, Ayers RA, Bateman TA, Simske SJ. Bone development and age-related bone loss in male C57Bl/6J mice. *Bone,* 2003; 33(3): 387-98.

[17] Begun DL. Age-related changes in bone: Variation and factors influencing bone fragility. *Doctor of Philosophy dissertation, University of Michigan,* (2015)

[18] Jamsa T, Jalovara P, Peng Z, Vaananen H.K, Tuukkanen J. Comparison of three-point bending test and peripheral quantitative computed tomography analysis in the evaluation of the strength of mouse femur and tibia. *Bone,* 1998; 23(2): 155-161.

[19] Brodt MD, Ellis CB, Silva MJ. Growing C57BL/6 mice increase whole bone mechanical properties by increasing geometric and material properties. *J Bone Miner,* 1999; 14(12): 2159-66.

[20] Somerville JM, Aspden RM, Armour KE, Armour KJ, Reid DM. Growth of C57Bl/6 mice and the material and mechanical properties of cortical bone from the tibia. *Calcif Tissue Int,* 2004; 74(5): 469-475.

[21] Wang X, Osborn R.W, Wolf JC, Puram S. Age related changes in the mechanical properties of interstitial bone tissues. Presented at 50th Annual meeting of the orthopedic research society Paper no. 0037. March 7-10, 2004, San Francisco C.A.

[22] Schriefer JL, Robling AG, Warden SJ, Fournier AJ, Mason JJ, Turner CH. A comparison of mechanical properties derived from multiple skeletal sites in mice. *Journal of Biomechanics,* 2005; 38: 467-475.

[23] Glatt V, Canalis E, Stadmeyer L, Bouxsein ML. Age related changes in trabecular architecture differ in female and male C57Bl/6J mice. *Journal of Bone and Mineral Research,* 2007; 22(8): 1197-207

[24] Panel on euthanasia. AVMA Guidelines for the euthanasia of animals. *ISBN 978-1-882691-21-0,* 2013; (0)1

[25] Method text for morphometric analysis of bones (or other samples) using SkyScan micro-CT imaging and analysis / visualization.

[26] Begonia MT, Dallas M, Vizcarra B, Liu Y, Johnson ML, Thiagarajan G. Non-contact strain measurement in the mouse forearm loading model using digital image correlation (DIC). *Bone*, 2015; 81: 593-601.

[27] Lee KC, Maxwell A, Lanyon LE. Validation of a technique for studying functional adaptation of the mouse ulna in response to mechanical loading. *Bone,* 2002; 31(3): 407-12.

[28] Sztefek P, Vanleene M, Olsson R, Collinson R, Pitsillides AA, Shefelbine S. Using digital image correlation to determine bone surface strains during loading and after adaptation of the mouse tibia. *J Biomech.* 2010; 43(4): 599-605.

[29] Chen H, Zhou Xiangrong, Fujita H, Onozuka M, Kubo Kin-Ya. Age-related changes in trabecular and cortical bone microstructure. *Int J Endocrinol*, 2013; 2013.

[30] Verhulp E, van Rietbergen B, Huiskes R. A three-dimensional digital image correlation technique for strain measurements in microstructures. *J Biomech,* 2004; 37: 1313–1320.

[31] Franck C, Hong S, Maskarinec S, Tirrell D, Ravichandran G. Three-dimensional full-field measurements of large deformations in soft materials using confocal microscopy and digital volume correlation. *Exp Mech,* 2007; 47: 427–438.

[32] Ramault, C, Makris, A, Van Hemelrijck, D, Lamkanfi, E. Van Paepegem, W. Comparison of Different Techniques for Strain Monitoring of a Biaxially Loaded Cruciform Specimen. Strain, 2011; 47: 210-217.

[33] Bornert, M, Brémand, F, Doumalin, P, Dupre JC, Fazzini M, Grediac M, Hild F, Mistou S, Molimard J, Orteu JJ, Robert L, Surrel Y, Vacher P, Wattrisse B. Assessment of digital image correlation measurement errors: methodology and results. *Exp Mech*, 2009; 49(3): 353-370.

[34] Hensley S, Christensen M, Small S, Archer D, Lakes E, Rogge R. Digital image correlation techniques for strain measurement in a variety of biomechanical test models. *Acta Bioeng Biomech,* 2017; 19(3): 187-195.

[35] Leucht P, Temiyasathit S, Russell A, Arguello JF, Jacobs CR, Helms JA, Castillo AB. CXCR$ antagonism load-induced periosteal one formation in mice. *J Orthop Res*, 2013; 31(11): 1828-38.

[36] Tranquilli LP, Doria C, Zachos A, Ruggiu A, Milia F, Barca F. Bone fragility: current reviews and clinical features. *Clin Cases Miner Bone Metab,* 2009; 6(2): 109-13.

[37] Jepsen, KJ. Systems analysis of bone. *WIREs Syst Biol Med,* 2009; 1: 73-88.

[38] Curry JD. The relationship between the stiffness and the mineral content of bone. *Journal of Biomechanics*, 1969; 2(4): 477-480.

[39] Currey JD. Effects of differences in mineralization on the mechanical properties of bone. *Philos Trans R Soc Lond B Biol Sci.* 1984; 304(1121): 509-18

[40] Ritchie RO, Nalla RK, Kruzic JJ, Ager JW, Balooch G Kinney JH. Fracture and Ageing in Bone: Toughness and Structural Characterization. *Strain,* 2006; 42: 225-232

[41] Gautieri A, Redaelli A, Buehler MJ, Vesentini S. Age- and diabetes-related nonenzymatic crosslinks in collagen fibrils: Candidate amino acids involved in Advanced Glycation End-products. *Matrix Biology,* 2014; 34: 89-95

[42] Beamer WG, Donahue LR, Rosen CJ, Baylink DJ. Genetic variability in adult bone density among inbred strains of mice. *Bone*, 1996; 18(5): 397-403.

[43] Moran AL, Nelson SA, Landisch RM, Warren GL, Lowe DA. Estradiol replacement reverses ovariectomy-induced muscle contractile and myosin dysfunction in mature female mice. *J Appl Physiol*, 2007; 102(4): 1387-93

[44] Recker R, Lappe J, Davies K, Heaney R. Characterization of perimenopausal bone loss: A prospective study. J Bone Miner Res, 2000; 15(10): 1965-73.

VITA

Hammad Mumtaz was born on October 02, 1980 in Wah Cantt, Pakistan. He received his bachelor's degree in Metallurgical Engineering and Materials Science from University of Engineering and Technology, Lahore in 2004. He received his master's degree in Mechanical Engineering from Royal Institute of Technology, Stockholm in 2007.

Hammad perused his Interdisciplinary PhD degree at the University of Missouri-Kansas City. His primary PhD discipline is Engineering, and his co-discipline is Oral and Craniofacial Sciences. His research interests are in the area of bone biomechanics using the experimental techniques and computational models.